APPLICATIONS OF THE GENERALIZED DDA FORMALISM AND THE NATURE OF POLARIZED LIGHT IN DEEP OCEANS

A Dissertation

by

YU YOU

Submitted to the Office of Graduate Studies of
Texas A&M University
in partial fulfillment of the requirements for the degree of

DOCTOR OF PHILOSOPHY

August 2008

Major Subject: Physics

APPLICATIONS OF THE GENERALIZED DDA FORMALISM

AND

THE NATURE OF POLARIZED LIGHT IN DEEP OCEANS

A Dissertation

by

YU YOU

Submitted to the Office of Graduate Studies of
Texas A&M University
in partial fulfillment of the requirements for the degree of

DOCTOR OF PHILOSOPHY

Approved by:

Co-Chairs of Committee,	George W. Kattawar
	Ping Yang
Committee Members,	Glenn Agnolet
	Edward S. Fry
Head of Department,	Edward S. Fry

August 2008

Major Subject: Physics

ABSTRACT

Applications of the Generalized DDA Formalism

and

the Nature of Polarized Light in Deep Oceans. (August 2008)

Yu You, B.S., University of Science and Technology of China

Co–Chairs of Advisory Committee: Dr. George W. Kattawar
Dr. Ping Yang

The first part of this study is focused on numerical studies of light scattering from a single microscopic particle using the Discrete Dipole Approximation (DDA) method. The conventional DDA formalism is generalized to two cases: (a) inelastic light scattering from a dielectric particle and (b) light scattering from a particle with magnetic permeability $\mu \neq 1$. The first generalization is applied to simulations of Raman scattering from bioaerosol particles, and the second generalization is applied to confirmation of irregular invisibility cloaks made from metamaterials.

In the second part, radiative transfer in a coupled atmosphere-ocean system is solved to study the asymptotic nature of the polarized light in deep oceans. The rate at which the radiance and the polarization approach their asymptotic forms in an ideal homogeneous water body are studied. Effects of the single scattering albedo and the volume scattering function are studied. A more realistic water body with vertical profiles for oceanic optical properties determined by a Case 1 water model is then assumed to study the effects of wavelength, Raman scattering, and surface waves.

Simulated Raman scattering patterns computed from the generalized DDA formalism are found to be sensitive to the distribution of Raman active molecules in the host particle. Therefore one can infer how the Raman active molecules are distributed

from a measured Raman scattering pattern. Material properties of invisibility cloaks with a few irregular geometries are given, and field distributions in the vicinity of the cloaked particles computed from the generalized DDA formalism confirm that the designated material properties lead to invisibility. The radiative transfer model calculation in deep oceans suggest that the underwater radiance approaches its asymptotic form more quickly than the polarization does. Therefore, a vector radiative transfer solution is necessary for asymptotic light field studies. For a typical homogeneous water body whose scattering property is characterized by the Petzold phase function, a single scattering albedo of $\omega_0 > 0.8$ is required in order that the asymptotic regime can be reached before there are too few photons to be detected.

To my parents and to Wei

ACKNOWLEDGMENTS

I would like to acknowledge many people who have contributed to this dissertation.

First of all, I would like to thank my advisor, George W. Kattawar. I learned a lot from his insightful guidance and continuous encouragements and inspirations. His diligence and enthusiasm for science set an example for the rest of my life as a researcher. I would like to thank the co-chair of my graduation committee, Ping Yang, for his guidance and suggestions that inspired some of the research works reported in this dissertation. I also wish to thank the other committee members, Glenn Agnolet and Edward Fry, whose suggestions were very helpful in the making of this dissertation.

I am grateful to my colleagues, Hatcher Tynes, Deric Gray, Changhui Li, Peng-Wang Zhai, Zhibo Zhang, Gang Hong, and Lei Bi. It has been an impressive experience working with them. Their generous help made my research much easier.

I also appreciate the financial support from the Office of Naval Research under contracts N00014-02-1-0478 and N00014-06-1-0069, from the National Science Foundation Physical Meteorology Program (ATM-0239605), and from the NASA Radiation Sciences Program (NAG5-11374).

I extend my thanks to my dear friends, Yunfeng Li, Juntao Chang, Hebin Li, and Deqiang Sun. They shared the joys and pains with me throughout the last five years.

Finally, I am sincerest thankful to my parents, Shigen You and Xulun Tan, and to my wife, Wei, for their continual support and unfailing love.

TABLE OF CONTENTS

CHAPTER Page

LIST OF TABLES

LIST OF FIGURES

FIGURE Page

FIGURE Page

FIGURE Page

FIGURE Page

FIGURE Page

CHAPTER I

INTRODUCTION AND BACKGROUND

This dissertation is mainly focused on numerical studies of light scattering from small particles, which finds its applications in both science and engineering disciplines, such as astronomy, atmospheric sciences, oceanography, biophysics, and material science, just to name a few. Light scattering can be divided into two basic categories: single scattering, i.e., light scattering associated with a single particle, and multiple scattering, i.e., light scattering associated with a medium that consists of a collection of scattering particles. In the *single scattering approximation* of a collection of randomly positioned and widely separated particles, we assume that there is only a single scattering from source to detector. Multiple scattering occurs when photons scatter more than once from source to detector.

The first part of my research is on calculations of single scattering using the Discrete Dipole Approximation (DDA) method. The second part is on simulations of multiple scattering in a coupled atmosphere-ocean system and investigations on the asymptotic nature of polarized light in deep oceans.

A. Light Scattering by a Single Particle

Visible light is electromagnetic radiation in the wavelength range 400 nm $\leq \lambda \leq$ 700 nm and is visible to the human eye. A single particle of arbitrary size, shape, and composition, subject to the radiation from an external light source, scatters the incident light into other directions. When all other scattering particles are assumed to be sufficiently far away from the particle under investigation such that the scattered

---

´This dissertation follows the style and format of Optics Express.

light will not be scattered again by another particle, we can study the distribution of the light scattered by this single particle at a large distance from the particle. This is called *single scattering*. Detailed discussions on single scattering by small particles can be found in books by, for example, van de Hulst [1], Bohren and Huffman [2], and Mishchenko *et al.* [3].

1. Phase Function

The most important property of the scattered light is its *radiance* I, which is what is detected by the human eyes, or the power per unit area per unit solid angle. For a general scattering particle, the radiance is a function $I = I(\theta, \phi)$ of the scattering angle θ and the azimuthal angle ϕ, as illustrated in Fig. 1.

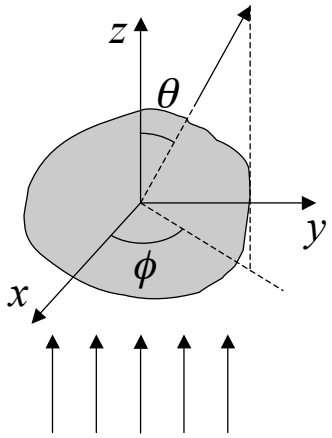

Fig. 1. Geometry of the single scattering.

Let I_0 be the radiance of the incident light, the radiance $I(\theta, \phi)$ of the scattered light along the direction specified by angles θ and ϕ at a large distance r from the scattering particle must be proportional to I_0 and inversely proportional to r^2.

Therefore, it can be written as

$$I(\theta, \phi) = \frac{1}{k^2 r^2} F(\theta, \phi) I_0, \tag{1.1}$$

where $k = 2\pi/\lambda$ is the wave number of the incident light of wavelength λ. Here k is included to make $F(\theta, \phi)$ dimensionless.

We define the *scattering cross section* C_{sca} such that the total energy scattered in all directions is equal to the energy of the incident light falling on the area C_{sca}. Evidently, C_{sca} can be expressed in terms of $F(\theta, \phi)$ as

$$C_{\text{sca}} = \frac{1}{k^2} \int F(\theta, \phi) d\Omega, \tag{1.2}$$

where $d\Omega = \sin\theta d\theta d\phi$ is the element of solid angle, and the integral is over 4π steradians. Similarly, the energy absorbed inside the particle is equal to the energy incident on the *absorbing cross section* C_{abs}, and the energy removed from the original beam is equal to the energy incident on the *extinction cross section* C_{ext}. Energy conservation requires that

$$C_{\text{ext}} = C_{\text{sca}} + C_{\text{abs}}. \tag{1.3}$$

With the scattering cross section, we can also define another function of the scattering direction, the *phase function*, as

$$p(\theta, \phi) = \frac{F(\theta, \phi)}{k^2 C_{\text{sca}}}, \tag{1.4}$$

which is also dimensionless and integrates to unity over 4π steradians. The phase function conveniently describes how the scattered light is distributed in all directions and is extensively used in studies of multiple scattering.

2. Polarized Light

The scattered light, however, contains more information than is sensed by the human eye due to its polarization state, which is the direction of the oscillation of the electromagnetic wave. In the studies of single scattering, we consider a plane wave incident radiation characterized by the electric field

$$\mathbf{E} = \mathbf{E}^i e^{i(\mathbf{k}\cdot\mathbf{r}-\omega t)}. \tag{1.5}$$

It is convenient to choose a *plane of reference* through the direction of propagation $\hat{\mathbf{k}}$, and decompose the electric field $\mathbf{E}$ of the incident light into parallel ($E_\parallel$) and perpendicular ($E_\perp$) components with respect to the plane of reference

$$\mathbf{E}^i = E^i_\parallel \hat{\mathbf{e}}_\parallel + E^i_\perp \hat{\mathbf{e}}_\perp, \tag{1.6}$$

where $E^i_\parallel$ and $E^i_\perp$ are both complex numbers. The sense is chosen such that $\hat{e}_\parallel \times \hat{e}_\perp$ is in the direction of propagation.

For a light beam scattered into the direction (θ, ϕ), we define the plane spanned by the incident beam and the scattered beam as the *scattering plane*, which is a plane of reference for both incident and scattered light beams. As shown in Fig. 2, we can decompose the electric fields of the incident light ($\mathbf{E}^i$) and the scattered light ($\mathbf{E}^s(\theta,\phi)$) with respect to the scattering plane, and relate the two electric fields by a 2×2 *scattering amplitude matrix* $\mathbf{S}(\theta,\phi)$

$$\begin{bmatrix} E^s_\parallel \\ E^s_\perp \end{bmatrix} = \frac{e^{ikr}}{-ikr} \begin{bmatrix} S_2 & S_3 \\ S_4 & S_1 \end{bmatrix} \cdot \begin{bmatrix} E^i_\parallel \\ E^i_\perp \end{bmatrix}, \tag{1.7}$$

where we have suppressed the θ and ϕ dependences of $E^s_\parallel(\theta,\phi)$, $E^s_\perp(\theta,\phi)$, and $S_i(\theta,\phi)$.

The electric field $\mathbf{E}$, however, is a complex number containing an arbitrary phase factor, and would be difficult to measure directly. Therefore, the *Stokes parameters*

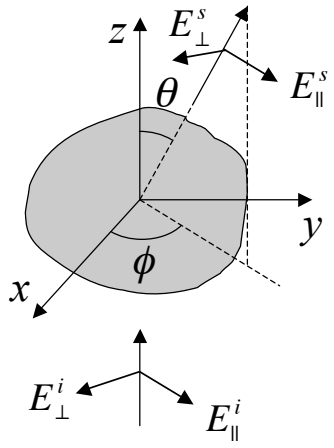

Fig. 2. Illustration of the single scattering for a polarized light.

[4] were introduced and are defined by

$$\begin{aligned} I &= E_\parallel E_\parallel^* + E_\perp E_\perp^*, \\ Q &= E_\parallel E_\parallel^* - E_\perp E_\perp^*, \\ U &= E_\parallel E_\perp^* + E_\perp E_\parallel^*, \\ V &= i(E_\parallel E_\perp^* - E_\perp E_\parallel^*), \end{aligned} \tag{1.8}$$

where an asterisk denotes complex conjugate. They are all real numbers and form a four-component vector $\mathbf{I} = \{I, Q, U, V\}$, also known as the *Stokes vector*. The I component is just the sum of the squares of both parallel and perpendicular components of the electric field, or the total energy carried by the electromagnetic radiation. Obviously, it is the same as the quantity I defined in Eq.(1.1).

To understand what the other three components represent, note that they can

be related to an elliptically polarized light beam as follows [1]

$$\begin{aligned} I &= a^2, \\ Q &= a^2 \cos(2\beta)\cos(2\chi), \\ U &= a^2 \cos(2\beta)\sin(2\chi), \\ V &= a^2 \sin(2\beta), \end{aligned} \tag{1.9}$$

where angles β and χ are as shown in Fig. 3. They are defined such that $-\pi/4 \leq \beta \leq \pi/4$ and $0 \leq \chi < \pi$. Here $|\tan\beta|$ is the ellipticity, and χ is the clockwise angle made by the semi major axis and the plane of reference.

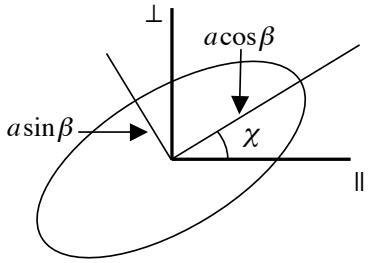

Fig. 3. A general elliptically polarized light beam specified by three parameters, a, β, and χ.

From Eqs.(1.9) and Fig. 3, it is evident that when $V = 0$, $\beta = 0$, the ellipse reduces to a straight line, which corresponds to linear polarization. Under this condition, the Q component relates to the linear polarization of the light field with respect to the plane of reference. A positive Q implies an electric field parallel to the plane of reference, while a negative Q implies an electric field perpendicular to the plane of reference. The U component relates the linear polarization with respect to the planes that are rotated $45°$ and $-45°$ from the plane of reference. Meanwhile, a non-vanishing V component gives information about the circular polarization of the electric field.

For a simple wave, an examination of Eq.(1.8) or Eq.(1.9) reveals that the Stokes parameters satisfy the relation

$$I^2 = Q^2 + U^2 + V^2. \tag{1.10}$$

However, incoherent light consists of many simple waves, each of which with an independent phase factor. A measurable radiance is actually a superposition of the radiance of all simple waves. In this case, the Stokes parameters should be understood as the sums

$$I = \sum_i I_i, Q = \sum_i Q_i, U = \sum_i U_i, V = \sum_i V_i,$$

where i is an index denoting each individual simple wave. The relation Eq.(1.10) now becomes

$$I^2 \geq Q^2 + U^2 + V^2, \tag{1.11}$$

where the equality holds only for fully polarized light.

The Stokes parameters are a complete set of quantities that are needed to characterize the radiance and the state of polarization of a beam of polarized light. This is sometimes referred to as the *principle of optical equivalence*.

Another useful quantity, the degree of polarization (DOP), can be derived from the Stokes parameters as follows:

$$\text{DOP} = \frac{\sqrt{Q^2 + U^2 + V^2}}{I}, \tag{1.12}$$

with DOP = 1 corresponding to fully polarized light and DOP = 0 corresponding to unpolarized or natural light. In all other cases, it is called partially polarized light. Two other useful DOP's are the degree of linear polarization (DOLP), defined by

$$\text{DOLP} = \frac{\sqrt{Q^2 + U^2}}{I}, \tag{1.13}$$

and the degree of circular polarization (DOCP), defined by

$$\text{DOCP} = \frac{|V|}{I}. \tag{1.14}$$

A combination of Eqs.(1.7) and (1.8) implies that the the incident and scattered Stokes vectors can be related by a 4×4 *scattering matrix* $\mathbf{F}(\theta, \phi)$ as

$$\begin{bmatrix} I^s \\ Q^s \\ U^s \\ V^s \end{bmatrix} = \frac{1}{k^2 r^2} \begin{bmatrix} F_{11} & F_{12} & F_{13} & F_{14} \\ F_{21} & F_{22} & F_{23} & F_{24} \\ F_{31} & F_{32} & F_{33} & F_{34} \\ F_{41} & F_{42} & F_{43} & F_{44} \end{bmatrix} \cdot \begin{bmatrix} I^i \\ Q^i \\ U^i \\ V^i \end{bmatrix}, \tag{1.15}$$

where we have suppressed the θ and ϕ dependence of $I^s(\theta, \phi)$, $Q^s(\theta, \phi)$, $U^s(\theta, \phi)$, $V^s(\theta, \phi)$, and $F_{ij}(\theta, \phi)$. Here the full 16 elements of the scattering matrix $\mathbf{F}$ can be expressed in terms of elements of the amplitude matrix $\mathbf{S}$ (see, for example, Ref. [3]). One can immediately recognize that Eq.(1.15) is a direct expansion of Eq.(1.1).

Similar to Eq.(1.2), the scattering cross section for polarized light is given by

$$C_{\text{sca}} = \frac{1}{k^2 I^i} \int [\mathbf{F}(\theta, \phi) \cdot \mathbf{I}^i]_1 d\Omega. \tag{1.16}$$

A normalized scattering matrix, or the *phase matrix* $\mathbf{p}(\theta, \phi)$, can then be defined as

$$\mathbf{p}(\theta, \phi) = \frac{\mathbf{F}(\theta, \phi)}{k^2 C_{\text{sca}}}, \tag{1.17}$$

where the scattering cross section is given by Eq.(1.16). Note here that in the polarized case, $\mathbf{p}(\theta, \phi)$ depends not only on the scattering particle itself, but also on the polarization state of the incident light. In most cases, however, effects of the incident polarization can be neglected.

3. Methods for Single Scattering Calculations

The dependence of the scattering matrix elements F_{ij} on angles θ and ϕ can be obtained by solving the Maxwell equations [5], first proposed by Maxwell in 1865, for the electric field distribution. In SI units, the Maxwell equations can be written as [6]

$$\nabla \cdot \mathbf{D} = \rho, \qquad \nabla \times \mathbf{E} = -\frac{\partial \mathbf{B}}{\partial t}, \tag{1.18a}$$

$$\nabla \cdot \mathbf{B} = 0, \qquad \nabla \times \mathbf{H} = \mathbf{J} + \frac{\partial \mathbf{D}}{\partial t}, \tag{1.18b}$$

where $\mathbf{E}$ and $\mathbf{H}$ are the electric and magnetic fields, respectively; $\mathbf{D}$ and $\mathbf{B}$ are the electric displacement and the magnetic induction, respectively; and ρ and $\mathbf{J}$ are the charge density and current density, respectively. In an electromagnetic medium, $\mathbf{D}$ and $\mathbf{H}$ are related to $\mathbf{E}$ and $\mathbf{B}$ as

$$\mathbf{D} = \epsilon_0 \mathbf{E} + \mathbf{P}, \qquad \mathbf{H} = \frac{\mathbf{B}}{\mu_0} - \mathbf{M}, \tag{1.19}$$

where ϵ_0 and μ_0 are the vacuum permittivity and permeability, respectively, and the electric polarization $\mathbf{P}$ and the magnetization $\mathbf{M}$ describe the response of the medium to an external electromagnetic field.

Eqs.(1.18a) and (1.18b), along with Eq.(1.19), govern the interaction between an incident electromagnetic field and a scattering particle characterized by its size, shape and optical properties, under various boundary conditions. Maxwell's equations can be analytically solved using the separation of variables method, which requires a simple boundary of the particle on which the boundary conditions can be conveniently applied. To date, analytical solutions are only available for scattering particles with a few simple shapes, such as spheres, infinite cylinders, and spheroids.

Several numerical techniques have also be developed to calculate single scattering.

Compared with analytical methods, numerical techniques are more versatile as they can be applied to particles with arbitrary shapes and compositions. The Finite-Difference Time-Domain (FDTD) method [7, 8], the Discrete Dipole Approximation (DDA) method [9], the T-matrix method [10, 11], and the Geometric Optics Method (GOM) [12] are some of the most extensively used numerical methods. The numerical methods, however, are more time-consuming compared with analytical methods.

B. Radiative Transfer

The discussions in the preceding section about single scattering are based on the assumption that the incident light is scattered only once by a single scattering particle. In the real world, however, this assumption does not necessarily hold. In most media, such as the atmosphere and the ocean, there are so many scattering particles packed in a small volume that the incident light will be scattered more than once before it hits a detector. Therefore, the effects of multiple scattering cannot be neglected. An integro-differential equation, the *radiative transfer equation*, is used to study the variation of radiance and polarization of a pencil of light in a turbid medium containing a collection of scattering and absorptive particles. The radiative transfer theory is dedicated to solving the transfer of radiant energy via multiple scattering in these media. Books by Chandrasekhar [13] and Mishchenko *et al.* [14] have given comprehensive reviews on radiative transfer.

1. Radiometry

The science that defines and measures radiant energy is called *radiometry*, which is the cornerstone of radiative transfer studies. Consider an element of area ds with a normal vector $\hat{n}$ and an amount of radiant energy dE within a wavelength range

$(\lambda - d\lambda/2, \lambda + d\lambda/2)$, which is transported across ds in directions confined to an element of solid angle $d\Omega$ centered about the direction $\hat{\xi}$ during a time interval dt, as shown in Fig. 4.

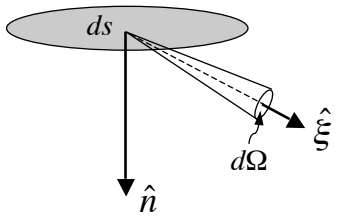

Fig. 4. Definition of radiance.

The fundamental variable of radiometry is the *spectral radiometric radiance* I_λ, defined by [13]

$$I_\lambda = \frac{d^4E}{(\hat{n}\cdot\hat{\xi})d\lambda\ dt\ d\Omega\ ds} \quad \left[\mathrm{W}\cdot\mathrm{m}^{-2}\cdot\mathrm{sr}^{-1}\cdot\mathrm{nm}^{-1}\right], \tag{1.20}$$

which specifies the spatial, temporal, directional, and spectral structure of the light field, and can be used to derive all other radiometric quantities.

However, such complete information about the light field is not needed for many applications. The most commonly measured radiometric quantities are various *irradiances*, which are the integrated radiance over a certain solid angle. The net flux or irradiance with respect to the element of area ds is defined by

$$E_\lambda = \frac{d^3E}{d\lambda\ dt\ ds} = \int_{4\pi} (\hat{n}\cdot\hat{\xi}) I_\lambda d\Omega. \tag{1.21}$$

An irradiance meter, however, will not measure E_λ in Eq.(1.21), but will instead measure the forward and backward plane irradiances, defined by

$$E_\lambda^+ \;=\; \int_{2\pi^+} \left|\hat{n}\cdot\hat{\xi}\right| I_\lambda d\Omega, \tag{1.22a}$$

$$E_\lambda^- = \int_{2\pi^-} \left|\hat{n}\cdot\hat{\xi}\right| I_\lambda d\Omega \tag{1.22b}$$

respectively, where the + refers to the same side of ds as $\hat{n}$, while the − refers to the opposite side. It is obvious that both E_λ^+ and E_λ^- are positive and that $E_\lambda = E_\lambda^+ - E_\lambda^-$.

2. Inherent Optical Properties of a Medium

Before we can write down the equation that governs the radiative transfer in a medium, we need to find out what are the physical processes that transport the light field and introduce the inherent optical properties (IOP) of a medium. Shown in Fig. 5 is a pencil of light with power P incident on a small rectangular volume of a medium with a small thickness dr. A part of the incident power P_a is absorbed by the material in the volume, another part P_s is scattered out of the volume into other directions. The transmitted power can then be expressed by $P + dP$, where

$$dP = -(P_a + P_s) \tag{1.23}$$

is the difference of the radiance after it propagates through the small volume, due to absorption and scattering of the incident radiance by the particles in the volume.

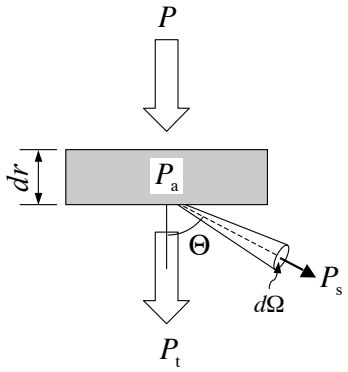

Fig. 5. Diagram used to define IOPs of a scattering and absorptive medium.

We introduce two useful IOPs of the medium, the *absorption coefficient* a and the *scattering coefficient* b, as follows:

$$a = \lim_{dr \to 0} \frac{(P_a/P)}{dr} \quad \left[m^{-1}\right], \tag{1.24a}$$

$$b = \lim_{dr \to 0} \frac{(P_s/P)}{dr} \quad \left[m^{-1}\right]. \tag{1.24b}$$

A third coefficient, the *extinction coefficient* c is defined as

$$c = a + b \quad \left[m^{-1}\right], \tag{1.24c}$$

and characterizes the total fraction of reduction from the incident radiance due to either scattering or absorption. What is more, to describe the fraction of the reduction due to scattering in the total reduction of incident radiance, we introduce the *single scattering albedo* of the medium, ω_0, given by

$$\omega_0 = b/c. \tag{1.25}$$

The quantity ω_0 varies from 0 to 1, where $\omega_0 = 0$ characterizes a purely absorptive medium, while $\omega_0 = 1$ characterizes a purely scattering medium.

To describe how the scattered radiance is distributed in the full 4π solid angle, it is helpful to introduce the *volume scattering function*, defined by

$$p(\theta, \phi) = \lim_{dr \to 0} \lim_{d\Omega \to 0} \frac{P_s(\theta, \phi)/P}{dr d\Omega}. \tag{1.26}$$

One can readily verify that the scattering function integrates to b over the 4π solid angle,

$$\int_{-1}^{1} \int_{0}^{2\pi} p(\theta, \phi) d(\cos\theta) d\phi = b.$$

Another useful IOP of the medium is the normalized scattering function, or the *volume*

phase function $\tilde{p}(\theta, \phi)$ of the medium, which can be obtained by

$$\tilde{p}(\theta, \phi) = \frac{p(\theta, \phi)}{b}. \tag{1.27}$$

Thus far, we have discussed the IOPs for unpolarized light only. In a real medium, the scattering particles are mixed and randomly oriented so that most of the polarization effects average out. However, it is still necessary to consider the polarization properties of the phase function. As in the single scattering studies, the 4-component Stokes vector $\mathbf{I}$ is used to describe the polarization state of a light beam, and a 4×4 *Mueller matrix* $\mathbf{M}$ is used to relate the incident and scattered Stokes vectors,

$$\mathbf{I}_s = \mathbf{M} \cdot \mathbf{I}_i. \tag{1.28}$$

Here we consider a more general case, where an incident light beam along the direction $\mathbf{n}_{\text{inc}} = (\theta, \phi)$ is scattered into the direction $\mathbf{n}_{\text{sca}} = (\theta', \phi')$, as shown in Fig. 6. For

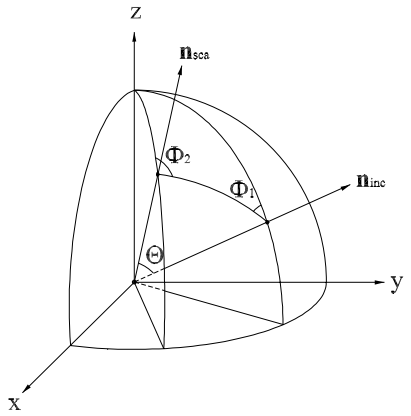

Fig. 6. Geometry of a scattering event for polarized light beams.

consistency, both Stokes vectors are referenced to the *meridian plane*, which is the plane defined by the direction of propagation $\mathbf{n}$ and the z-direction. However, the Mueller matrix is referenced to the scattering plane defined by the two directions of

propagation $\mathbf{n}_{\text{inc}}$ and $\mathbf{n}_{\text{sca}}$. Therefore, the planes of reference for the incident and scattered Stokes vectors must be rotated to the scattering plane,

$$\mathbf{I}_s(\theta', \phi') = \mathbf{L}(\pi - \Phi_2)\mathbf{M}(\Theta)\mathbf{L}(-\Phi_1)\mathbf{I}_i(\theta, \phi), \tag{1.29}$$

where $\mathbf{L}$ is a rotation matrix as follows

$$\mathbf{L}(\pi - \alpha) = \mathbf{L}(\alpha) = \begin{bmatrix} 1 & 0 & 0 & 0 \\ 0 & \cos 2\alpha & -\sin 2\alpha & 0 \\ 0 & \sin 2\alpha & \cos 2\alpha & 0 \\ 0 & 0 & 0 & 1 \end{bmatrix}. \tag{1.30}$$

A normalized Mueller matrix, or a *volume phase matrix* of the small volume of medium, is given by

$$\tilde{\mathbf{M}}(\Theta) = \frac{\mathbf{M}(\Theta)}{b}. \tag{1.31}$$

For a small volume of a homogeneous medium, the volume phase function Eq.(1.27) is identical to the single scattering phase function Eq.(1.4), and the volume phase matrix Eq.(1.31) is identical to the single scattering phase matrix Eq.(1.17). Therefore, they can be conveniently obtained via single scattering studies.

3. The Equation of Transfer

With the three coefficients a, b, and c, the single scattering albedo ω_0, and the volume scattering phase function $\tilde{p}(\theta, \phi)$, we can now write down the equation of transfer for the radiance in a scattering and absorbing medium.

For a pencil of light with power P passing through a small rectangular volume of medium normally as shown in Fig. 5, it is obvious from Eqs.(1.23), (1.24a), (1.24b), and (1.24c) that the difference of the incident power due to absorption and scattering

can be conveniently written in terms of c as

$$dP = -cP\ dr. \tag{1.32}$$

Eq.(1.32) can be alternatively written in terms of radiance I. Since radiance is defined to be power per area per solid angle, it is proportional to the corresponding power given an equal area and an equal solid angle. Therefore, the difference of the incident radiance is

$$dI = -cI\ dr. \tag{1.33}$$

which is proportional to the incident radiance I and the thickness dr of the medium, or the length of path that the radiance passes through.

Besides this reduction, there could also be contribution to the radiance from some sources, such as the scattering of radiation from all other directions into the direction considered in a scattering medium, or the thermal emission in a medium in local thermodynamic equilibrium. This contribution can be accounted for by a *source term* $\mathcal{J}$. Therefore, the *equation of tranfer* can be formulated as

$$\frac{dI}{c\ dr} = -I + \mathcal{J}. \tag{1.34}$$

Now we assume that the amount of radiance being absorbed and scattered are only proportional to the length of path when the radiance passes through the volume, and do not depend on the direction of the incident radiance. Therefore, for a pencil of radiance that propagates along an arbitrary direction specified by angles (θ, ϕ) with respect to the normal of the rectangular volume, Eq.(1.33) becomes

$$dI(\theta, \phi) = -cI(\theta, \phi)dr/\mu, \tag{1.35}$$

where $\mu = \cos\theta$.

A part of this difference, however, will reappear in other directions as sources. It can be noticed that the scattered radiance associated with incident radiance in other directions (θ', ϕ') also has contributions to the radiance in the direction (θ, ϕ), given by the source term

$$\mathcal{J}(\theta, \phi) = \omega_0 \int_{-1}^{1} \int_{0}^{2\pi} \tilde{p}(\theta, \phi; \theta', \phi') I(\theta', \phi') d(\cos\theta') d\phi', \tag{1.36}$$

where $I(\theta', \phi')$ is the incident radiance along a direction specified by (θ', ϕ'), and a reference of the argument of the phase function $(\theta, \phi; \theta', \phi')$ to angle Θ is understood.

A combination of Eqs.(1.34), (1.35) and (1.36) gives the equation of transfer for a pencil of radiance passing through a small rectangular volume of a scattering and absorbing medium

$$\mu \frac{dI(\theta, \phi)}{d\tau} = -I(\theta, \phi) + \omega_0 \int_{-1}^{1} \int_{0}^{2\pi} \tilde{p}(\theta, \phi; \theta', \phi') I(\theta', \phi') d(\cos\theta') d\phi', \tag{1.37}$$

where

$$d\tau = c \; dr$$

is the *optical thickness* of the small volume. Eq.(1.37) is an integro-differential equation in terms of the radiance $I(\theta, \phi)$.

To describe the radiative transfer of polarized light, it is necessary to replace the source term Eq.(1.36) with its vector form

$$\mathcal{J}(\theta, \phi) = b \int_{-1}^{1} \int_{0}^{2\pi} \tilde{\mathbf{M}}(\theta, \phi; \theta', \phi') \mathbf{I}(\theta', \phi') d(\cos\theta') d\phi', \tag{1.38}$$

where

$$\tilde{\mathbf{M}}(\theta, \phi; \theta', \phi') = \mathbf{L}(\pi - \Phi_1) \tilde{\mathbf{M}}(\Theta) \mathbf{L}(\Phi_2). \tag{1.39}$$

The vector form of Eq.(1.37) now assumes the form:

$$\mu \frac{d\mathbf{I}(\theta,\phi)}{d\tau} = -\mathbf{I}(\theta,\phi) + \omega_0 \int_{-1}^{1}\int_{0}^{2\pi} \tilde{\mathbf{M}}(\theta,\phi;\theta',\phi')\mathbf{I}(\theta',\phi')d(\cos\theta')d\phi', \tag{1.40}$$

Eq.(1.40) governs the transfer of polarized light through a small volume in a scattering and absorbing medium. As can be seen in this equation, all information about this small volume of medium are given by the single scattering albedo ω_0 and the volume phase matrix $\tilde{\mathbf{M}}(\theta,\phi;\theta',\phi')$.

This equation, however, can be very inconvenient to use in an inhomogeneous medium, as both ω_0 and $\tilde{\mathbf{M}}(\theta,\phi;\theta',\phi')$ could be a function of the position of the small volume in the medium. Assumptions have been made to make things easier. The most extensively studied radiative transfer model is the plane parallel model, which assumes a medium that consists of stratified horizontal layers. Therefore, ω_0 and $\tilde{\mathbf{M}}(\theta,\phi;\theta',\phi')$ are both functions of the accumulated optical depth τ measured from the boundary of the medium, and Eq.(1.40) can be used as an equation of transfer for the whole medium. This model has been widely used to simulate more sophisticated scattering media, such as atmospheres and oceans, and has shown great potential in giving reasonable results.

4. Methods for Radiative Transfer

A solution to the equation of transfer Eq.(1.40) is only available in a discretized fashion. Several approaches have been reported for plane-parellel media. In his 1950 book, Chandrasekhar [13] introduced the quadrature formulae, which solves Eq. (1.40) by replacing the integro-differential equation with a system of linear equations, which can be regarded as a matrix equation. Twomey *et al.* [15, 16] reported their studies on the matrix method, which is later referred to as the *adding-doubling* method. Plass and Kattawar [17, 18] gave a clear physical interpretation of this matrix method, which

they called the *matrix operator* theory. These authors further improved the algorithm and applied it to scattering media with larger optical depths and anisotropic scattering phase functions. Stamnes *et al.* [19] also developed an algorithm based on the matrix method, which they referred to as the *discrete-ordinate-method*. A computer code based on this method, the DIScrete Ordinate Radiative Transfer (DISORT) [20] program, is publicly available, and has been widely used in the community of atmospheric sciences and remote sensing.

An alternative method to study radiative transfer is the Monte Carlo (MC) method, which simulates the multiple scattering of light in a scattering and absorbing medium not by solving the equation of transfer Eq.(1.40), but instead by tracing the trajectories of photons, or groups of photons, and their interaction with particles. The MC method is a statistical method, which gives precise results when the number of photons traced is large enough. The advantage of the MC method over other methods is that the MC method is more versatile as it can conveniently handle media with arbitrary boundaries and/or more variations of optical properties.

CHAPTER II

APPLICATIONS OF THE GENERALIZED DDA FORMALISM

A. The Discrete Dipole Approximation Method

The Discrete Dipole Approximation (DDA) is a powerful numerical method for computation of scattering and absorption of electromagnetic radiation by particles of arbitrary shape and composition. Initially suggested by Purcell and Pennypacker [9] in 1973, the DDA represents a scattering particle in terms of a collection of point-like dipoles. Each dipole undergos forced oscillations in response to incident radiation and the field induced by all other dipoles. Solution to a self-consistent set of linear equations gives all dipole moments, which in turn provide information for computations of various quantities of interest.

The DDA method was popularized by Draine and Flatau [21, 22] in the late 1980's, who developed and kept maintaining a publicly available computer code `DDSCAT` [23], which has been widely used. Another computer code using the DDA formalism, the `ADDA` (the Amsterdam DDA) [24], has been made public recently by Yurkin *et al.* This code allows simulation of light scattering by larger particles due to its ability to parallelize the DDA simulation of a single particle. A detailed comparison between these two codes and two non-publicly-available DDA codes, the `SIRRI` and the `ZDD`, has been presented [25]. Yurkin and Hoekstra [26] gave a review on the DDA method and its recent developments.

1. The Discrete Dipole Scheme

A dielectric particle consists of a large number of molecules. The internal charge distribution within each individual molecule will be altered once it is subject to an

external electric field $\mathbf{E}$. In other words, there will be a molecular dipole moment $\mathbf{P}_{\text{mol}}$

$$\mathbf{P}_{\text{mol}} = \bar{\bar{\alpha}}_{\text{mol}} \cdot \mathbf{E}$$

induced by the external electric field, where $\bar{\bar{\alpha}}_{\text{mol}}$ is the molecular polarizability tensor. If the dielectric particle is subject to electromagnetic radiation, i.e., an oscillating electromagnetic wave, the molecular dipole moments will also oscillate and radiate electromagnetic fields. At the microscopic molecular scale, this is exactly how a dielectric particle responds to electromagnetic radiation and scatters/absorbs the incident radiation.

Following the molecular scenario comes the idea of simulating the response of a dielectric particle, which in principle is a huge number of microscopic molecules, by that of a collection of point-like dipoles. In the discrete dipole scheme, a solid particle is replaced by a simple cubic array of N point-like dipoles undergoing forced oscillations, as Fig. 7 illustrates.

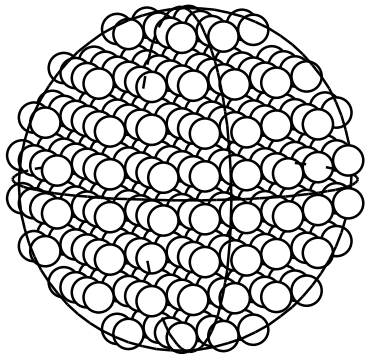

Fig. 7. Representation of a spherical particle in the Discrete Dipole scheme.

In a real computation, the number density of DDA dipoles is much smaller than

that of the real molecular dipoles. Therefore, each individual dipole effectively represents all molecules in the small cell in its immediate vicinity. The DDA dipole at the jth occupied lattice site is characterized by a polarizability tensor $\bar{\bar{\alpha}}_j$, which is the averaged molecular polarizability tensor in its immediate vicinity. The DDA dipole moment can then be written as

$$\mathbf{P}_j = \bar{\bar{\alpha}}_j \cdot \mathbf{E}_{\text{ext},j}, \tag{2.1}$$

where $\mathbf{P}_j$ is the dipole moment of the DDA dipole at lattice site j, or the dipole moment density of the molecular dipoles in the corresponding lattice cell, and $\mathbf{E}_{\text{ext},j}$ is the electric field density at this lattice site due to the incident radiance as well as all other $N-1$ oscillating dipoles. Hereafter, we will refer to the DDA dipole and the DDA dipole moment as the dipole and the dipole moment, respectively.

To make the discrete dipole scheme work properly, it is necessary to determine the polarizability tensors $\bar{\bar{\alpha}}_j$ according to the material properties of the scattering particle. In Purcell and Pennypacker's study, the Clausius-Mossotti relation was used to relate $\bar{\bar{\alpha}}_j$ with the macroscopic electric permittivity $\bar{\bar{\epsilon}}_j$ of the dielectric:

$$\bar{\bar{\alpha}}_j^0 = \frac{3}{4\pi n} \frac{\bar{\bar{\epsilon}}_j - 1}{\bar{\bar{\epsilon}}_j + 2}, \tag{2.2}$$

where n is the number density of dipoles. Eq.(2.2) holds exactly only at zero frequency $kd = 0$, where k is the wavenumber of the incident radiation, and d is the inter-dipole spacing. Draine [21] introduced a correction due to the radiative reaction [6] into the discrete dipole calculation, and suggested the polarizability

$$\bar{\bar{\alpha}}_j = \frac{\bar{\bar{\alpha}}_j^{(\text{nr})}}{1 - (2/3)ik^3 \bar{\bar{\alpha}}_j^{(\text{nr})}}, \tag{2.3}$$

where the "nonradiative" polarizability $\bar{\bar{\alpha}}_j^{(\text{nr})}$ was assumed to be $\bar{\bar{\alpha}}_j^0$. Draine and Good-

man [27] further investigated the problem that, for what polarizability $\alpha(\omega)$ will an infinite lattice of polarizable points have the same dispersion relation as a continuum of permittivity $\epsilon(\omega)$, and proposed the lattice dispersion relation (LDR) which relates the nonradiative polarizability $\bar{\bar{\alpha}}^{(\mathrm{nr})}$ and the Clausius-Mossotti polarizability $\bar{\bar{\alpha}}^{0}$ as follows:

$$\bar{\bar{\alpha}}^{(\mathrm{nr})} = \frac{\bar{\bar{\alpha}}^{0}}{1+(\bar{\bar{\alpha}}^{0}/d^3)(b_1+\bar{\bar{\epsilon}}b_2+\bar{\bar{\epsilon}}b_3 S)(kd)^2}, \tag{2.4a}$$

$$b_1 = -1.8915316, \quad b_2 = 0.1648469, \quad b_3 = -1.7700004, \tag{2.4b}$$

$$S = \sum_{j=1}^{3} \left(\hat{a}_j \hat{e}_j\right)^2, \tag{2.4c}$$

where $\hat{a}$ and $\hat{e}$ are unit vectors of the propagating direction and the polarization state of the incident radiation. Eq.(2.4a) is only valid in the low-frequency limit $kd \ll 1$. The dipole moment $\mathbf{P}_j$ given by Eqs.(2.1), (2.3), (2.4a), (2.4b) and (2.4c) determines the response of the jth dipole to the external radiation.

2. Formulation of the Scattering Problem

The desired self-consistant set of equations for $\mathbf{P}_j$ is obtained by writing $\mathbf{E}_{\mathrm{ext},j}$ in Eq.(2.1) explicitly, which gives

$$\mathbf{P}_j = \bar{\bar{\alpha}}_j \cdot \left(\mathbf{E}_{\mathrm{inc},j} - \sum_{k \neq j} \mathbf{A}_{jk}\mathbf{P}_k \right), \tag{2.5}$$

where $\mathbf{E}_{\mathrm{inc},j}$ is the electric field at lattice site j due to the incident radiance, and $-\mathbf{A}_{jk}\mathbf{P}_k$ is the contribution from the oscillating dipole at the lattice point k, $\mathbf{P}_k$, given by

$$\begin{aligned} \mathbf{A}_{jk}\mathbf{P}_k \;=\; & \frac{\exp(ikr_{jk})}{r_{jk}^3}\Big\{ k^2 \mathbf{r}_{jk} \times (\mathbf{r}_{jk} \times \mathbf{P}_k) + \\ & \frac{(1-ikr_{jk})}{r_{jk}^2}\left[r_{jk}^2 \mathbf{P}_k - 3\mathbf{r}_{jk}\left(\mathbf{r}_{jk}\cdot\mathbf{P}_k\right)\right]\Big\}, \end{aligned} \tag{2.6}$$

with $\mathbf{r}_{jk} = \mathbf{r}_j - \mathbf{r}_k$. We can then define an $N \times N$ matrix $\mathbf{A}$, each element of which is again a 3×3 matrix, with its off-diagonal elements determined by Eq.(2.6) and diagonal elements given by

$$\mathbf{A}_{jj} = \bar{\bar{\alpha}}_j^{-1}. \tag{2.7}$$

The scattering problem can now be formulated in a compact set of N linear equations in terms of $\mathbf{P}_k$:

$$\sum_{k=1}^{N} \mathbf{A}_{jk}\mathbf{P}_k = \mathbf{E}_{\mathrm{inc},j}, \tag{2.8}$$

where both $\mathbf{A}_{jk}$ and $\mathbf{E}_{\mathrm{inc},j}$ are known variables.

The scattering problem now becomes a problem of solving for the unknown dipole moments $\mathbf{P}_j$ in the matrix equation Eq.(2.8). Various numerical techniques, such as the Complex Conjugate Gradient (CCG) [21] method and the Fast Fourier Transform (FFT) [28], are used to expedite the solution of this matrix equation.

3. Applications of the DDA Method

Purcell and Pennypacker introduced the discrete dipole method in order to investigate light scattering and absorption by intersteller dust grains with arbitrary shape in the visible and ultraviolet wavebands. Draine and Flatau developed the `DDSCAT` code in order to study intersteller graphite grains. This versatile method has also found its applications in various disciplines. In nanotechnology, it has been used to calculate surface enhanced Raman scattering [29]; in atmospheric sciences, it has been used to simulate light scattering from ice and snow particles at high microwave frequencies [30]; in biomedical sciences, it has been used to calculate light scattering from a single erythrocyte (red blood cell) [31].

To date, however, applications of the DDA method have been limited to the interaction between an incident plane wave and dielectric particles, i.e., particles that

have only an electric response to the incident radiation. DDA calculations involving incident radiation other than a plane wave have not been reported; nor has DDA calculations involving scattering particles with both electric and magnetic responses been reported. In the following sections, the conventional DDA formalism will be generalized to cases involving an incident field from radiating dipoles or scattering particles with magnetic responses. Applications of the generalized DDA formalisms to calculations of inelastic scattering and simulation of invisibility cloaks will be presented.

B. Application of the DDA Method to Inelastic Scattering*

In the process of light scattering, a major fraction of the incident photons are elastically scattered, in which case there is no energy exchange between the incident photons and the material molecules. Therefore, a scattered photon has the same amount of energy as an incident photon. Meanwhile, a small fraction of the incident photons will be turned into scattered photons with shifted energy or frequency as they lose a part of electromagnetic energy in the material molecules or gain extra electromagnetic energy from the material molecules. This is inelastic scattering phenomena.

The two most studied and useful inelastic scattering processes are Raman scattering and fluorescence. First discovered by and named after C. V. Raman [32], Raman scattering involves interactions between a fraction of the incident light and molecules in the target particle that move back and fourth around an equilibrium location. The vibrational or rotational energy of a molecule may be changed upon

*Part of the data reported in this section is reprinted with permission from "Internal dipole radiation as a tool for particle identification", Y. You, G. W. Kattawar, C. Li, and P. Yang, Appl. Opt. **45,** 9115-9124 (2006). Copyright 2006 by Optical Society of America.

the incident light, which leads to an excitation in the energy state of the molecule and an energy shift in the Raman-scattered light. The fraction of the incident light involved in Raman scattering, however, is on the order of 10^{-6}. The Raman spectroscopy technique based on Raman scattering has been extensively used in a variety of disciplines, e.g., chemistry and material analysis.

Fluorescence also involves an energy shift in the scattered light and excitation of the material molecules. In this case, however, an incident photon is completely absorbed by a molecule while the molecule is transferred to an excited state. The excited molecule can then be transferred to lower states after a certain resonance lifetime. Fluorescence has been used to identify host particles in various disciplines, such as analytic chemistry, biochemistry, medicine, and mineralogy.

Most studies on angular dependence of light scattering have been focused on elastic scattering. It has been shown that the elastic-scattering patterns contain useful information about the scattering particle, such as its shape, size, and composition. Therefore, it has been used as a diagnostic tool to identify various particles. angular dependence of inelastic scattering, on the contrary, has received less attention. However, for particles with inclusions, the inelastic-scattering pattern provides additional information about the composite of the host particle. Therefore, simulation of inelastic scattering is also of great interest.

1. Model for Inelastic Scattering

Based on the fact that the inelastic scattering is essentially light scattering from oscillating molecules embedded in the host particle, Chew *et al.* [33] suggested a model to study inelastic scattering quantitatively. Their idea was similar to that of the DDA method, to represent an active molecule by a point-like dipole undergoing forced oscillations characterized by an effective polarizability α according to the local

exciting field at the incident frequency. Chew and colleagues have reported analytical solutions to the radiation from a single internal dipole embedded in spherical host particles [33, 34], cylindrical host particles [35] and spheroidal host particles [36].

Following this model, the angular dependence of inelastic-scattered light can be simulated by a superposition of the scattered fields associated with a distribution of oscillating point dipoles embedded in the host particle. Chew *et al.* [37, 38] reported numerical results of inelastic scattering from a distribution of active molecules embedded in dielectric spheres. Numerical results for spherical host particles with a broader range of refractive indexes and larger size parameters were reported in a later study [39]. The formulae used in these studies have been improved [40, 41], and similar results have been obtained. In these studies, the probability that an active molecule is raised to the excited state is assumed to be proportional to the square of the magnitude of the local exciting field at the incident frequency and proportional to the number density of active molecules at this location. It was also assumed that the dipole moment of an active molecule is induced in the direction parallel to the local exciting field.

There are two optical processes involved in the superposition of contributions from individual active molecules. For spontaneous Raman emission and fluorescence, there is an arbitrary phase factor associated with the oscillation of each active molecule. Therefore, the radiation from each individual excited molecules adds *incoherently*, i.e., the time averaged power over the particular distribution of molecules should be added up, giving the total radiated power. On the contrary, in stimulated Raman scattering, the radiation from each individual excited molecules adds *coherently*, i.e., the radiated fields themselves should be added to obtain the total radiated field, from which a time averaged power is easy to obtain. Numerical results of both incoherent [37, 39] and coherent [38] inelastic scattering from homogeneously

distributed active molecules embedded in a spherical particle have been reported.

Numerical solutions to the inelastic-scattering problem using other methods have also been reported. Zhang and Alexander [42, 43] proposed a hybrid method for spherical particles, in which the Lorenz-Mie theory was used to determine the exciting field and the GOM was used to solve for the inelastic-scattered field. Velesco and Schweiger [44] and Weigel *et al.* [45] reported a more efficient method to calculate inelastic scattering by large spherical particles using the reversed-ray-tracing (RRT) technique. The RRT technique was further used [46] to investigate the shape effect of inelastic scattering by large particles. The GOM approach, however, gives accurate results only for large scattering particles and does not work well for small particles with size parameters ($x = 2\pi a/\lambda$ where a is the effective radius or the radius of an equal-volume-sphere and λ is the wavelength of the incident light) less than 20, which are of great interest in particular cases. The spores of *Bacillus megaterium*, *Bacillus cereus*, and *Bacillus anthracis*, for example, usually have size parameters less than 10 for 0.5 μm incident light [47].

One should realize that, in order to use this model to calculate real inelastic scattering, the shift in the frequency must be prescribed by other means, as the model itself provides no information about the energy shift.

2. DDA Formalism for Internal Dipole Radiation

Before we can simulate inelastic scattering using the DDA method, it will be helpful to present how to calculate the radiation from a single internal oscillating dipole (hereafter referred to as the *source dipole*) using the DDA formalism. As the current DDA formalism treats a dielectric particle as an array of electric dipoles (hereafter referred to as the *induced dipoles*) induced by an incident field, it may be the most straightforward numerical technique for computation of internal dipole radiation with

a source dipole embedded in a dielectric particle. Instead of a plane-wave incident field for $\mathbf{E}_{\text{inc},j}$ in Eq.(2.8), now the incident field is the electric field radiated by an electric dipole, given by [6]

$$\mathbf{E}_{\text{inc},j} = \frac{e^{ikr_j}}{r_j^3}\left\{k^2(\mathbf{r}_j \times \mathbf{P}_0) \times \mathbf{r}_j + \frac{1-ikr_j}{r_j^2}\left[3\mathbf{r}_j(\mathbf{r}_j \cdot \mathbf{P}_0) - \mathbf{P}_0 r_j^2\right]\right\}, \tag{2.9}$$

where $\mathbf{P}_0$ is the dipole moment of the source dipole, and $\mathbf{r}_j$ is the position vector measured from the source dipole to the location where the electric field is observed. The source dipole is assumed to be oscillating at the excited frequency.

This incident field being established, it is straightforward to apply the conventional DDA formalism by solving Eq.(2.8) for dipole moments $\mathbf{P}_j$ of all induced dipoles, with $\mathbf{E}_{\text{inc},j}$ given by Eq.(2.9). Notice here that, as the source dipole itself is excited by external fields and is used to generate the incident field in this calculation, it is regarded as a hard source and its dipole moment $\mathbf{P}_0$ is not included in the self-consistent system of dipole moments described by Eq.(2.8). Given all this information, the resultant field is the superposition of fields radiated by the source dipole and all induced dipoles, and the radiated power at a large distance can be formulated as

$$\frac{dP}{d\Omega} = \frac{c^2 Z_0}{32\pi^2}k^4\left|\sum_{j=0}^{N}\left[\mathbf{P}_j - \hat{\mathbf{n}}\left(\hat{\mathbf{n}} \cdot \mathbf{P}_j\right)\right]\exp\left(-ik\hat{\mathbf{n}} \cdot \mathbf{r}_j\right)\right|^2, \tag{2.10}$$

where $Z_0 = \sqrt{\mu_0/\epsilon_0}$ is the impedance of free space, and $\hat{\mathbf{n}}$ is the unit vector in the direction of radiation. $j = 0$ is the contribution from the source dipole, and $j = 1, \cdots, N$ collects the contribution from all induced dipoles.

As aforementioned, the DDA formalism models a continuous dielectric in terms of an array of dipoles by relating the macroscopic dielectric constant of the medium and the microscopic polarizabilities of the induced dipoles using the Clausius-Mossotti

relation. This introduces the local-field effects [48] when applied to problems involving internal sources. According to these effects, a dipole embedded inside a dielectric medium changes the local field in its immediate proximity. Therefore, the electric field that the dipole sees is not equivalent to the macroscopic field. Consequently, the power P radiated by a dipole $\mathbf{p}$ considering the local-field effects and the power P_0 radiated by the same dipole without the local-field effects can be related as $P = \mathcal{L}^2 P_0$ [49], where $\mathcal{L}$ is the local field cavity factor. To compensate these effects, it is necessary to rescale the source dipole in the DDA calculations. For example, if we want a unit dipole, we should specify the source dipole $|\mathbf{p}| = \mathcal{L}^{-1}$ in the DDA computation.

To couple an extra source dipole with an array of induced dipoles in the DDA computation, it is also important to specify the location of the source dipole with proper consideration of symmetry. In the DDA formalism, the fields are computed only at the lattice points of the 3D dipole array. These fields are supposed to be, or close to, the averaged value of fields in the vicinity of the corresponding dipoles. For an incident plane wave, the field is slowly varying within a scale smaller than the wavelength. Therefore, this condition is always satisfied. The field radiated by a dipole, on the contrary, varies dramatically in the proximity of itself. Thus in the vicinity of the source dipole, the induced dipoles should be symmetrically distributed around it so that a symmetric field can be properly approximated by the DDA dipoles. Figure 8 shows the two schemes that satisfy this symmetry requirement. In the *interstitial* scheme, the source dipole is surrounded by eight neighboring induced dipoles. In the *subsbitutional* scheme, the location of the source dipole overlaps with that of an induced dipole. For any scheme other than these two, the fields on DDA lattice sites cannot give a symmetric approximation to the incident field in the vicinity of the source dipole.

Furthermore, the conventional DDA formalism was developed to account for an

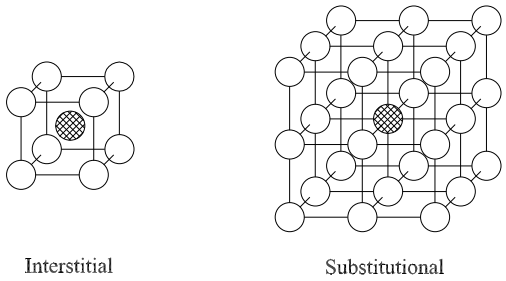

Fig. 8. Two schemes of the coupling between the DDA dipole lattice and the source dipole, where the shadowed circle represents the source dipole, and the open circles represent the induced dipoles.

incident plane wave that does not have a singularity. However, it is obvious from Eq. (2.9) that the field radiated by an electric dipole has a singularity that varies as $\mathbf{E} \propto r^{-3}$ as $r \to 0$. As a result, the numerical computation can be unstable due to the singularity of the incident field at the singularity point if there is an induced dipole near the source dipole. Therefore, it is necessary not to locate the source dipole in the immediate proximity of an induced dipole. In this sense it is necessary to exclude the induced dipole right at the location of the source dipole if the substitutional scheme is employed. This requirement essentially changes the morphology of the dielectric particle by introducing a cubic cavity of a volume of d^3 around the source dipole. Before we continue to discuss the choice of schemes, a brief review of the cavity factor $\mathcal{L}$ is necessary.

Böttcher [48] studied the local-field effects by assuming a cavity of radius r and an oscillating dipole with polarizability α inside it. The microscopic radius r is given by Onsager's approximation $(4\pi/3)nr^3 = 1$, where n is the number density of the dielectric molecules. For this general case, the cavity factor is given by

$$\mathcal{L} = \frac{3\epsilon}{2\epsilon + 1 - 2\frac{\alpha}{r^3}(\epsilon - 1)}, \tag{2.11}$$

where ϵ is the relative permittivity, or the dielectric constant, of the dielectric particle. For a homogeneous system [50] where the source dipole is the same as the induced dipoles, the Clausius-Mossotti relation gives $(4\pi/3)n\alpha = (\epsilon - 1)/(\epsilon + 2)$, therefore Eq.(2.11) reduces to the Lorentz *virtual-cavity* factor

$$\mathcal{L}_{\text{virtual}} = \frac{\epsilon + 2}{3}, \tag{2.12}$$

which was proposed by Lorentz [51] who assumed a virtual cavity around the source dipole, with the same refractive index $m = \sqrt{\epsilon}$ both inside and outside the cavity. While for an inhomogeneous system [52, 53] where the polarizability density of the excited molecule is much lower than that of the dielectric molecules, i.e., $(4\pi/3)n\alpha \ll (\epsilon - 1)/(\epsilon + 2)$, Eq.(2.11) reduces to the Onsager-Böttcher *empty-cavity* factor

$$\mathcal{L}_{\text{empty}} = \frac{3\epsilon}{2\epsilon + 1}. \tag{2.13}$$

which was proposed by Böttcher who assumed a very small empty cavity around the source dipole. In our dipole radiation, the oscillating dipole is the same as the media dipoles, therefore the virtual-cavity model is appropriate to describe the situation. So we chose the cavity factor $\mathcal{L}_{\text{virtual}}$ in our calculations.

It is obvious that the interstitial scheme corresponds to the virtual-cavity model, since in this case the source dipole is placed between the lattice of the induced dipoles, thus it can be interpreted that around the source dipole there is a very small virtual cavity, with refractive index m both inside and outside. So we choose the cavity factor $\mathcal{L}_{\text{virtual}}$ for the interstitial scheme. While for the substitutional scheme, by replacing an induced dipole with the source dipole, we introduced a macroscopic cubic cavity with a finite edge equal to the diameter of a lattice dipole d, which is not the same situation as Eq.(2.11) was based on. However, we can approximate the cubic cavity with an equal-volume-spherical cavity with radius $r'^3 = (6/\pi)r^3$. Substituting r'^3 into

Eq.(2.11), we have the cavity-factor associated with this computational scheme

$$\mathcal{L}_{\text{sub}} = \frac{3\epsilon}{2\epsilon + 1 - \frac{\pi}{3}\frac{(\epsilon-1)^2}{\epsilon+2}}. \tag{2.14}$$

To validate the efficacy of the DDA formalism for internal dipole radiation, we first compared the DDA results with the analytical counterpart for spherical particles, which has been given by Chew *et al.* [33]. In the comparison, the oscillating source dipole is assumed to have a unit dipole moment. To compare with analytic results, we want to locate the source dipole on the center of symmetry and also on an axis of symmetry. Therefore, as can be seen in Fig. 8, in the interstitial scheme, we want the center of a lattice cell at the center of symmetry, and then we would have equivalent numbers of induced dipoles on both sides of the interstitial dipole, so we need an even number of induced dipoles along each dimension. While, in the substitutional scheme, we want a substitutional dipole at the center of symmetry, and again equivalent numbers of induced dipoles on both sides, so we need an odd number of induced dipoles along each dimension.

Firstly, to compare the two schemes shown in Fig. 8, we considered a source dipole located at the center of the spherical particle and oscillating along the z direction. We computed the normalized radiated power P/P_0 (defined as the power radiated by the source dipole in the presence of the host particle divided by that radiated by the same source dipole in the absence of the host particle), where P_0 is given by [6]

$$P_0 = \frac{c^2 Z_0 k^4}{12\pi}|\mathbf{P}_0|^2. \tag{2.15}$$

The simulated results for both schemes, as well as corresponding relative errors, are shown in Fig. 9.

Figure 9(a) shows the results for a spherical particle with a size parameter of

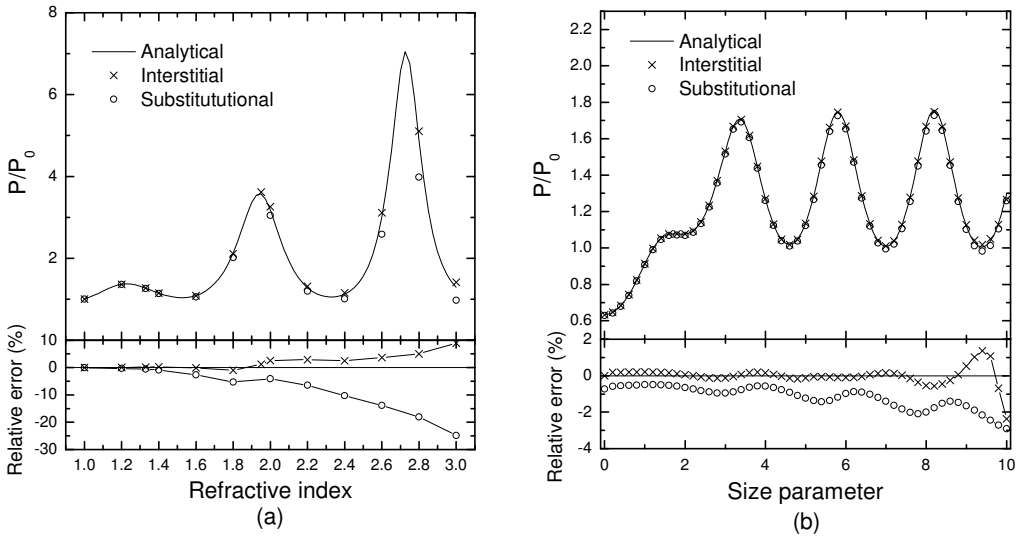

Fig. 9. Comparisons of the normalized radiated power computed from interstitial and substitutional schemes in Fig. 8, with a unit source dipole located at the center: (a) radiated power versus the refractive index of the host particle with a size parameter $ka = 4$; (b) radiated power versus the size parameter of the host particle with a refractive index $m = 1.33$.

$ka = 4$, where a is the radius of the spherical particle and a refractive index varying from $m = 1$ to 3. Obviously the results computed from the interstitial scheme are more accurate than those from the substitutional scheme. Both schemes give accurate results for refractive index $m < 1.4$. The relative error associated with the interstitial scheme is less than 1% for refractive index $m < 2.0$, and less than 5% for $m \leq 2.6$. While the relative error associated with the substitutional scheme increases to around 5% for $m = 1.8$, and continues to increase dramatically. Figure 9(b) shows the results for a spherical particle with a fixed refractive index of $m = 1.33$, and a size parameter varying from $ka = 0.2$ to 10. Again, we notice that the interstitial scheme gives more accurate results than the substitutional scheme does. We feel that the larger errors for the substitutional scheme come from approximating a spherical cavity by a cubic cavity. Hereafter, we will only use the interstitial scheme in our studies. For

the purpose of validation, in this section the refractive index of the particle for the simulation is always chosen to be $m = 1.33$, which represents a moderately polarizable and non-absorbing case.

Secondly, to show the effect of the location of the source dipole in the DDA lattice, test cases are simulated pertaining to a spherical particle with a size parameter $ka = 8$. A source dipole is placed on and oscillating along the z-axis. In the test runs, the position of the source dipole is varied from the center of one cubic lattice to the center of an adjacent cubic lattice as $z = a/2 + \alpha d$, where $0 \leq \alpha \leq 1$, and d is the inter-dipole spacing. A comparison between the DDA results and the analytical results is shown in Fig. 10, where Fig. 10(a) shows the normalized radiated power as a function of α, and Fig. 10(b) shows the radiated power per solid angle when the source dipole is located at the midpoint of the two centers of the cube ($\alpha = 0.5$).

Figure 10(a) reveals that the DDA gives a correct value of radiated power only when the source dipole is located in the proximity of the center of a lattice cell. When the source dipole is away from this point, the relative errors of the DDA results are considerable and can be up to 66%. It can be found in Fig. 10(b) that, however, the DDA simulation still gives a correct shape of the radiation pattern although the simulated radiated power per solid angle is $65\% - 67\%$ lower than the analytical solution. Again, the results shown in Figs. 9 and 10 confirm that the interstitial scheme is appropriate for the application of the DDA method to internal dipole radiation calculations.

3. Accuracy of DDA Results for Internal Dipole Radiation

To investigate the accuracy of the DDA formalism in more general cases, we computed P/P_0 for a source dipole located at various positions inside and at the surface of spherical particles with size parameters of $ka = 8$ and 20. Since the particles are

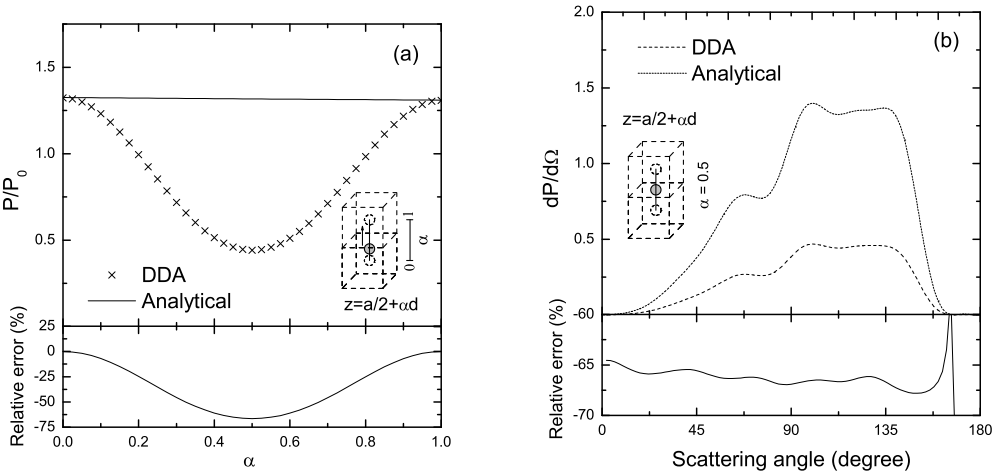

Fig. 10. Radiated power when the source dipole is located off the center of a cell, for a spherical particle of size parameter $ka = 8$, a refractive index of $m = 1.33$, and a source dipole located on and oscillating along the z direction: (a) normalized radiated power when the source dipole is moved from the center of one cell to the center of an adjacent cell, $0 \leq \alpha \leq 1$; (b) radiated power per solid angle versus the scattering angle θ when the source dipole is at the midpoint of the two centers of cell $\alpha = 0.5$.

spherically symmetric, we can always choose a proper coordinate system such that the source dipole is located on the z-axis. The source dipole is then specified to oscillate along either the z or the x direction, corresponding to radially and tangentially oriented cases, respectively. Here, we use $mkd = 0.3324$ for the numerical simulation in the case of $ka = 8$ and $mkd = 0.5541$ in the case of $ka = 20$. The results given by both the analytical and the DDA methods are shown in Fig. 11, where the symbols represent the results from the DDA calculation, and solid curves represent the results from the analytical method. The corresponding relative errors are also shown in Fig. 11.

Evidently, for a source dipole embedded inside a spherical particle with a size

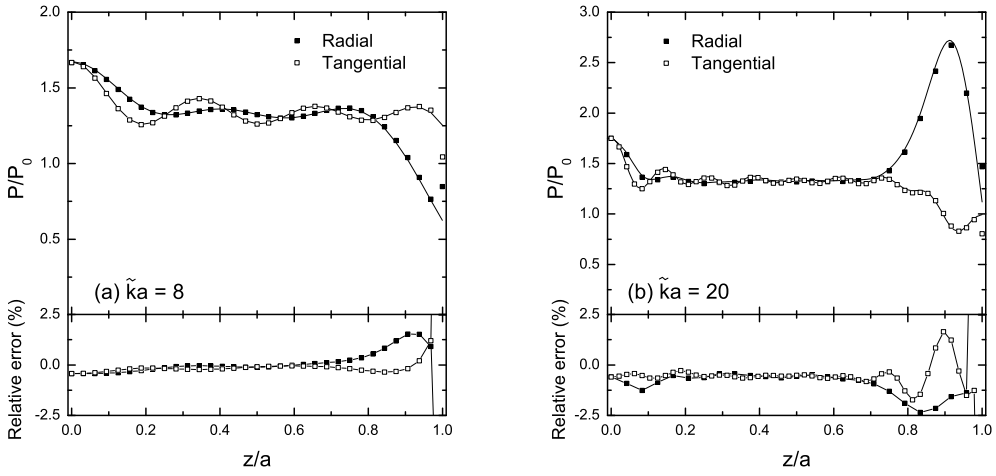

Fig. 11. Normalized radiated power versus the location of the source dipole computed from the DDA and analytic methods. The source dipole is located on the z-axis and oscillates along either the z or x direction, corresponding to radially or tangentially oriented dipoles. Size parameters (a) $ka = 8$ and (b) $ka = 20$, and refractive index $m = 1.33$ are chosen for the spherical host particle.

parameter up to 20, the normalized radiated power computed from the DDA agrees quite well with that predicted by the analytical approach. The relative errors are within $\pm 2.5\%$. However, if the source dipole is on the surface of the particle, the DDA solution is substantially inaccurate, and the relative errors can be up to $\pm 30\%$.

We also compared the radiated power per solid angle ($dP/d\Omega$) as a function of the scattering angle, i.e., the radiation pattern. For a source dipole in the absence of the host particle, the result is well-known, and is given by [6]

$$\frac{dP}{d\Omega} = \frac{c^2 Z_0}{32\pi^2} k^4 |\mathbf{p}|^2 \sin^2\theta, \tag{2.16}$$

where θ is measured from the direction of the dipole oscillation.

For the simulation, a source dipole is specified on the z-axis at $z/a = 1/4, 1/2, 3/4$, and 1, oscillating along the z or x direction. For radially oriented cases, there is a

rotational symmetry with respect to the z-axis, which implies that the radiation pattern is the same for all values of angle ϕ. For tangentially oriented cases, there is only a mirror symmetry with respect to the x-z plane, which means we only have $\frac{dP}{d\Omega}(\theta, \phi) = \frac{dP}{d\Omega}(\theta, 2\pi - \phi)$. Here we only present the radiated power at scattering angles $\phi = 0$ and $0 \leq \theta \leq \pi$ for both cases. The results for $ka = 8$ are shown in Fig. 12, and those for $ka = 20$ are shown in Fig. 13, where "R" stands for the radially oriented cases, and "T" for the tangentially oriented cases. The results of radiated power per solid angle shown in the figures have units of $(c^2 Z_0/32\pi^2)\, k^4 |\mathbf{p}|^2$.

As evident from Fig. 12, the DDA can give quite accurate approximations to the radiation pattern at all scattering angles as long as $mkd < 0.5$ and the source dipole is embedded inside the host particle, i.e., $z/a < 1$. The relative errors at most scattering angles are less than $\pm 5\%$. Relatively larger errors at some scattering angles are observed because the radiated power is low (4 orders lower than the power at other angles), so that the relative errors become significant. While if the source dipole is on the surface of the host particle, $z/a = 1$, the DDA results deviate from the analytical results. However, the radiation pattern is quite similar to that of the analytical solution. The DDA results are over/underestimated almost at the same ratio ($\sim 40\%$ in the radial case and $\sim -18\%$ in the tangential case) at most scattering angles.

If $mkd > 0.5$, as shown in Fig. 13, the DDA gives less accurate results for the radiated power per solid angle for a source dipole inside the host particle. The relative errors can be as large as $\pm 15\%$ when $z/a = 1/4$ and $1/2$ and $\pm 30\%$ when $z/a = 3/4$ at most scattering angles. However, the DDA still gives quite accurate radiation patterns, even though there are many maxima and minima. For source dipole located on the surface of the host particle, the radiated power was again over/underestimated, although the overall radiation pattern is roughly correct.

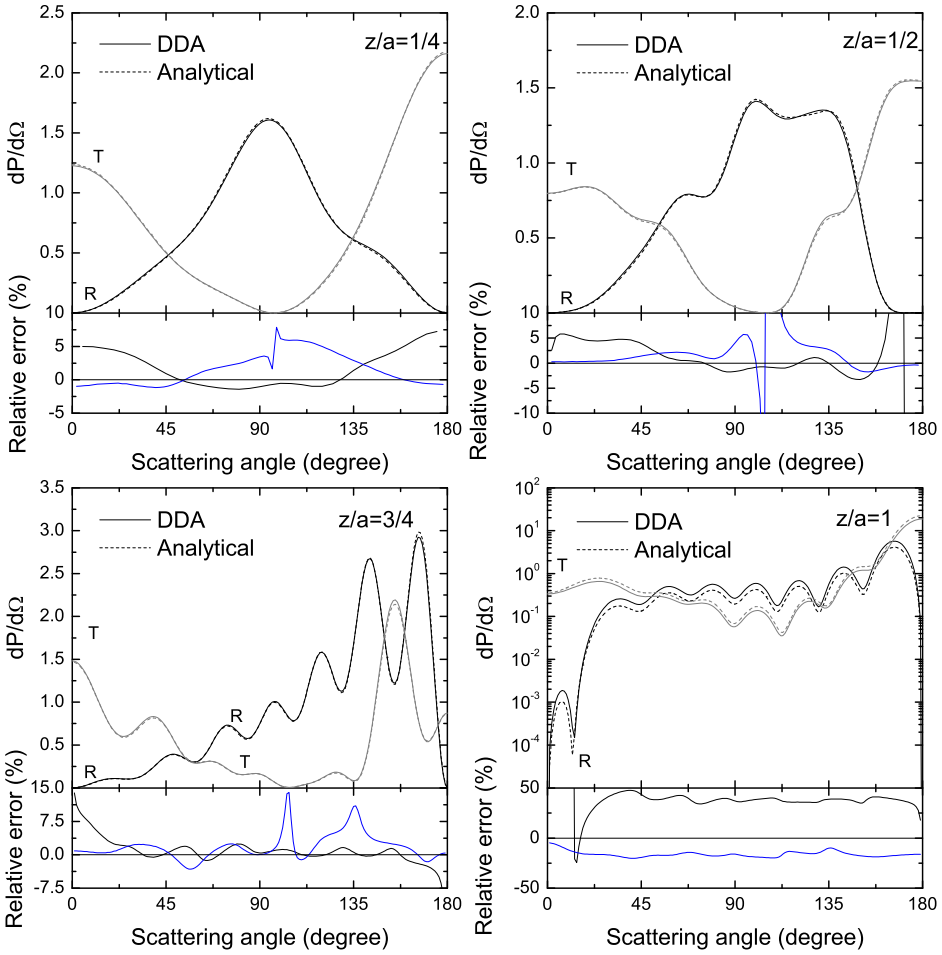

Fig. 12. Radiated power per solid angle versus the scattering angle θ when the source dipole is located at various locations, for the spherical host particle of size parameter $ka = 8$ and refractive index $m = 1.33$, given by the DDA and analytic method.

Furthermore, we consider the radiation pattern in a more general case: a source dipole embedded in a spherical particle with a size parameter of $ka = 8$ and a refractive index of $m = 1.33$. The source dipole is located on the z-axis at $z/a = 1/2$ and oscillates along a direction specified by a unit vector of $\hat{x}+\hat{z}$. In this case, the radiation

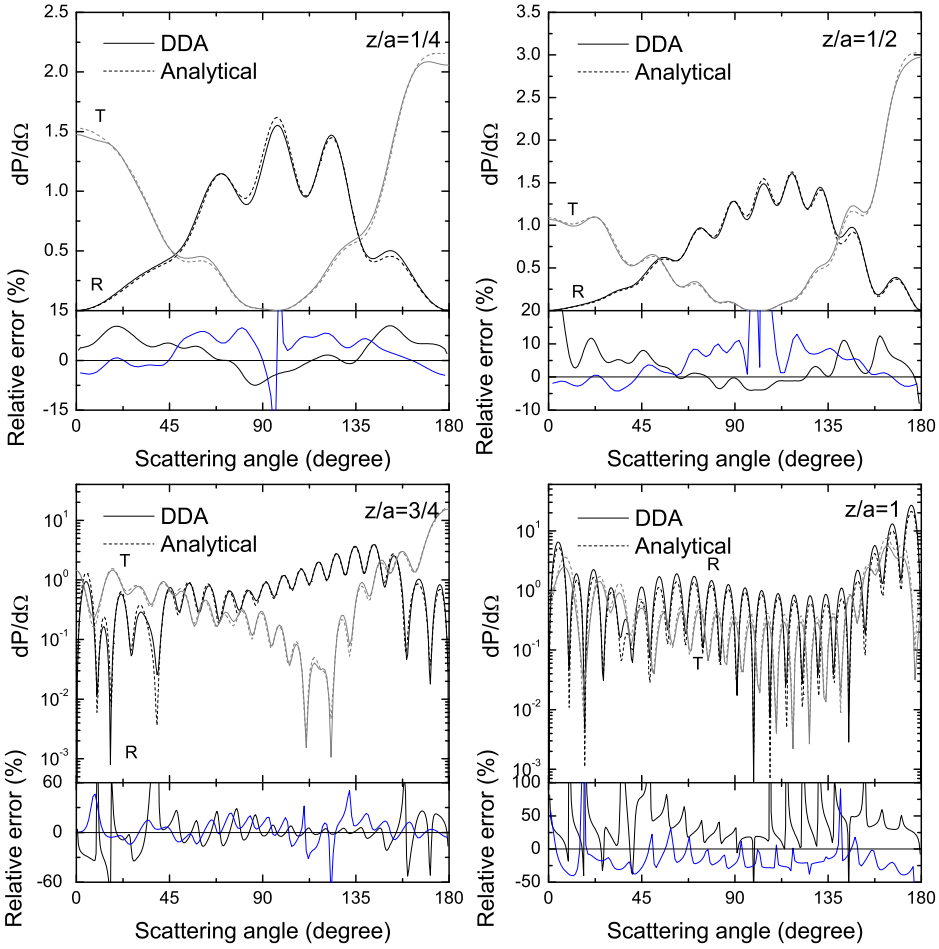

Fig. 13. Same as Fig. 12, but for size parameter $ka = 20$.

pattern is symmetric with respect to the x-z plane so that $\frac{dP}{d\Omega}(\theta, \phi) = \frac{dP}{d\Omega}(\theta, 2\pi - \phi)$. Again, $mkd = 0.3324$ is used for the simulation. Figure 14 shows the results of the radiation patterns computed from both the DDA and analytical methods in the region of $0 \leq \theta \leq \pi$ and $0 \leq \phi \leq \pi$. Shown in Fig. 14 are also the DDA relative errors. Evidently, the two results for the radiated power agree quite well at all scattering angles, and the radiation pattern is accurately predicted by the DDA method. The

relative errors are less than $\pm 2.5\%$ at most scattering angles, except those angles for which the radiated power is low ($\sim 10^{-4}$) then the relative errors are significant.

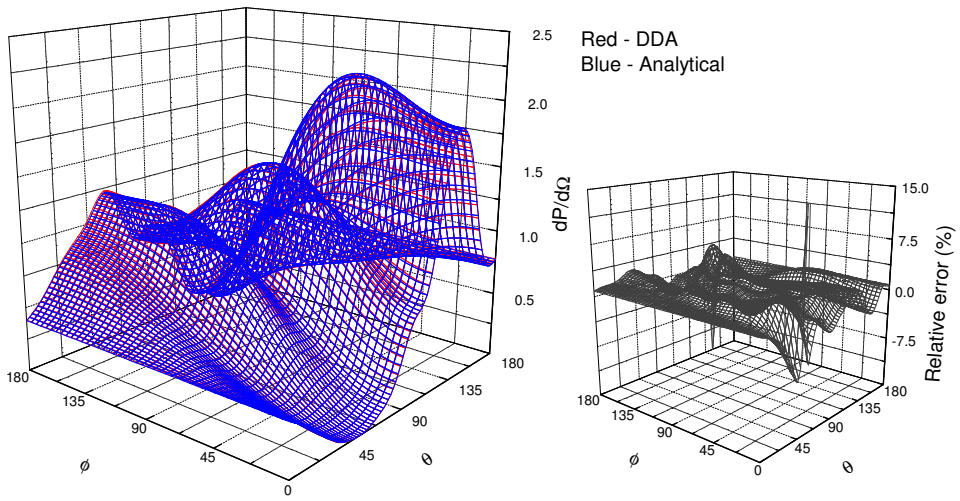

Fig. 14. Radiated power per solid angle, as well as corresponding relative error, versus the scattering angles θ and ϕ, for a source dipole embedded in a spherical host particle of size parameter $ka = 8$ and refractive index $m = 1.33$, located on z-axis at $z/a = 1/2$ and oscillating along $\hat{x} + \hat{z}$.

Moreover, to check the accuracy of the DDA formalism for the internal dipole radiation pertaining to non-spherical particles, we compute the radiate power distribution of a single dipole embedded in a cubic particle and a cylindrical particle with aspect ratio 1. The DDA results are compared with those computed from the FDTD method. In the comparison, the refractive index is $m = 1.33$ and the effective size parameters (the size parameter of a sphere that has the same volume as aspherical particle) of the particles are $ka_{\text{eff}} = 8$. The orientation of the host particle are shown in Fig. 15. The source dipoles are located at the center of the particles, and oscillate along the z direction. In the DDA computation, $mkd = 0.2680$ for the cubic case, and $mkd = 0.2901$ for the cylindrical case. Shown in Fig. 15 are the results for

scattering angles $0 \leq \theta \leq \pi$ and $\phi = 0$. The radiated power computed from the two numerical methods agree very well, although there are some minor discrepancies. The radiation patterns for particles with different shapes are different, which implies that the internal dipole radiation information can be used to detect the morphology of host particles.

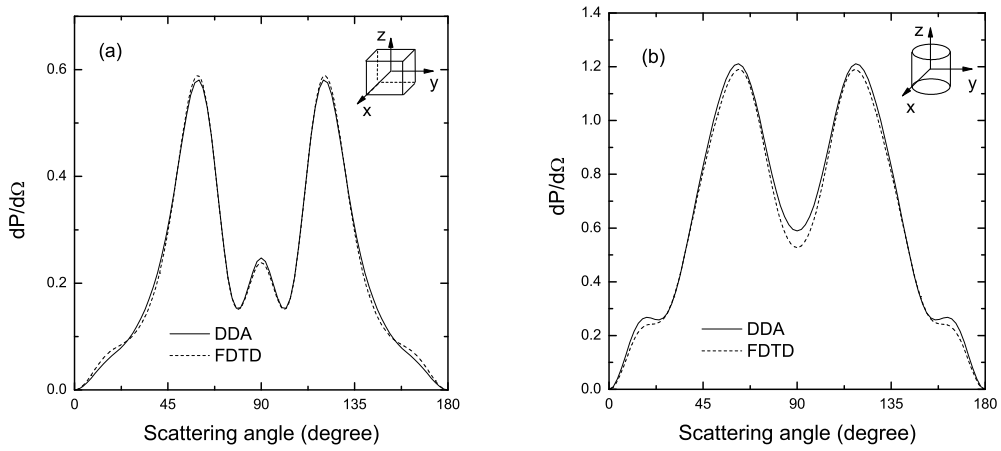

Fig. 15. Radiated power per solid angle versus the scattering angle θ of internal dipole radiation in cubic and cylindric particles with $ka_{\text{eff}} = 8$, refractive index $m = 1.33$, and a source dipole located at the center and oscillating along the z direction.

4. Simulation of Inelastic Scattering

Having proved the accuracy of the DDA formalism in simulating radiation from a single internal dipole, we can confidently use it to compute inelastic scattering. Similar to Chew's model, there will be two steps in simulating the inelastic scattering light field using the DDA formalism. Firstly, an internal exciting field at the incident frequency should be established using either analytical or numerical approach. This exciting field, along with a prescribed number density distribution of the active

molecules, determines the distribution of the excited molecules, or, in the language of the DDA calculation, the oscillating source dipoles.

From the numerical calculation perspective, the coherent scattering is easier to simulate, as one only needs to sum up the radiated electric field associated with each individual source dipole. Therefore, one can simply compute the sum of the radiated electric field in one run with a collection of source dipoles, each of which with proper dipole moment, orientation, and phase information. The total electric field computed from the DDA formalism will automatically be the superposition of electric fields due to all source dipoles as the electric field is additive. Simulation of the incoherent scattering, on the other hand, requires more computational efforts, as in this case one has to run a DDA simulation for each individual source dipole separately, calculate the radiated power, i.e., square of the magnitude of the radiated electric field, due to the specific source dipole being calculated, and then sum up the radiated power.

We first did several simulations for an incoherent scattering from a collection of homogeneous distributed active molecules embedded in a spherical particle. Unlike the spherical distribution of active molecules used in previous studies, we used a cubic distribution as the DDA formalism uses a cubic array to represent the dielectric particle. A total number of 2103 induced dipoles were used in each simulation. To compare with results in previous studies, the inelastic scattering was assumed to occur at $\lambda' = 1.196\lambda$, where λ is the wavelength of the incident radiation. The incident light was assumed to be linearly polarized and oscillating in the scattering plane, $\phi = 0$. A collection of homogeneously distributed source dipoles were used to represent the homogeneously distributed active molecules. The dipole moment of each source dipole was assumed to be induced in the direction parallel to the local exciting field. The parallel component of the inelastic-scattered radiance, i.e., the component lies in the scattering plane, I_r, is shown in Fig. 16.

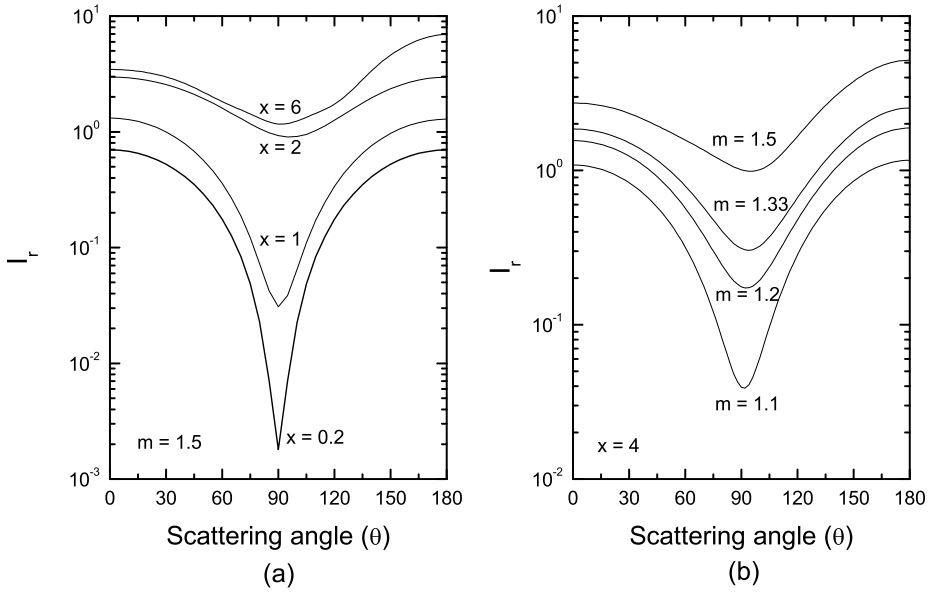

Fig. 16. The parallel component of the incoherent radiance, I_r, from homogeneously distributed active molecules embedded in a spherical particle with a variety of refractive indexes and size parameters. (a) $m = 1.5$ and $x = 0.2$, 1, 2 and 6; (b) $m = 1.1$, 1.2, 1.33 and 1.5, and $x = 4$.

Figure 16(a) shows the resultant I_r associated with a host particle with a fixed refractive index $m = 1.5$ and a varying size parameter $x = 0.2$, 1, 2 and 6. Shown in Fig. 16(b) are I_r associated with a host particle with a varying refractive index $m = 1.1$, 1.2, 1.33 and 1.5, and a fixed size parameter $x = 4$. Results for similar cases have been reported by Kerker and Druger [39] and by Veselovskii *et al.* [41]. Comparing Fig. 16(a) with Fig. 5 in Ref. [39], and Fig. 2(a) in Ref. [41], and comparing Fig. 16(b) with Fig. 10 in Ref. [39], one can notice that the results given by the DDA formalism agree with previous results.

Next we use the DDA formalism to simulate inelastic-scattered radiation from a modeled spore-like particle. We consider a layered prolate spheroidal particle with

a core and a coat, as shown in Fig. 17(a). The refractive index varying radially, as Fig. 17(b) shows. This layered spheroid model provides an ideal representation of the structural feature of spore particles of *Bacillus megaterium* and *Bacillus cereus* observed via electron microscopes [47].

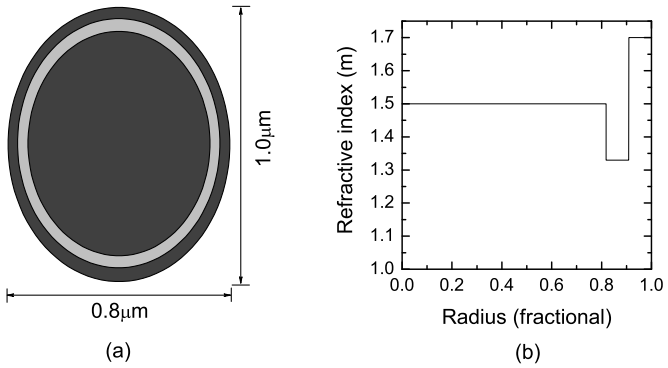

Fig. 17. (a) Geometry and size of the spore particle model in this study; and (b) radial variation of the refractive index.

We first simulate the exciting electric field distribution when an unpolarized plane wave with wavelength $\lambda = 0.5$ μm is incident on the spore-like particle parallel to its axis of symmetry from the left. The size parameter of the particle is $x = 5.41$. A unit amplitude is assumed for the incident electric field. Figure 18(a) shows the resultant distribution of the square of the magnitude of the exciting electric field, $|E_0|^2$, in the vicinity of the spore particle, which is highly inhomogeneous. In this case, one can notice a small region with significantly higher $|E_0|^2$ in the coat layer at the far end of the spheroidal particle. The distribution of $|E_0|^2$ when the plane wave is incident perpendicular to the axis of symmetry from the left is shown in Fig. 18(b). Again, there is a small region with high $|E_0|^2$ in the coat layer at the far end. The maximum value, however, is smaller than that in case (a).

All previous studies on angular dependence of inelastic scattering have assumed

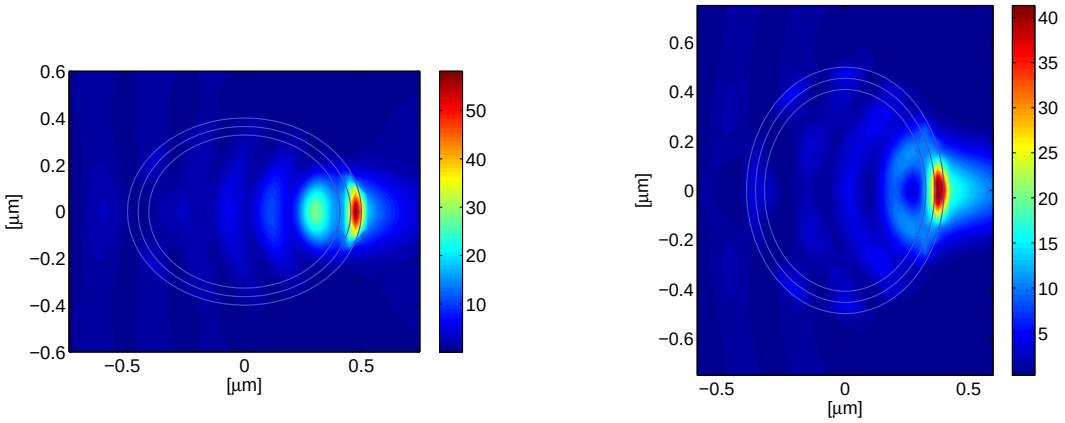

(a) (b)

Fig. 18. Square of the magnitude of the exciting electric field $|E_0|^2$ in the vicinity of the spore-like particle when an unpolarized plane wave is incident (a) parallel to or (b) perpendicular to the symmetry of axis of the spheroidal particle from the left. Shown here are the situations in the $\phi = 0$ plane.

a homogeneous distribution of active molecules throughout the whole host particle. In many cases, however, active molecules in the host particle will be inhomogeneously distributed. In this study, we intend to investigate the effects of the distribution of active molecules on the inelastic-scattering patterns. We assumed three distributions: homogeneously distributed (i) everywhere throughout the full particle; (ii) only within the core; and (iii) only within the coat. In our simulations, over $1,500$ source dipoles were used to represent the distributions of the active molecules, and about $20,000$ induced dipoles were used to represent the scattering particle. An unpolarized incident plane wave with a wavelength of $\lambda_0 = 0.5$ μm, and a inelastic scattering wavelength of $\lambda = 1.196\lambda_0$ were assumed. Shown in Figs. 19 and 20 are the inelastic-scattering radiance associated with two orientations of the modeled spore particle. In these figures, we show the component of the radiance parallel to the scattering plane I_{para}, the component of the radiance perpendicular to the scattering plane I_{perp}, as well as

the total radiance $I = I_{\text{para}} + I_{\text{perp}}$, respectively.

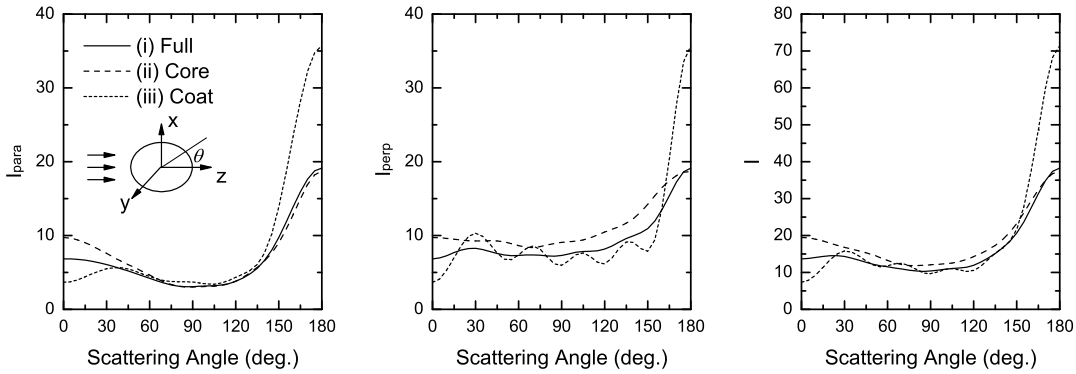

Fig. 19. Inelastic-scattering radiance as a function of the scattering angle θ associated with the modeled spore particle and the three distributions of the active molecules. The incident light is propagating along the axis of symmetry of the spheroid (end-on incidence).

Figure 19 shows the results when the incident field propagates along the axis of symmetry of the spheroid. In this case, the system is azimuthally symmetric. Therefore, the scattering patterns in all scattering planes are identical. It can be noticed from Fig. 19 that all three quantities, I_{para}, I_{perp} and I, give useful information on how the active molecules are distributed within the host particle. Case (iii), in which the active molecules are homogeneously distributed only within the coat, can be easily discriminated from the other cases, as the corresponding inelastic-scattering patterns feature a larger peak in the backscatter direction. Specifically, the I_{perp} pattern associated with case (iii) is oscillating and differs substantially from patterns associated with the other cases. The scattering patterns in the other two cases look similar, but one can still discriminate them from each other by noticing that the I_{para} pattern associated with case (i) becomes flat when approaching the forward scatter

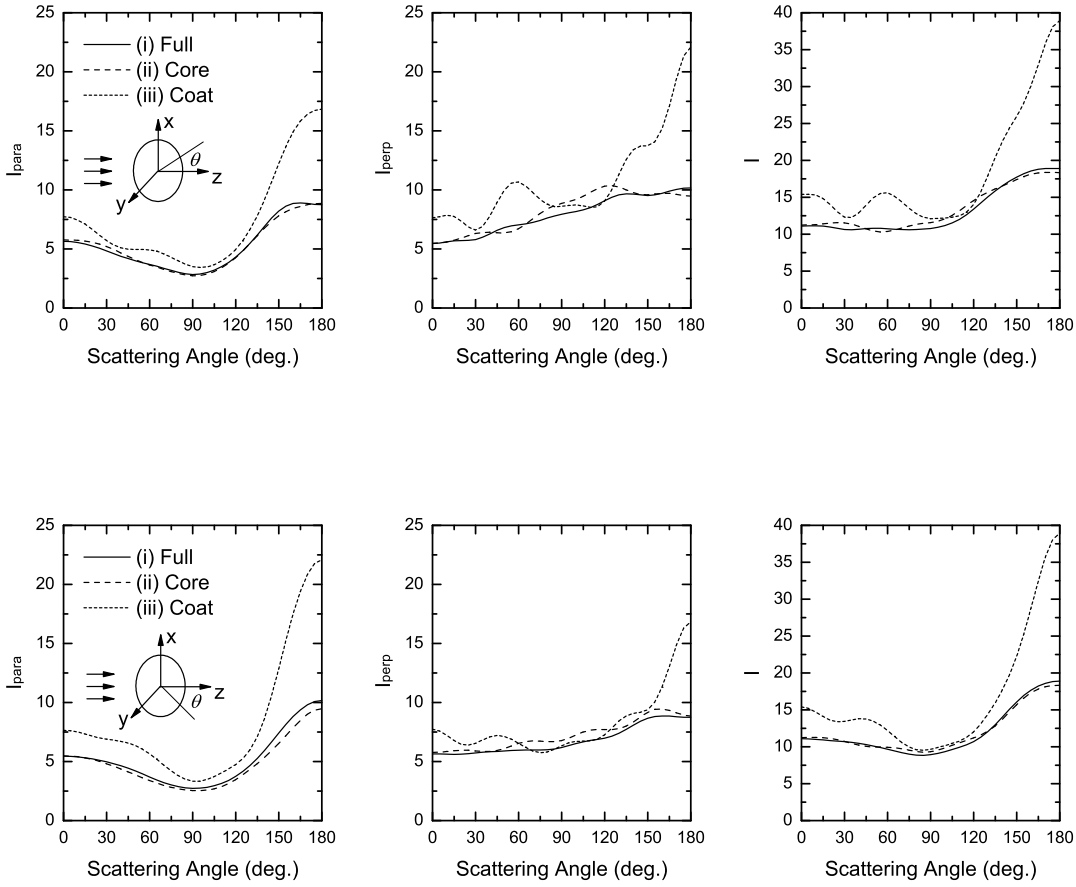

Fig. 20. Same as Fig. 19, but for a spore particle with its axis of symmetry along the x-direction (broadside incidence). The upper and lower panels show the inelastic-scattering pattern in the scattering planes of $\phi = 0°$ and $\phi = 90°$, respectively.

direction, while that associated with case (ii) keeps rising.

Figure 20 shows the same inelastic-scattering patterns, but for a spore particle with its axis of symmetry along the x-direction. In this case, the system is no longer azimuthally symmetric. Therefore, we show the resultant scattering patterns in scattering planes $\phi = 0°$ and $\phi = 90°$, respectively. In this case, the inelastic-scattering

patterns associated with case (iii) still have a larger peak at the backscatter direction. Therefore, the distribution (iii) can again be easily discriminated from the other two. The I_{para} and I patterns associated with the other two cases look very similar. To discriminate cases (i) and (ii), one can investigate the I_{perp} patterns, which differ appreciably in the two cases.

The simulated results from DDA computations suggest that the inelastic-scattering pattern contains useful information on the distribution of the active molecules inside the host particle. Therefore, it can be used as a powerful tool to investigate the distribution of the active molecules in host spore particles.

C. Application of the DDA Method to Invisibility Cloaks*

Invisibility cloak using metamaterial has been a popular research topic in the recent years. In this section, we will present an extension of the conventional DDA formalism that can be conveniently used to study invisibility cloaks for irregular particles.

1. Invisibility Cloak Using Metamaterials

Controlling electromagnetic fields using material properties determined by the coordinate transformation approach [54, 55, 56, 57, 58, 59, 60] has recently drawn extensive attention in the research community. The coordinate transformation approach pioneered by Pendry and colleagues has been reported in a general coordinate system [54, 55, 56] and in Cartesian coordinates [57]. A coordinate transformation method in the form of optical conformal mapping [58, 59] in arbitrary coordinates has also

*Part of the data reported in this section is reprinted with permission from "Zero-backscatter cloak for aspherical particles using a generalized DDA formalism", Y. You, G. W. Kattawar, P.-W. Zhai, and P. Yang, Opt. Express **16,** 2068-2079 (2008), and "Invisibility cloaks for irregular particles using coordinate transformations", Y. You, G. W. Kattawar, P.-W. Zhai, and P. Yang, Opt. Express **16,** 6134-6145 (2008). Copyright 2008 by Optical Society of America.

been reported. In Cartesian coordinates, for example, a point in space is described by its Cartesian components x^i, with $i = 1, 2, 3$. Consider a coordinate transformation $x^i \rightarrow x^{i'} = x^{i'}(x^i)$, a rank 2 contravariant tensor density T^{ij} of weight +1 transforms as [61]

$$T^{i'j'} = \left|\det\left(\Lambda_i^{i'}\right)\right|^{-1} \Lambda_i^{i'} \Lambda_j^{j'} T^{ij}, \tag{2.17}$$

where

$$\Lambda_i^{i'} = \frac{\partial x^{i'}}{\partial x^i} \tag{2.18}$$

is the Jacobian transformation matrix. The permittivity ϵ^{ij} and the permeability μ^{ij} are both rank 2 contravariant tensor densities with weight +1 that describe material properties. Therefore, they transform as

$$\epsilon^{i'j'} = \left|\det\left(\Lambda_i^{i'}\right)\right|^{-1} \Lambda_i^{i'} \Lambda_j^{j'} \epsilon^{ij}, \tag{2.19a}$$

$$\mu^{i'j'} = \left|\det\left(\Lambda_i^{i'}\right)\right|^{-1} \Lambda_i^{i'} \Lambda_j^{j'} \mu^{ij}. \tag{2.19b}$$

Pendry *et al.* [55] and Schurig *et al.* [57] suggested that the left hand sides of Eqs.(2.19a) and (2.19b) be interpreted as either the properties of the same material in the transformed coordinate system (the *topological interpretation*), or the properties of an another material in a flat Cartesian coordinate system (the *material interpretation*).

It has been demonstrated that the transformation properties of Maxwell equations under certain coordinate transformations can yield material properties that have interesting functionality, such as invisibility cloaks [55, 56, 57], perfect lens [56], and magnification [56, 60], however, this study will focus on invisibility cloaks.

As has been discussed in Ref. [57], the material properties of an invisibility cloak can be determined as illustrated in Fig. 21. Consider a closed domain that is to be transformed (region (I) in Fig. 21(a)). The internal and external regions of this

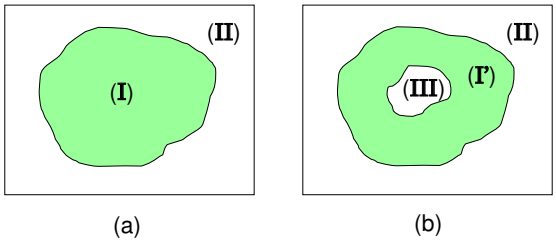

Fig. 21. Illustration of the coordinate transformation used to determine the material properties of a cloak.

domain are assumed to be vacuum. Next, consider a coordinate transformation that maps this region into a region (region (I′) in Fig. 21(b)) that has the same outer boundary but contains a hole (region (III)) bounded by an inner boundary. Then, determine the material properties $\epsilon^{i'j'}$ and $\mu^{i'j'}$ in region (I′), which no longer represent a vacuum, using Eqs.(2.19a) and (2.19b). Meanwhile, the external region (region (II)) remains undistorted, therefore the material properties $\epsilon^{i'j'}$ and $\mu^{i'j'}$ in this region still represent a vacuum. In this manner, we have defined a cloaking region. Subject to radiation from outside sources, this object compresses the radiation field in region (I) into region (I′), the *cloaking region*, and leaves region (III), the *cloaked region*, radiation-free. This implies that there is no interaction between anything in the cloaked region and sources in the outside domain. Outside of the cloaking region, the radiation fields remain unchanged, as if neither the cloaking material nor any cloaked object exists. In principle, regions (I), (I′), and (III) can be of arbitrary shapes, although the transformation matrix Eq.(2.18) associated with irregular shapes may be quite complicated.

The first invisibility cloak ever studied is a spherical one. Following the coordinate transformation approach, and considering the coordinate transformation

$$r' = \frac{b-a}{b} r + a, \tag{2.20a}$$

$$\theta' = \theta, \tag{2.20b}$$

$$\phi' = \phi, \tag{2.20c}$$

in the spherical coordinates (r, θ, ϕ) [55], or, equivalently

$$x^{i'} = \frac{b-a}{b} x^i \delta_i^{i'} + a \frac{x^i}{r} \delta_i^{i'}, \tag{2.21}$$

in Cartesian coordinates [57], it has be derived that the electric permittivity and magnetic permeability tensors of a spherical invisibility cloak are given by

$$\bar{\bar{\epsilon}} = \epsilon_r(r)\hat{r}\hat{r} + \epsilon_t[\hat{\theta}\hat{\theta} + \hat{\phi}\hat{\phi}], \tag{2.22a}$$

$$\bar{\bar{\mu}} = \mu_r(r)\hat{r}\hat{r} + \mu_t[\hat{\theta}\hat{\theta} + \hat{\phi}\hat{\phi}], \tag{2.22b}$$

where

$$\epsilon_t = \mu_t = \mu_0 \frac{b}{b-a} \tag{2.22c}$$

are the tangential components, and

$$\epsilon_r(r) = \mu_r(r) = \mu_t \frac{(r-a)^2}{r^2} \tag{2.22d}$$

are the radial components of the permittivity and permeability, respectively, with a and b the inner and outer radii of the spherical cloak, respectively.

The material properties for an infinite cylindrical invisibility cloak have also been reported [56, 62, 63]. The resultant ϵ and μ tensors are given by

$$\epsilon_r = \mu_r = \frac{r-a}{r}, \tag{2.23a}$$

$$\epsilon_\theta = \mu_\theta = \frac{r}{r-a}, \tag{2.23b}$$

$$\epsilon_\phi = \mu_\phi = \left(\frac{b}{b-a}\right)^2 \frac{r-a}{r}, \tag{2.23c}$$

where a and b are the inner and outer radii of a cylinder, respectively. The invisibility

predicted by the coordinate transformation approach has been verified by a variety of analytical and numerical calculations for various geometries. Ray-tracing simulations [55, 57] in the geometric optics limit have been reported for a cloaked sphere with consistent results. Rigorous solutions to Maxwell's equations have been reported in the spherical case [64] and in the 2-D cylindrical case [65], confirming the cloaking effects in both cases. Numerical simulations using the full-wave finite-element method have been performed to study the effects of the cloaking material on the propagation of the incident waves associated with 2-D invisibility cloaks of various shapes, such as cylinders [62], squares [66], elliptical cylinders [67], and eccentric elliptical cylinders [68]. In all of these numerical studies, simulated local field distribution outside of the cloak is found to be the same as that of the incident radiation.

Materials with inhomogeneous, anisotropic, and continuously varying electric permittivity and magnetic permeability specifications as given by Eqs.(2.19a) and (2.19b) are not available in nature. They are also hard, if not impossible, to fabricate using conventional materials. Fortunately, recent development of metamaterial technology [69] enables manipulations of material properties on small scales and makes it possible to practically implement the required material specification in a discretized fashion. 2-D cylindrical cloaking has been realized using artificially structured metamaterials at microwave frequencies [63] and at optical frequencies with reduced cloak material properties [70]. In the study reported in [63], ten layers of Cu films, each of which with a proper ϵ and μ, were placed in a concentric arrangement. In the study reported in [70], metal wires with varying material properties were aligned radially. In both experiments, a reduced material property specification was used. Considerable cloaking effects were observed in both studies, although the cloak material properties are not perfect.

2. Generalization of the DDA Method to Metamaterials

Due to its capability to simulate light scattering from particles with arbitrary morphology, the DDA method can be another powerful tool to study the invisibility cloak numerically. As aforementioned, however, application of the DDA formalism has been limited to light scattering associated with dielectric particles, i.e., particles with permeability $\mu = 1$ and vanishing magnetic susceptibility $\chi_m = \mu - 1 = 0$, since all natural scatterers of interest fall into this category. In this case, the null magnetization $\mathbf{M} = \chi_m \mathbf{H} = 0$ allows us to represent the scattering particle solely by a collection of electric dipoles. For materials with nonzero magnetic susceptibilities such as metamaterials, the magnetization $\mathbf{M}$ is non-vanishing. Therefore, as has been reported by Lakhtakia [71], both electric and magnetic dipoles should be included such that both electric and magnetic responses of the scattering particle to the incident electromagnetic radiation are properly accounted for.

Following Lakhtakia's steps, we still use a cubic array to represent the particle, but locate both an electric and a magnetic dipole at each lattice site j in the cubic lattice with $j = 1, \cdots, N$ running over all occupied lattice sites. As usual, each electric dipole is characterized by the polarizability tensor $\bar{\bar{\alpha}}_j$ such that Eq.(2.1) is satisfied with $\mathbf{E}_{\text{ext},j}$ being the electric field at position j due to electric and magnetic dipoles at all other lattice sites and the incident radiation. Similarly, each magnetic dipole is characterized by a magnetic susceptibility tensor $\bar{\bar{\chi}}_{m,j}$ such that

$$\mathbf{M}_j = \bar{\bar{\chi}}_{m,j} \mathbf{H}_{\text{ext},j}, \tag{2.24}$$

where $\mathbf{M}_j$ is the magnetic dipole moment and $\mathbf{H}_{\text{ext},j}$ is the magnetic field at position j due to the radiating electric and magnetic dipoles at all other lattice sites and the incident radiation.

For paramagnetic materials, there is an equation like the Clausius-Mossotti equation that relates the microscopic magnetic susceptibility of each magnetic dipole $\bar{\bar{\chi}}_{m,j}$ and the local macroscopic magnetic permeability $\bar{\bar{\mu}}_j$ in the zero frequency limit $kd = 0$. Similar to Eq.(2.2), the magnetic equation can be written as [6]

$$\bar{\bar{\chi}}^0_{m,j} = \frac{3}{4\pi n}\frac{\bar{\bar{\mu}}_j - 1}{\bar{\bar{\mu}}_j + 2}. \tag{2.25}$$

In the long-wavelength limit, $kd \ll 1$, the lattice dispersion relation (LDR) [27] also holds for the magnetic susceptibility, giving a magnetic susceptibility at finite frequency $\bar{\bar{\chi}}_m(kd)$. The resultant relation is similar to Eq.(2.4a), with $\bar{\bar{\alpha}}$ replaced by $\bar{\bar{\chi}}_m$ and $\bar{\bar{\epsilon}}$ replaced by $\bar{\bar{\mu}}$

$$\bar{\bar{\chi}}_m = \frac{\bar{\bar{\chi}}^0_m}{1 + (\bar{\bar{\chi}}^0_m/d^3)(b_1 + \bar{\bar{\mu}}b_2 + \bar{\bar{\mu}}b_3 S)(kd)^2}, \tag{2.26}$$

where the parameters b_1, b_2, b_3 and S have been given by Eqs.(2.4b) and (2.4c).

Knowing the polarizability $\bar{\bar{\alpha}}_j$ and the magnetic susceptibility $\bar{\bar{\chi}}_{m,j}$ at all lattice sites j, one can readily write down the self-consistent set of equations for electric and magnetic dipole moments $\mathbf{P}_j$ and $\mathbf{M}_j$ $(j = 1, \cdots, N)$ as

$$\begin{bmatrix} \bar{\bar{\alpha}}_j^{-1}\mathbf{P}_j \\ \bar{\bar{\chi}}_{m,j}^{-1}\mathbf{M}_j \end{bmatrix} = \begin{bmatrix} \mathbf{E}_{\mathrm{inc},j} \\ \mathbf{H}_{\mathrm{inc},j} \end{bmatrix} - \sum_{k\neq j} \begin{bmatrix} \mathbf{A}^{(ee)}_{jk} & \mathbf{A}^{(eh)}_{jk} \\ \mathbf{A}^{(he)}_{jk} & \mathbf{A}^{(hh)}_{jk} \end{bmatrix} \cdot \begin{bmatrix} \mathbf{P}_k \\ \mathbf{M}_k \end{bmatrix}, \tag{2.27}$$

where in the first term

$$\begin{aligned} \mathbf{E}_{\mathrm{inc},j} &= \mathbf{E}_0 \exp\left(i\mathbf{k}\cdot\mathbf{r}_j - i\omega t\right) \\ \mathbf{H}_{\mathrm{inc},j} &= \mathbf{H}_0 \exp\left(i\mathbf{k}\cdot\mathbf{r}_j - i\omega t\right) \end{aligned} \tag{2.28}$$

are the electric and magnetic fields at position j due to the incident plane wave electromagnetic radiation, with $\mathbf{E}_0 \times \mathbf{H}_0 = \mathbf{k}$, the wave vector of the incident radiation. For simplicity, we will always assume an incident plane wave throughout this section.

In the second term, $-\mathbf{A}_{jk}^{(ee)}\mathbf{P}_k$ and $-\mathbf{A}_{jk}^{(eh)}\mathbf{M}_k$ are the contributions to the electric field at position j due to the electric and magnetic dipoles at position k, which have been conveniently given by Jackson in his classical textbook [6] (pp. 411 and pp. 413)

$$\begin{aligned}
\mathbf{A}_{jk}^{(ee)}\mathbf{P}_k &= \frac{\exp(ikr_{jk})}{r_{jk}^3}\Bigg\{k^2\mathbf{r}_{jk}\times(\mathbf{r}_{jk}\times\mathbf{P}_k)+ \\
&\qquad \frac{(1-ikr_{jk})}{r_{jk}^2}\left[r_{jk}^2\mathbf{P}_k-3\mathbf{r}_{jk}\left(\mathbf{r}_{jk}\cdot\mathbf{P}_k\right)\right]\Bigg\}, \qquad (2.29a)\\
\mathbf{A}_{jk}^{(eh)}\mathbf{M}_k &= \frac{\exp(ikr_{jk})}{r_{jk}^3}\left(\mathbf{r}_{jk}\times\mathbf{M}_k\right)\left(r_{jk}-\frac{1}{ik}\right), \qquad (2.29b)
\end{aligned}$$

and $-\mathbf{A}_{jk}^{(he)}\mathbf{P}_k$ and $-\mathbf{A}_{jk}^{(hh)}\mathbf{M}_k$ are the contributions to the magnetic field at position j due to the electric and magnetic dipoles at position k, given by [6]

$$\begin{aligned}
\mathbf{A}_{jk}^{(he)}\mathbf{P}_k &= \frac{\exp(ikr_{jk})}{r_{jk}^3}\left(\mathbf{r}_{jk}\times\mathbf{P}_k\right)\left(\frac{1}{ik}-r_{jk}\right), \qquad (2.30a)\\
\mathbf{A}_{jk}^{(hh)}\mathbf{M}_k &= \frac{\exp(ikr_{jk})}{r_{jk}^3}\Bigg\{k^2\mathbf{r}_{jk}\times(\mathbf{r}_{jk}\times\mathbf{M}_k)+ \\
&\qquad \frac{(1-ikr_{jk})}{r_{jk}^2}\left[r_{jk}^2\mathbf{M}_k-3\mathbf{r}_{jk}\left(\mathbf{r}_{jk}\cdot\mathbf{M}_k\right)\right]\Bigg\}, \qquad (2.30b)
\end{aligned}$$

where $\mathbf{r}_{jk}=\mathbf{r}_j-\mathbf{r}_k$ and $r_{jk}=|\mathbf{r}_{jk}|$. It is evident here that the electric dipole moments and magnetic dipole moments are coupled with each other.

Letting $\mathbf{A}_{jk}$ be the off-diagonal elements of $\mathbf{A}$-matrices, and defining the diagonal elements of these $\mathbf{A}$-matrices as follows

$$\begin{aligned}
&\mathbf{A}_{jj}^{(ee)}=\bar{\bar{\alpha}}_j^{-1}, \quad \mathbf{A}_{jj}^{(eh)}=0,\\
&\mathbf{A}_{jj}^{(he)}=0, \qquad \mathbf{A}_{jj}^{(hh)}=\bar{\bar{\chi}}_{m,j}^{-1},
\end{aligned} \qquad (2.31)$$

one can reformulate Eq.(2.27) into a compact form as a set of $2N$ inhomogeneous

linear complex vector equations

$$\sum_{k=1}^{N} \begin{bmatrix} \mathbf{A}_{jk}^{(ee)} & \mathbf{A}_{jk}^{(eh)} \\ \mathbf{A}_{jk}^{(he)} & \mathbf{A}_{jk}^{(hh)} \end{bmatrix} \cdot \begin{bmatrix} \mathbf{P}_k \\ \mathbf{M}_k \end{bmatrix} = \begin{bmatrix} \mathbf{E}_{\mathrm{inc},j} \\ \mathbf{H}_{\mathrm{inc},j} \end{bmatrix}. \tag{2.32}$$

Here each element of the $\mathbf{A}$-matrices, $\mathbf{A}_{jk}$, is a 3×3 matrix, where $\mathbf{A}_{jk}^{(ee)}$ and $\mathbf{A}_{jk}^{(hh)}$ are symmetric, while $\mathbf{A}_{jk}^{(eh)}$ and $\mathbf{A}_{jk}^{(he)}$ are anti-symmetric with respect to lattice site indices i and j. We can still use the FFT and CCG methods used in the conventional DDA formalism to solve for $\mathbf{P}_j$'s and $\mathbf{M}_j$'s in Eq.(2.32). However, the CCG algorithm will need more iterations to converge in this case, since a $6N \times 6N$ matrix is involved instead of a $3N \times 3N$ matrix.

Being generalized, the DDA formalism can be readily applied to calculations of interaction between electromagnetic radiation and invisibility cloak with tensorial permittivity and permeability. To validate our generalized DDA code, we first simulated the electric field in the vicinity of a cloaked sphere with a cloak described by Eq.(2.22a). In the simulations, we chose an outer size parameter $b = 8\lambda/2\pi$, and two inner size parameters $a = 0.3b$ and $0.5b$. The results for the two cases are shown in Fig. 22(a) and Fig. 22(b), respectively. For comparison, we also show the corresponding field distribution associated with an uncloaked homogeneous sphere with $\epsilon = \mu = 1.21$ and $a = 8\lambda/2\pi$ in Fig. 22(c). A unit amplitude was assumed for the incident electric field in all three cases. The plane wave is incident from the left.

A quick comparison between the cloaked and uncloaked results reveals that the DDA calculation simulates the plane-wave fields outside of the cloaked particle and the distorted fields in the cloaking material correctly. The same electric field distribution associated with cloaked spheres can be found in previous studies [62, 64], where Cummer *et al.* [62] presented a field distribution simulated by the finite-element method, and Chen *et al.* showed the analytical results by solving Maxwell's equations.

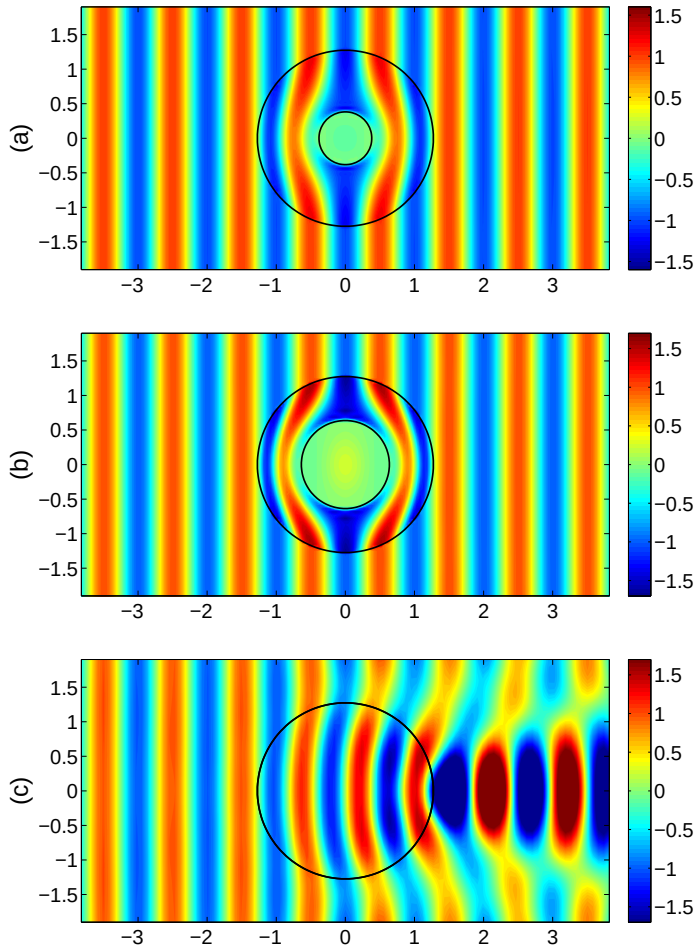

Fig. 22. Electric field distribution in the vicinity of cloaked and uncloaked spheres, with scales in unit of λ. (a) A cloaked sphere with $b = 8\lambda/2\pi$ and $a = 0.3b$; (b) A cloaked sphere with $b = 8\lambda/2\pi$ and $a = 0.5b$. (c) An uncloaked homogeneous sphere with $\epsilon = \mu = 1.21$ and $a = 8\lambda/2\pi$. Black circles indicate the inner and outer boundaries of the cloak, and the incident radiation propagates from the left to the right.

Comparing the DDA simulation with these results, we found that the DDA gives better plane-wave structure outside of the cloak than the finite-element method does.

The DDA simulation of the electric field inside the cloaked region, however, is not exactly zero. In the $a = 0.3b$ case, a maximum leakage of about 13% of the radiating

field, or about 1.7% of the radiative energy, into the cloaked region is observed due to the discretization of material properties in the DDA simulation. In the $a = 0.5b$ case, the maximum leakage is about 24% of the radiating field, or about 6% of the radiative energy. This can be attributed to the fact that the inhomogeneous cloak represented by the discrete array of dipoles is not a perfect cloak. Therefore, the cloaking effects simulated by a DDA computation are not expected to be perfect. What is more, the tangential component of the refractive index determined by Eq.(2.23b) could be very large if the ratio a/b is close to 1. For example, $a = 0.3b$ requires $m_t = \sqrt{\epsilon_t \mu_t} = 1.43$, which is a moderate value; while $a = 0.5b$ requires $m_t = 2$, which is much larger. In the simulations, however, we used the same number of DDA dipoles, which means that the quantity mkd is much larger in the $a = 0.5b$ calculation. Therefore, a larger error in this case is reasonable.

As a numerical method, the DDA is not expected to reproduce the exact zero scattering of a cloaked object. The simulated scattering efficiencies

$$Q_{\text{sca}} = C_{\text{sca}}/(\pi b^2)$$

for the cases shown in Fig. 22 are on or below the order of 10^{-4} (6.13×10^{-5} in case (a) with $a = 0.3b$ and 4.43×10^{-4} in case (b) with $a = 0.5b$), which are sufficiently small to exhibit the nature of invisibility. For comparison, the scattering efficiency of the uncloaked sphere in case (c) is $Q_{\text{sca}} = C_{\text{sca}}/(\pi b^2) = 3.46$. We use the outer radius b in the calculation of Q_{sca} as we are comparing cases with the same b. It can again be noticed that the DDA calculations gave a better simulation of the zero scattering for the cloak with $a = 0.3b$, in which case m_t is smaller.

Finally, to study the capability of the DDA formalism in simulating the far field scattering from a cloaked object, in Fig. 23 we show the simulated differential scattering cross section P_{11} for a cloaked sphere with $b = 5\lambda/2\pi$, $a = 0.2b$, and various

refractive indices in the cloaked region. The P_{11} for uncloaked cores are also shown for comparison. The corresponding scattering efficiencies $Q_{\rm sca} = C_{\rm sca}/(\pi a^2)$ are listed in Table I. These results imply that the DDA formalism has its limitation in simulating the zero scattering of cloaked object, as the simulated P_{11} and $Q_{\rm sca}$ of the cloaked spheres are only 3 orders lower than that of the uncloaked cores. However, it can be noticed that as the refractive index of the cloaked region increases and the scattering of the uncloaked core increases, the simulated scattering of the cloaked spheres stays almost the same. This is a demonstration of the cloaking effects.

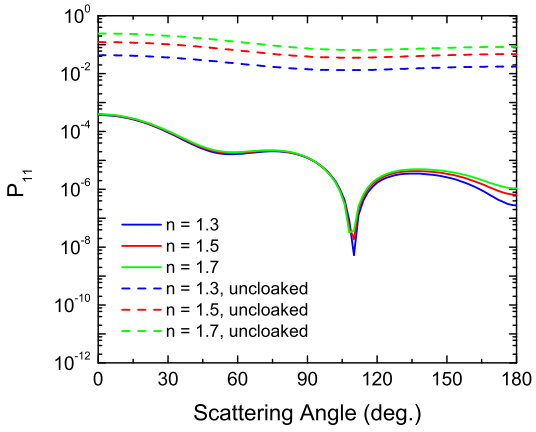

Fig. 23. P_{11} for a cloaked sphere with $b = 5\lambda/2\pi$ and $a = 0.2b$. Refractive indices for the cloaked region $n = 1.3$, 1.5 and 1.7 were simulated. Dash lines are P_{11}'s for corresponding uncloaked spheres.

3. Invisibility Cloak for Irregular Particles

With the generalized DDA formalism ready to use, we now explore invisibility cloaks for particles with irregular shapes. We will determine the ϵ and μ tensors for invisibility cloaks of various morphologies using the coordinate transformation approach, then simulate the interaction between a plane wave incident radiation and such cloaks

Table I. Simulated scattering efficiencies of cloaked spheres and the corresponding uncloaked cores with various refractive indices n.

	$n = 1.3$	$n = 1.5$	$n = 1.7$
Cloaked	1.12×10^{-4}	1.20×10^{-4}	1.27×10^{-4}
Uncloaked	0.77×10^{-1}	2.15×10^{-1}	4.12×10^{-1}

to confirm the cloaking effect.

The coordinate transformation used in the studies of spherical cloaks [55, 57] can be readily generalized to ellipsoids. For an ellipsoid with its semi-axes lying along x-, y-, and z-directions with lengths $\alpha_1 b, \alpha_2 b$, and $\alpha_3 b$, respectively, its outer boundary is described by

$$\left(\frac{x^1}{\alpha_1 b}\right)^2 + \left(\frac{x^2}{\alpha_2 b}\right)^2 + \left(\frac{x^3}{\alpha_3 b}\right)^2 = 1, \tag{2.33}$$

where α_1, α_2, and α_3 are positive numbers characterizing the aspect ratio of the ellipsoid, and do not transform as vectors. Inside this boundary, we start with the coordinate transformation for the spherical cloak Eq.(2.21),

$$x^{i'} = \frac{b-a}{b} x^i \delta_i^{i'} + a\frac{x^i}{r}\delta_i^{i'}, \qquad (a < b) \tag{2.34}$$

where $\delta_i^{i'}$ is the Kronecker tensor, $r = \sqrt{(x^1)^2 + (x^2)^2 + (x^3)^2}$ is the distance between the point and the origin. For an ellipsoid, we can still use this coordinate transformation. But it is necessary to re-define r as a scaled distance

$$r = \left[\sum_{i=1}^{3}\left(\frac{x^i}{\alpha_i}\right)^2\right]^{1/2}. \tag{2.35}$$

This definition guarantees that $r = b$ for any point x^i on the outer boundary. Therefore, $x^{i'} = x^i$, i.e., the outer boundary is not changed by the transformation.

By writing the coordinate transformation in the fashion of Eq.(2.34), we have a

singularity at the origin. Therefore, to investigate how the origin transforms, we need to avoid the singularity and study an infinitesimal ellipsoid bounded by the surface

$$\left(\frac{x^1}{\alpha_1 b}\right)^2 + \left(\frac{x^2}{\alpha_2 b}\right)^2 + \left(\frac{x^3}{\alpha_3 b}\right)^2 = \varepsilon^2, \tag{2.36}$$

where ε is a small positive number. In the limit when ε approaches 0, this surface becomes the origin. A little algebra will show that this surface transforms to a surface

$$\left(\frac{x^1}{\alpha_1 a}\right)^2 + \left(\frac{x^2}{\alpha_2 a}\right)^2 + \left(\frac{x^3}{\alpha_3 a}\right)^2 = 1, \tag{2.37}$$

which is the boundary of a smaller concentric ellipsoid. Therefore, the coordinate transformation determined by Eqs.(2.34) and (2.35) transforms a closed ellipsoid with lengths of the outer semi-axes $\alpha_1 b, \alpha_2 b$, and $\alpha_3 b$ into an ellipsoidal shell with the same lengths of outer semi-axes and lengths of inner semi-axes $\alpha_1 a, \alpha_2 a$, and $\alpha_3 a$. For the external region, we assume the identity transformation. In the following discussions, all equations apply only to the internal region.

In Fig. 24 we show the application of the transformation Eq.(2.34) to a closed ellipsoidal region. The ellipsoid shown in Fig. 24 has a size parameter of $x = 8$, with $\alpha_1 = \alpha_2 = 1$, and $\alpha_3 = 2$, i.e., $b = 2^{1/3} 8\lambda/(2\pi)$. This ellipsoid is practically a prolate spheroid with its axis of symmetry lying along the z direction.

Figure 24(a) shows the ellipsoidal region, along with Cartesian coordinate grid, before the coordinate transformation. As we assume a vacuum everywhere, the coordinate grid lines can also be interpreted as light rays and wave fronts (loci of points having the same phase) if the incident plane wave propagates in the z-direction. A coordinate transformation Eq.(2.34) with $a = 0.5b$ transforms this closed region into the cloaking region shown in Fig. 24(b). The grid lines in the region transform accordingly, and the transformed grid lines, which are geodesics in the transformed coordinates, can be interpreted as light rays and wave fronts in the presence of the

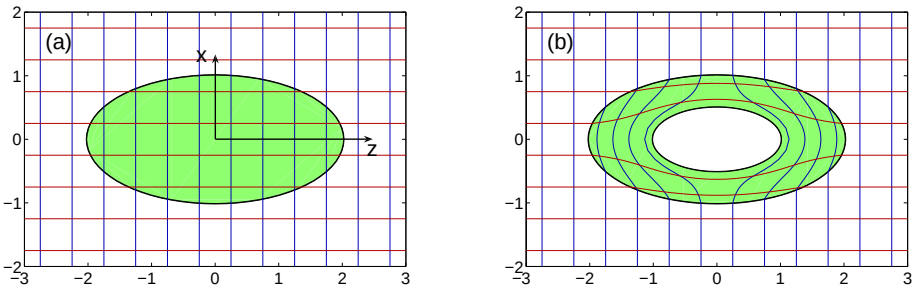

Fig. 24. Application of the coordinate transformation to a spheroidal region subject to a plane-wave radiation propagating in the z-direction. Shown in the figures is the situation in the x-z plane, with the x- and z-axes as depicted in Fig. (a). The scales are in unit of λ. Figure (a) shows the closed region (green region) in Cartesian coordinates, with vacuum both inside and outside. The light rays (dark red lines) and wave fronts (dark blue lines) of the incident radiation are also shown. Figure (b) shows the transformed region according to the transformation Eq.(2.34) with $a = 0.5b$, with the material properties in the cloaking region determined by Eq.(2.19a) and Eq.(2.19b). The light rays and wave fronts transform accordingly.

cloak. As expected, the radiation field never penetrates into the cloaked region. Evidently, the light rays and wave fronts beyond the outer boundary remain the same, as an identity transformation is applied in this region.

A nice feature of the coordinate transformation approach is that it does not depend on the orientation of the incident radiation beam with respect to the cloak. Actually, it works for incident radiance from an arbitrary direction. We just need to do the coordinate transformation in the same Cartesian coordinates spanned by the three semi-axes of the ellipsoid. Figure 25 shows the transformation applied to the same ellipsoid, but subject to an incident plane wave in the x-z plane making an angle of $\theta = 30^\circ$ to the z-axis. Here, a rotated coordinate grid represents the light rays and the wave fronts. Again, it is evident that the light rays and wave fronts inside the

boundary are transformed accordingly such that the cloaked region is never reached.

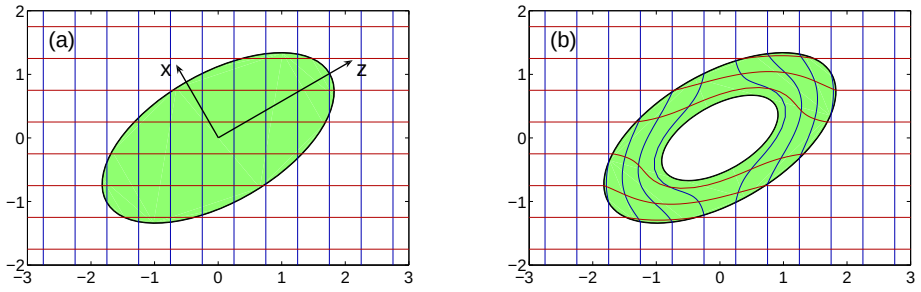

Fig. 25. Same as Fig. 24, but for an incident plane wave in the x-z plane making an angle of $\theta = 30°$ to the z-axis.

To make sure the above prediction by the coordinate transformation approach is true, we turn to DDA simulations, which require material properties of an ellipsoidal cloak. The ϵ^{ij} and μ^{ij} in the cloaking region can be determined by substituting Eqs.(2.34) and (2.35) into Eq.(2.18), which leads to a transformation matrix

$$\Lambda_j^{i'} = \frac{r'}{r}\delta_j^{i'} - \frac{a x^i x^k \delta_i^{i'} \delta_{kj}}{{\alpha_j}^2 r^3} \tag{2.38}$$

in Cartesian coordinate, where the Einstein summation convention has been assumed for indices i and k. For the vacuum, $\epsilon^{ij} = \mu^{ij} = \delta^{ij}$. Therefore, a combination of Eqs.(2.17) and (2.38) gives the material properties in the cloaking region as follows:

$$\epsilon^{ij} = \mu^{ij} = \frac{b}{b-a}\left[\delta^{ij} - x^i x^j \left(\frac{a}{r^3}\left({\alpha_i}^{-2} + {\alpha_j}^{-2}\right) - \frac{a^2}{\tilde{r}^2 r^4}\sum_{k=1}^{3}\frac{\left(\tilde{x}^k\right)^2}{{\alpha_k}^4}\right)\right]. \tag{2.39}$$

As we take the material interpretation, we have dropped all primes and relabeled the variables as follows: $x^i \to \tilde{x}^i$, $r \to \tilde{r}$, $x^{i'} \to x^i$, and $r' \to r$, with r given by Eq.(2.35), $\tilde{r}$ and $\tilde{x}^i$ given by

$$\tilde{x}^i = \frac{x^i}{\frac{b-a}{b} + \frac{a}{r}} \quad \text{and} \quad \tilde{r} = \frac{r-a}{b-a}\cdot b. \tag{2.40}$$

Therefore, we have obtained the permittivity and permeability tensors of an ellipsoidal cloak. In the special case of spheres, $\alpha_i = 1$, Eq.(2.39) reduces to the simple results described by Eqs.(2.22a) and (2.22b).

Next we turn to a cuboidal invisibility cloak. Rahm *et al.* [66] have studied the application of the coordinate transformation approach to 2-D squares. The transformation they used can be easily generalized to 3-D cases. This transformation, however, involves discontinuities in the variance of material properties of the cloak. We will present material properties of cloaks for rounded-cuboids with arbitrary aspect ratio, determined by an alternative coordinate transformation. In our approach, discontinuities are not involved.

We seek the possibility of representing a cuboid approximately by a *superellipsoid* [72, 73], bounded by the surface

$$\left[\left(\frac{x}{\alpha_1 b}\right)^{2/e} + \left(\frac{y}{\alpha_2 b}\right)^{2/e}\right]^{e/m} + \left(\frac{z}{\alpha_3 b}\right)^{2/m} = 1, \tag{2.41}$$

which has been well known in computer graphics and widely used to model a wide range of shapes, including rounded-cubes and rounded-cylinders [72]. Wriedt [73] introduced this shape to the light scattering community in his study of the T-Matrix method.

To approximate a cuboid, we let $e = m = 2/n$. Therefore, Eq.(2.41) becomes

$$\left(\frac{x^1}{\alpha_1 b}\right)^n + \left(\frac{x^2}{\alpha_2 b}\right)^n + \left(\frac{x^3}{\alpha_3 b}\right)^n = 1. \tag{2.42}$$

Eq.(2.42) is a direct generalization of Eq.(2.33) by replacing the exponent 2 with an integer n. We call this shape the *order-n-cuboid* for convenience. As can be seen in Fig. 26(a), an order-n-cuboid approaches a cube as the exponent n increases. In Fig. 26(b) we show the scattering pattern associated with an order-10-cuboidal scattering particle with $\alpha_1 = \alpha_2 = \alpha_3$ in comparison with that associated with a

cubical scattering particle with the same size parameter. As can be seen in this figure, an order-n-cuboid with $n = 10$ is already a good approximation of a cuboid as far as light scattering is concerned.

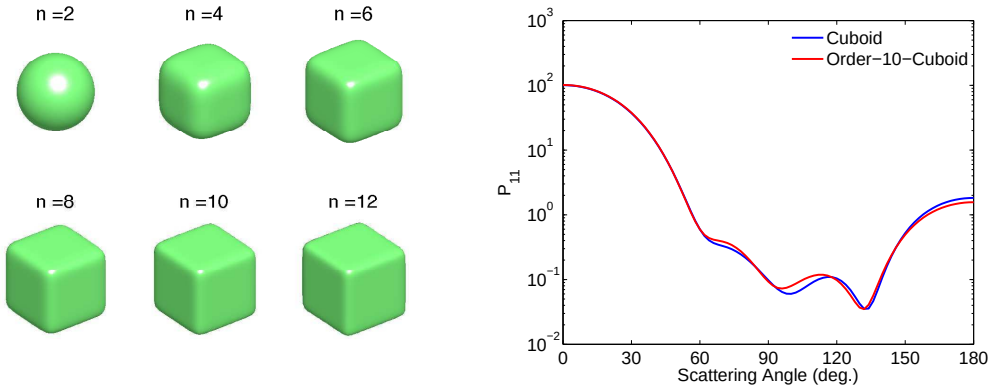

(a) (b)

Fig. 26. (a) Approximations of a cube by order-n-cuboids with various n values, and $\alpha_1 = \alpha_1 = \alpha_3$. (b) Comparison of phase functions pertaining to an order-10-cuboidal scattering particle with $\alpha_1 = \alpha_2 = 1$, $\alpha_3 = 2$ and to a cubical scattering particle. Both particles are homogeneous and have the same size parameter $x = 4$ and the same permittivity $\epsilon = 1.44$.

To determine the material property tensors of an order-n-cuboidal cloak, we can still use the coordinate transformation Eq.(2.34), and redefine the scaled magnitude r again as

$$r = \left[\sum_{i=1}^{3}\left(\frac{x^i}{\alpha_i}\right)^n\right]^{1/n}. \tag{2.43}$$

It can be easily verified that the outer boundary transforms to itself and the origin transforms to an inner boundary with b replaced by a.

Substituting Eqs.(2.34) and (2.43) into Eq.(2.18), we obtain the transformation matrix as follows:

$$\Lambda_j^{i'} = \frac{r'}{r}\delta_j^{i'} - \frac{a x^i \left(x^k\right)^{n-1} \delta_i^{i'} \delta_{kj}}{{\alpha_j}^n r^{n+1}}, \tag{2.44}$$

and a combination of Eqs.(2.17) and (2.44) gives the permittivity and permeability

tensors for an order-n-cuboidal cloak

$$\begin{aligned}\epsilon^{ij} &= \mu^{ij} \\ &= \frac{b}{b-a}\Bigg[\delta^{ij} - x^i x^j \times \\ &\quad \left(\frac{a}{r^3 \tilde{r}^{n-2}}\left(\frac{(\tilde{x}^i)^{n-2}}{{\alpha_i}^n} + \frac{(\tilde{x}^j)^{n-2}}{{\alpha_j}^n}\right) - \frac{a^2}{\tilde{r}^{2(n-1)} r^4} \sum_{k=1}^{3} \frac{(\tilde{x}^k)^{2n-2}}{{\alpha_k}^{2n}}\right)\Bigg], \end{aligned} \tag{2.45}$$

with r given by Eq.(2.43), $\tilde{r}$ and $\tilde{x}^i$ given by Eq.(2.40).

In Fig. 27, we show a rounded cuboidal cloak, approximated by an order-10-cuboid with $\alpha_1 = \alpha_2 = 1$, $\alpha_3 = 2$, and size parameter $x = 8$. Shown in the figure is the situation in the x-z plane. The light rays and wave fronts in the vicinity of the cloak predicted by the coordinate transformation are shown. Two particle orientations were considered. Again, the light rays and wave fronts deviate from the cloaked region. Therefore, any object in the cloaked region is hidden from outside observers.

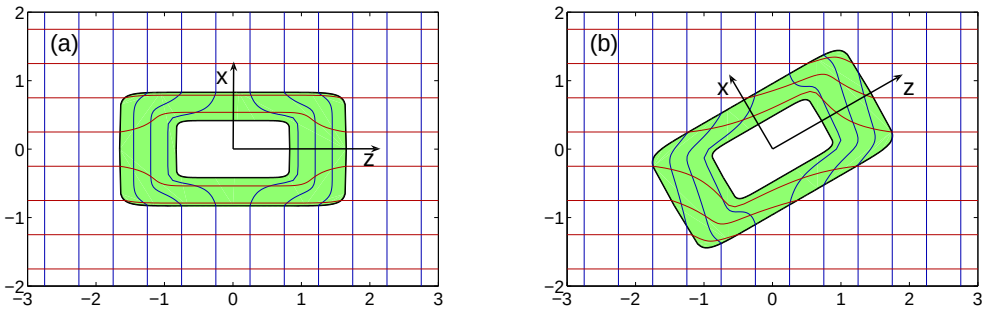

Fig. 27. Same as Fig. 24(b), but for a rounded cuboidal cloak approximated by an order-10-cuboid with $x = 8$, $a = 0.5b$, $\alpha_1 = \alpha_2 = 1$, and $\alpha_3 = 2$, subject to an incident plane wave propagating in various directions. (a) The incident plane wave is along the z-axis; (b) The incident plane wave is in the x-z plane, making an angle of $\theta = 30^\circ$ to the z-axis.

To approximate an elliptic cylinder of finite height, we start with Eq.(2.41), and

let $e = 1$ and $m = 2/n$. Therefore, Eq.(2.41) becomes

$$\left[\left(\frac{x^1}{\alpha_1 b}\right)^2 + \left(\frac{x^2}{\alpha_2 b}\right)^2\right]^{n/2} + \left(\frac{x^3}{\alpha_3 b}\right)^n = 1, \tag{2.46}$$

which we will call an *order-n-cylinder*. As Fig. 28(a) shows, an order-n-cylinder approaches a cylinder as the exponent n increases. The scattering patterns shown in Fig. 28(b) imply that an order-n-cylinder with $n = 10$ gives a good approximation to a cylinder as far as light scattering is concerned.

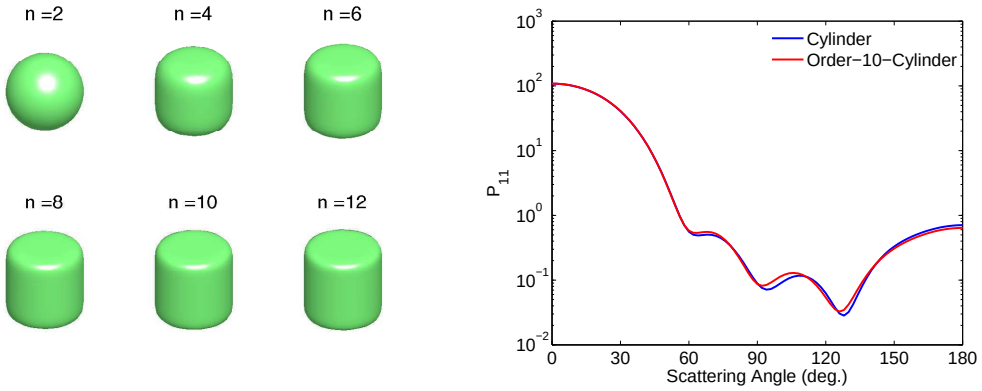

(a) (b)

Fig. 28. (a) Approximations of a cylinder by order-n-cylinders with various n values, and $\alpha_1 = \alpha_1 = \alpha_3$. (b) Same as Fig. 26(b), but for an order-10-cylindrical scattering particle of the same size parameter and aspect ratio, and a cylindrical scattering particle.

We can again use the same coordinate transformation Eq.(2.34) to determine material property tensors of an order-n-cylindrical cloak by redefining the scaled magnitude r as

$$r = \left(\left[\left(\frac{x^1}{\alpha_1}\right)^2 + \left(\frac{x^2}{\alpha_2}\right)^2\right]^{n/2} + \left(\frac{x^3}{\alpha_3}\right)^n\right)^{1/n}. \tag{2.47}$$

Again, the outer boundary transforms to itself and the origin transforms to an

inner boundary with b replaced by a. The corresponding transformation matrix will then be

$$\Lambda_j^{i'} = \frac{r'}{r}\delta_j^{i'} - \frac{a}{r^{n+1}}x^i\delta_i^{i'}\left[\frac{x^k\delta_{kj}\rho^{n-2}}{{\alpha_j}^2}\left(\delta_1^j+\delta_2^j\right)+\frac{\left(x^k\right)^{n-1}\delta_{kj}}{{\alpha_j}^2}\delta_3^j\right], \tag{2.48}$$

and the permittivity/permeability tensor for an order-n-cylindrical cloak is a hybrid of the corresponding tensors for an ellipsoidal cloak and for an order-n-cuboidal cloak, given by

$$\begin{aligned}
\epsilon^{ij} &= \mu^{ij} \\
&= \frac{b}{b-a}\Bigg[\delta^{ij} - x^ix^j \times \\
&\qquad \left(\frac{a}{r^3\tilde{r}^{n-2}}\left[\rho^{n-2}\left(\frac{1}{{\alpha_i}^2}\left(\delta_1^i+\delta_2^i\right)+\frac{1}{{\alpha_j}^2}\left(\delta_1^j+\delta_2^j\right)\right)+\right.\right. \\
&\qquad\qquad \left.\frac{\left(\tilde{x}^i\right)^{n-2}}{{\alpha_i}^n}\delta_3^i+\frac{\left(\tilde{x}^j\right)^{n-2}}{{\alpha_j}^n}\delta_3^j\right]- \\
&\qquad \left.\frac{a^2}{\tilde{r}^{2(n-1)}r^4}\left[\rho^{2n-4}\left(\frac{\left(\tilde{x}^1\right)^2}{{\alpha_1}^4}+\frac{\left(\tilde{x}^2\right)^2}{{\alpha_2}^4}\right)+\frac{\left(\tilde{x}^3\right)^{2n-2}}{{\alpha_3}^{2n}}\right]\right)\Bigg],
\end{aligned} \tag{2.49}$$

with r given by Eq.(2.47), $\tilde{r}$ and $\tilde{x}^i$ given by Eq.(2.40).

Note that when $z = 0$, Eq.(2.46) and Eq.(2.33) are identical, and Eq.(2.47) and Eq.(2.35) are identical; When $x = 0$ or $y = 0$, Eq.(2.46) and Eq.(2.42) are identical, and Eq.(2.47) and Eq.(2.43) are identical. Namely, for an order-n-cylindrical cloak, the wave fronts and light rays behave the same as that associated with an ellipsoidal cloak in the x-y plane (similar to the situation shown in Fig. 24(b) and Fig. 25(b)), and the same as that associated with an order-n-spherical cloak in the x-z plane and the y-z plane (same as the situation shown in Fig. 27).

To conclude this section, in Fig. 29 we present 3-D views of light rays and wave fronts associated with the three irregular invisibility cloaks we discussed.

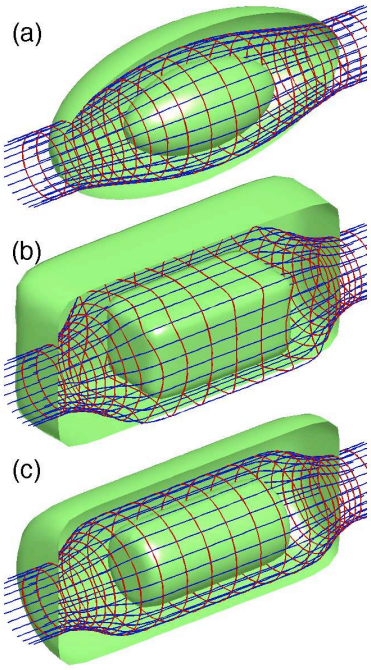

Fig. 29. 3-D views of light rays and wave fronts associated with the three irregular invisibility cloaks: (a) ellipsoid, (b) rounded-cuboid, and (c) rounded cylinder.

4. DDA Simulations of Irregular Invisibility Cloaks

To confirm the predictions given by these coordinate transformations, we simulated the light scattering pertaining to spheroidal cloaks, rounded cuboidal cloaks, and rounded cylindrical cloaks with the permittivity and permeability tensors given by Eq.(2.39), Eq.(2.45), and Eq.(2.49), respectively, using the DDA formalism discussed in Section II.2. The situations shown in Fig. 24(b), Fig. 25(b), and Fig. 27 are considered. Figure 30 shows the simulated electric-field distribution in the vicinity of an ellipsoidal cloak. DDA simulations for electric field distribution in the vicinity of a rounded cuboidal cloak are presented in Fig. 31. Both figures show the situation in the x-z plane. The DDA simulations in the x-z plane for a rounded cylindrical cloak look similar to Fig. 31. It can be noticed, in all three cases, that the plane-

wave feature outside of the cloak is perfectly kept. The field in the cloaking region is compressed into patterns that are consistent with the predictions of the coordinate transformation approach as can be seen in Fig. 24(b), Fig. 25(b), and Fig. 27. The field in the cloaked region is close to 0 with a leakage of about 10% of the radiating field, or about 1% of the radiative energy, into the cloaked region due to the discretization of material properties in the DDA calculations.

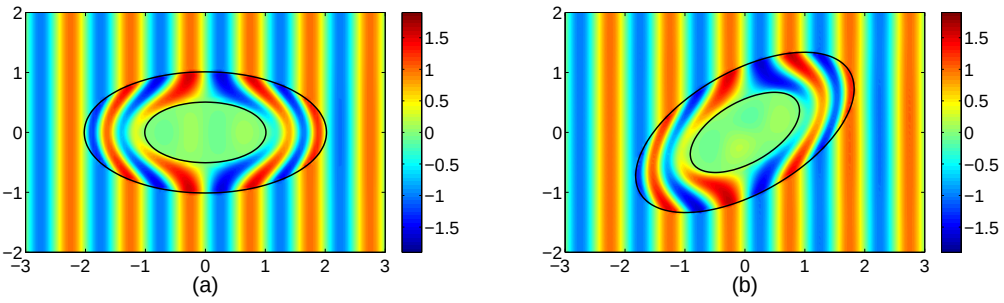

Fig. 30. The DDA simulations of the electric-field distribution in the vicinity of an ellipsoidal cloak in the x-z plane.

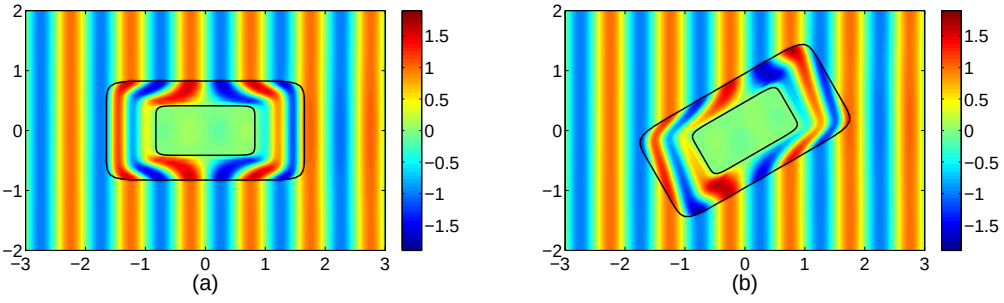

Fig. 31. The DDA simulations of the electric-field distribution in the vicinity of an order-10-cuboidal cloak in the x-z plane.

The simulated far field scattering is similar to that in the spherical case. In our

calculations for the three cloaks with size parameter $x = 8$, cloak parameter $a = 0.5b$, and two particle orientations, all simulated scattering efficiencies $Q_{\text{sca}} = C_{\text{sca}}/(\pi a_{\text{eff}}^2)$ are on the order of 10^{-3}, which is 3 orders lower than that for a regular dielectric particle. The simulated scattering efficiencies are on the order of 10^{-5} for smaller cloaks ($x = 5$) applied to smaller cloaked regions ($a = 0.3b$).

CHAPTER III

THE NATURE OF POLARIZED LIGHT IN DEEP OCEANS

In this chapter, we switch from single scattering to multiple scattering, specifically multiple scattering in deep oceans.

Generally, the polarized light fields described by the radiance and the polarization of light within a scattering and absorbing ocean depend not only on the optical properties of the medium, but also on the incident polarized light fields. The light fields vary as the optical depth from the surface increases. These complicated fields, however, become asymptotic at a considerable optical depth below the surface, where the photons have made enough collisions before they hit the detector, such that they have lost memory of their initial state. Below a critical depth, patterns of the radiance and the polarization depend only on the optical properties of the ocean and not on the incident light field; The radiance in a given direction decreases exponentially as $e^{-k\tau}$ with k the diffuse attenuation coefficient and τ the optical depth; The radiance and the polarization are azimuthally symmetric, and their dependence on the scattering nadir angle θ is independent of the optical depth. The region below this depth is called the *diffusion regime* (or the *asymptotic regime*).

The asymptotic light field underwater was first studied by Poole [74] for a medium with isotropic scattering assuming unpolarized light. Preisendorfer [75] indicated the possibility of extending the asymptotic field to a polarized case. Kattawar and Plass [76] have studied the integral equation for the asymptotic radiance and polarization, and have derived closed form solutions for scattering described by the Rayleigh phase matrix and numerical solutions for scattering described by other phase matrices.

The rate at which the unpolarized underwater light field approaches its asymptotic form has been thoroughly studied by Mobley [77] using the invariant embedding

method. In this study, the radiative transfer of a scalar light field was simulated with various values of the single scattering albedo ω_0 and various incident radiance distributions. It has been reported that for a point sun at a fixed zenith angle, and an ocean described by a Petzold scattering phase function and an albedo of $\omega_0 = 0.8$, the k-functions (the local decay rates of the radiance) all converge to within $\pm 0.2\%$ of the asymptotic value. And the larger ω_0 is, the more quickly the k-functions reach their asymptotic value.

In this chapter, we will investigate the asymptotic nature of the radiance and polarization in the underwater light field in an atmosphere-ocean system using a vector radiative transfer code. We will study how quickly the radiance and the polarization approach their asymptotic forms. We will find out how deep the asymptotic regime is in water bodies with various optical properties, e.g., single scattering albedo and phase function. Finally, we will discuss effects of wavelength, Raman scattering, and surface waves.

A. Methods to Solve Asymptotic Radiance

1. The Integral Equation for Asymptotic Radiance

We start with the scalar case, where the light field in the medium is described only by the radiance $I(\mu)$. As has been shown by van de Hulst [78], the integral equation that describes the asymptotic radiance is

$$(1 + k\mu)I(\mu) = \frac{1}{2}\omega_0 \int_{-1}^{1} h(\mu, \mu')I(\mu')d\mu', \tag{3.1}$$

where k is the diffusion exponent, $\mu = \cos\theta$ with θ as the scattering angle, ω_0 is the single scattering albedo, and $h(\mu, \mu')$ is the redistribution function defined by

$$h(\mu, \mu') = \frac{1}{2\pi} \int_0^{2\pi} \Phi \left[\mu\mu' + (1-\mu^2)^{1/2}(1-\mu'^2)^{1/2} \cos(\phi - \phi') \right] d\phi, \tag{3.2}$$

where Φ is the phase function for single scattering.

For some simple phase functions, e.g., the Rayleigh phase function, Eq.(3.1) can be solved analytically [76]. While for most phase functions with closed form expressions, and for those phase functions only available in tabulated form, such as the Petzold phase function, an analytical solution of Eq.(3.1) has not been achieved. In these cases, we discretize the equation and write the integral as a summation using the quadrature formulation

$$\begin{aligned} \mu &\rightarrow \mu_i, \\ \mu' &\rightarrow \mu_j, \\ \int_{-1}^{1} h(\mu, \mu') I(\mu') d\mu' &\rightarrow \sum_{j=1}^{N} h(\mu_i, \mu_j) I(\mu_j) w_j, \end{aligned} \tag{3.3}$$

where μ_i and μ_j are abscissas for the Gauss-Legendre quadrature over the interval $[-1, 1]$, w_j is the corresponding weight, and N is the order of the quadrature. With this discretization, Eq.(3.1) can therefore be rewritten in a matrix form

$$\tilde{\mathbf{h}} \cdot \mathbf{I} = k\mathbf{I}, \tag{3.4}$$

where $\tilde{\mathbf{h}}$ is an N by N matrix, and $\mathbf{I}$ is an N-component column vector, with elements

$$\begin{aligned} \tilde{h}_{ij} &= \frac{1}{\mu_i} \left(\frac{1}{2} \omega_0 h(\mu_i, \mu_j) w_j - \delta_{ij} \right), \\ I_j &= I(\mu_j). \end{aligned} \tag{3.5}$$

The solution to this eigensystem gives us the value of k as well as a discretized

distribution of the radiance P_j.

To include the polarization, we use the $\{I, Q, U, V\}$ Stokes vector representation. We have both $U = 0$ and $V = 0$ in the diffusion regime since the asymptotic solution is independent of the azimuthal angle. Therefore we can introduce a two-component representation as follows,

$$\begin{aligned} I(\mu) &\rightarrow \begin{bmatrix} I(\mu) \\ Q(\mu) \end{bmatrix}, \\ h(\mu, \mu') &\rightarrow \begin{bmatrix} h_{11}(\mu, \mu') & h_{12}(\mu, \mu') \\ h_{21}(\mu, \mu') & h_{22}(\mu, \mu') \end{bmatrix}. \end{aligned} \tag{3.6}$$

Using this notation, Eq.(3.1) becomes

$$(1 + k\mu) \begin{bmatrix} I(\mu) \\ Q(\mu) \end{bmatrix} = \frac{1}{2}\omega_0 \int_{-1}^{1} \begin{bmatrix} h_{11}(\mu, \mu') & h_{12}(\mu, \mu') \\ h_{21}(\mu, \mu') & h_{22}(\mu, \mu') \end{bmatrix} \cdot \begin{bmatrix} I(\mu) \\ Q(\mu) \end{bmatrix} d\mu'. \tag{3.7}$$

The discretized form of Eq.(3.7) can also be easily obtained using the quadrature formulation.

Kattawar and Plass have used the quadrature formulation to study asymptotic radiance and polarization for phase functions with closed form expressions, such as haze L and $C3$ cloud [76]. A twenty-one-point Gauss-Lobatto quadrature was used in their calculation.

In this study, we developed a `Fortran` code to solve the above eigensystem for phase functions that have closed-form expressions or only have tabulated values, utilizing the `LAPACK` libraries [79]. We have been able to solve the eigensystem using a Gauss-Legendre quadrature of as high an order as 1024 points.

2. The Multi-Component Approach

A fast code `RayXP` [80] has been developed by Zege *et al.* to simulate the radiative transfer of polarized light in a stratified plane-parallel atmosphere-ocean system. This code uses a combination of analytical and numerical techniques. The most important technique used in this code is the multi-component approach (MCA), which tremendously reduces the time consumption of simulations involving phase functions with strong forward peaks. In the two-component version of the MCA, such a phase function is decomposed into two components

$$p(\mu) = A_1 p^{(f)}(\mu) + (1 - A_1) p^{(d)}(\mu), \tag{3.8}$$

where the first term gives the forward peak in the small angle region and the second term gives the more diffuse remaining part of the phase function. The small-angle part, $p^{(f)}(\mu)$, is non-zero only when $\mu \geq \eta$,

$$p^{(f)}(\mu) = \frac{1}{A_1} \begin{cases} p(\mu) - p(\eta), & (\mu \geq \eta) \\ 0, & (\mu < \eta) \end{cases}, \tag{3.9}$$

where $A_1 = \frac{1}{2} \int_\eta^1 [p(\mu) - p(\eta)] d\mu$, and $\eta = \cos \beta_c$ with $\beta_c \leq 10^\circ - 20^\circ$ being an arbitrary truncation angle. By this means, the radiative transfer equation associated with a strongly anisotropic phase function is divided into a small-angle part and a diffuse part, where the strong forward peak is limited within the small-angle part. The radiative transfer associated with the small-angle part is solved assuming the small-angle diffusion approximation [81]. Therefore, what is left for us to solve is the radiative transfer equation associated with a fairly smooth phase function, which can be conveniently solved using the conventional adding-doubling method, where the reflection and transmission matrices for each homogeneous layer are computed from matrices for an element layer using the doubling procedure, and the resulting reflection and

transmission matrices for the whole inhomogeneous layer are computed from matrices for all sub-layers using the adding procedure. Following the standard procedure, the elements of Mueller matrix are expanded into series of Generalized Spherical Functions (GSF) with a finite number M of terms; the phase matrix, the reflection and transmission matrices are all expressed as Fourier series over the azimuthal angle ϕ. By treating the strong forward peak specifically, precise results could be achieved with much less run time. For the MCA scheme to be self-consistent, it is incumbent that the results be independent of the truncation angle β_c.

Polarized underwater light field computed by the MCA at various optical depths has been compared [82] with results given by the Monte Carlo method, which has been proven to give correct results. These comparisons showed that, for an atmosphere-ocean system where the ocean is described by a Henyey-Greenstein (H-G) phase function of $g = 0.75$ and has an optical thickness of $\tau = 1$, the MCA gives accurate results despite some minor discrepancies at a few scattering angles, however, the MCA is orders of magnitude faster than the Monte Carlo method.

Due to its fast computing time and satisfactory accuracy, the multi-component approach is capable of calculating radiance and polarization at optical depths in the range of the asymptotic regime. Thus the MCA provides an alternative method to compute the asymptotic radiance and polarization. Moreover, this method can show us how the light fields approach the asymptotic form as the optical depth increases. Before we can use the MCA to study the asymptotic radiance, however, it is necessary to investigate the accuracy of this method for an atmosphere-ocean system where the ocean is described by a strong anisotropic phase function ($g > 0.75$) and/or has a large optical thickness ($\tau > 1$).

3. Applicability and Calibration of the MCA

To explore the applicability of the multi-component approach in extreme conditions, we simulated the radiative transfer process in an atmosphere-ocean system where the ocean has a large optical thickness and strong anisotropic hydrosol scattering phase function. Our simulations reveal that for H-G phase functions with g greater than 0.8, the MCA fails to give self-consistent results at large optical depths. The computed radiance and polarization show appreciable dependence on the truncation angle β_c. To resolve this issue, we compared the MCA results at a sufficiently large optical depth with the asymptotic radiance and polarization computed by the integral equation method. This comparison can tell us which truncation angle gives the best asymptotic results, by which means we can "calibrate" the MCA method.

In our comparisons, we used three scattering phase functions: (a) an H-G phase function with $g = 0.99$; (b) an H-G phase function with $g = 0.995$; and (c) the Petzold phase function, a real measurement off the California coast [83], with an asymmetry factor of approximately $g = 0.92$. Monte Carlo simulations using this phase function have been performed, and agreement between the Monte Carlo computations and actual observations in the Mediterranean Sea have been reported [84]. In cases (a) and (b), all components of the phase matrix other than P_{11} are determined by the reduced Rayleigh phase matrix. In case (c), a reduced elastic fluctuation scattering matrix [84] with depolarization ratio $\rho = 0.047$ was used to account for the asymmetry of the ocean polarizability tensor.

Although vertical changes in the optical properties of the ocean have been reported, in these comparisons we assumed a semi-infinite ocean with constant optical properties for simplicity. The ocean has a refractive index of $n = 1.338$, a single scattering albedo of $\omega_0 = 0.5$, and is infinitely deep. The atmosphere was described by

the Rayleigh phase matrix, with an optical thickness $\tau = 0.15$ and a single scattering albedo $\omega_0 = 1$. A smooth surface was assumed in the simulation. The detector was located at optical depth $\tau = 100$ down from the surface. Through testing we have verified that the light fields do not change any more beyond this optical depth. The radiance given by the MCA is normalized such that

$$\int_{-1}^{1} p(\mu) d\mu = 2. \tag{3.10}$$

Comparisons of the results given by both MCA and IEM are shown in Fig. 32. In all calculations, we define the scattering nadir angle θ such that $\theta = 0$ ($\mu = 1$) corresponds to the light traveling directly downward.

It is evident from Fig. 32 that the MCA gives accurate results at large optical depth $\tau = 100$ for phase functions with as large an asymmetry factor as $g = 0.995$, provided that an appropriate truncation angle β_c was used in the MCA computation. The value of β_c may vary for different phase functions. Therefore, to obtain correct results for strong anisotropic phase functions using the MCA method, it is necessary to calibrate the MCA to find out the truncation angle that worked best for the specific phase function.

To validate the MCA method, we also compared the simulated radiance and degree of polarization with *in situ* measurements made in 1971 in the Mediterranean Sea [84]. In our simulations, we chose the same parameters as used in the previous Monte Carlo calculations [84]. Again the Petzold phase function was used as the hydrosol scattering function. The resultant radiance and degree of polarization at two sites, J2A and A2, are shown in Fig. 33. It turns out that there is remarkably good agreement between simulated results given by the MCA method and *in situ* measurements.

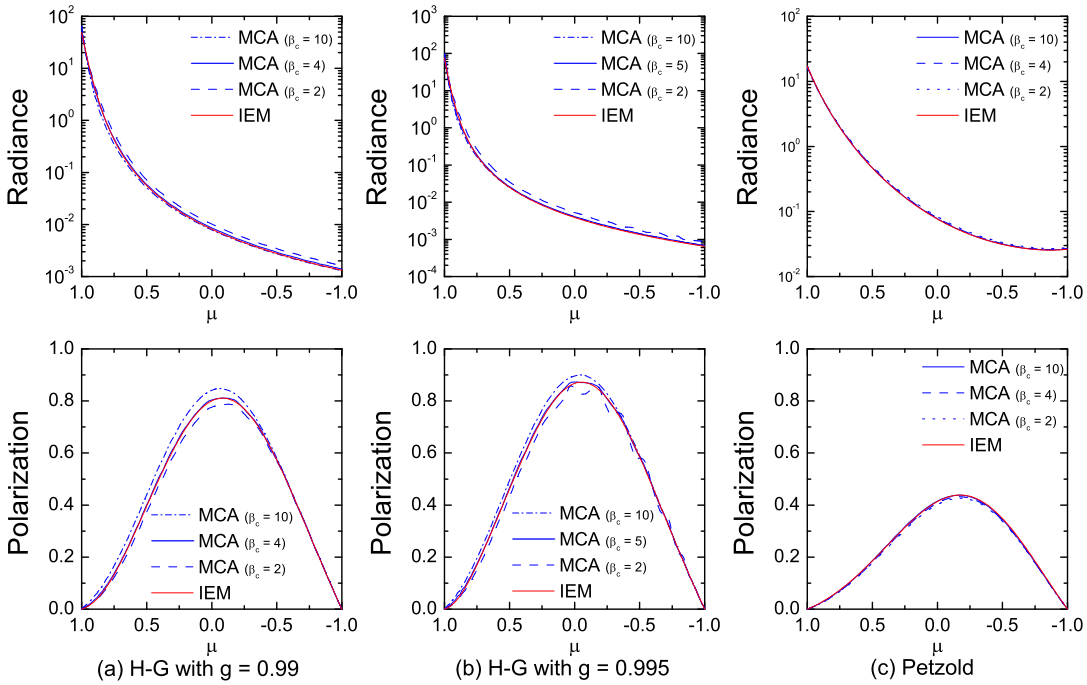

Fig. 32. Comparisons of the asymptotic radiance and polarization given by the MCA and the IEM, for (a) an H-G phase function with $g = 0.99$, (b) an H-G phase function with $g = 0.995$, and (c) the Petzold phase function with $g = 0.92$. A single scattering albedo $\omega_0 = 0.5$ was assumed. In the MCA computation, various β_c were used. $\beta_c = 4^\circ, 5^\circ$, and 10° give the best agreement for the three cases, respectively.

B. Numerical Results

1. The Polarized Underwater Light Fields

Having been calibrated, the MCA is capable of studying the asymptotic nature of the polarized underwater light fields. First of all, we need to get an idea of how the underwater light fields change as the optical depth increases. Shown in Fig. 34 is the underwater patterns of the Stokes parameters I, Q, U, as well as the degree of linear

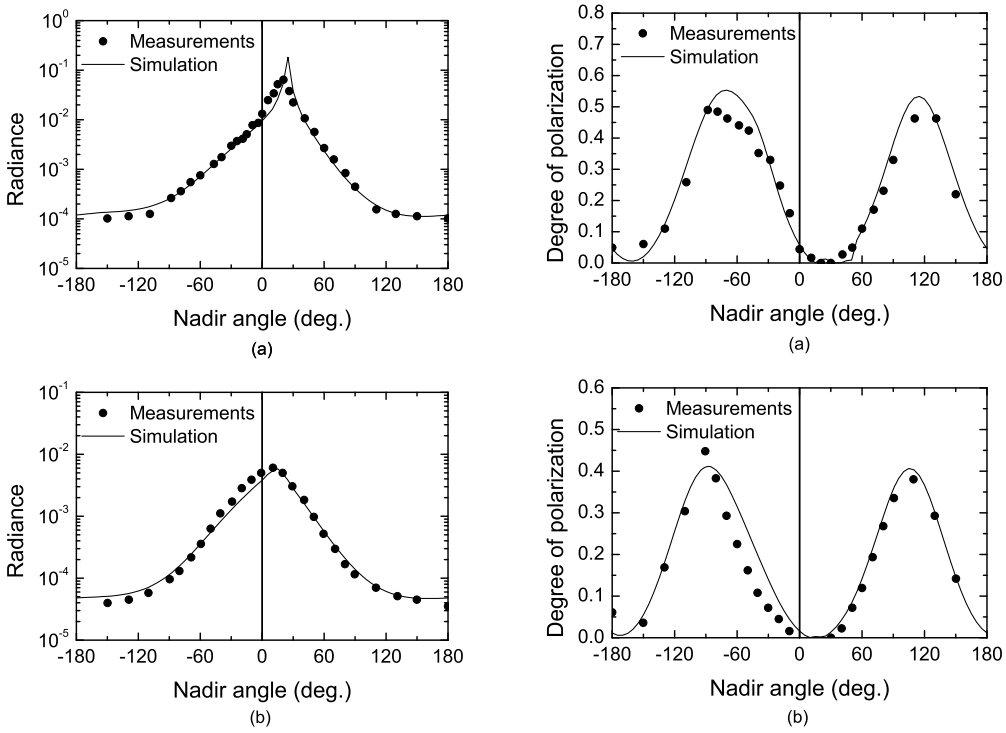

Fig. 33. Comparison of the measured (solid dots) and simulated (curves) radiance and degree of polarization at two sites, (a) J2A with solar zenith angle $\theta_s = 34°$ and physical depth $z = 50$ m, and (b) A2 with solar zenith angle $\theta_s = 21°$ and physical depth $z = 100$ m.

polarization $P = \sqrt{Q^2 + U^2}/I$, at selected optical depths for a unit solar spectral irradiance 1 W/(m^{2}nm). The computed radiance I is shown in units of W/(m^{2}nm). The Petzold phase function was used for the ocean, and a single scattering albedo $\omega_0 = 0.9$ was assumed. The solar zenith angle was $\theta_s = 30°$.

Figure 34 shows that as the optical depth increases, all I, Q, U, and P approach asymptotic and azimuthal-independent forms. It can also be noticed that I becomes asymptotic faster than Q, U, and P.

Before going further, it is necessary to have an idea of the relation between the "optical depth" τ, mostly used by physicists, and the "physical depth" z, mostly

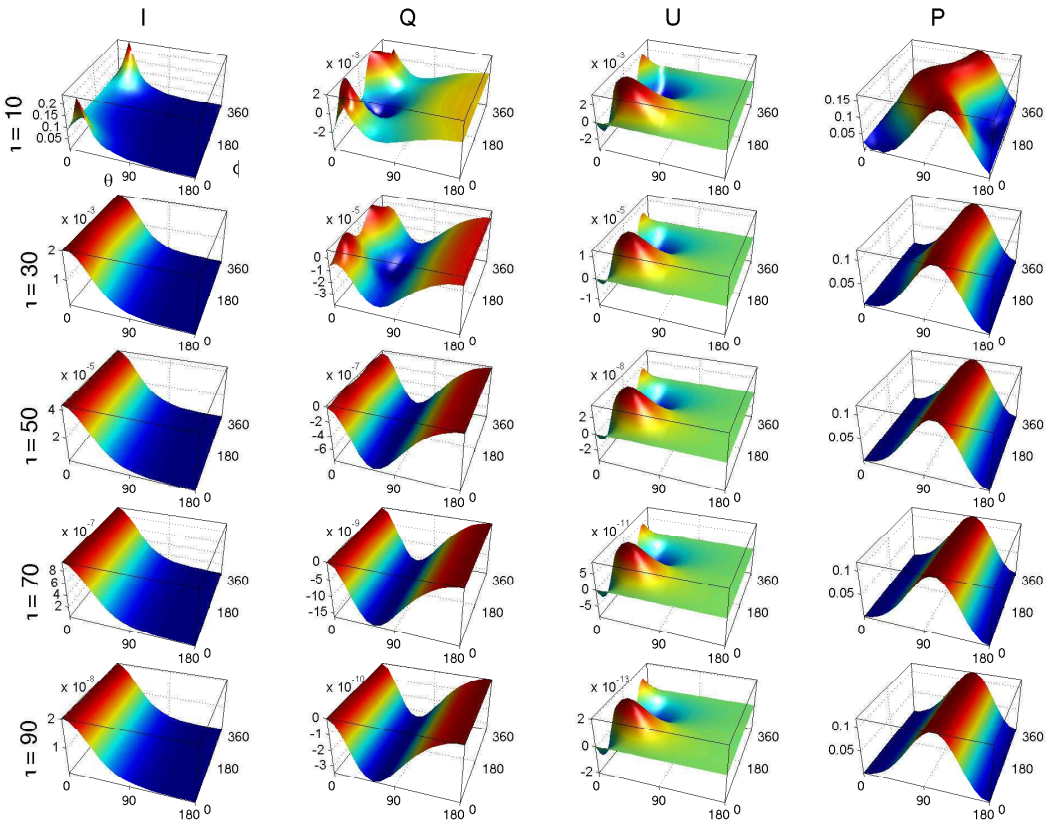

Fig. 34. Underwater Stokes parameters I, Q, U and the degree of linear polarization P at selected optical depths. The Petzold phase function was used for the ocean, and a single scattering albedo $\omega_0 = 0.9$ was assumed.

used by oceanographers. In the radiative transfer equation, what really matters is the optical depth, while the real-world measurements are in terms of the physical depth, which is related to the optical depth by $z = \tau/K$, with K the extinction coefficient or the attenuation coefficient. The attenuation coefficient varies substantially in the ocean, and the correspondence between the optical depth and the physical depth vary accordingly. Assuming a homogeneous water body with attenuation coefficients as measured at various locations [84, 85, 86, 87, 88], the corresponding physical depths are shown in Fig. 35.

To quantitatively study the underwater light fields as we approach the asymptotic

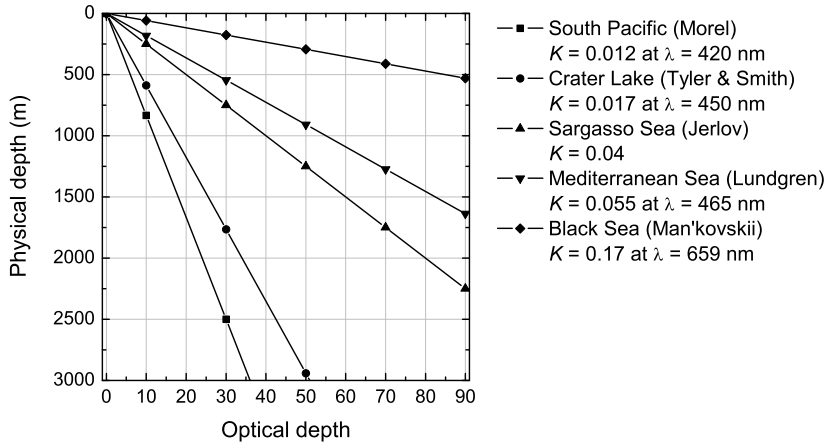

Fig. 35. Physical depth z versus the corresponding optical depth τ for attenuation coefficients measured at various locations.

regime, we show the radiance and polarization patterns in the principal plane at selected optical depths in Fig. 36. In the principal plane, $U = V = 0$. Therefore, the degree of polarization is defined as $P = -Q/I$. For comparison, the corresponding asymptotic radiance and polarization patterns are also shown in gray dashed lines. We assumed a unit incident solar spectral irradiance again, and the underwater radiance is in units of W/(m^{2}sr·nm). The asymptotic radiance pattern is normalized to have the same value at nadir angle 0° as the computed radiance patterns at each optical depth.

As can be seen in Fig. 36(a), for optical depths $\tau < 10$, there is a radiance maximum at the scattering nadir angle $\theta_{\rm rad} = 22°$, which coincides with the directly refracted solar beam at 21.94°. As the detector moves deeper, $\theta_{\rm rad}$ starts to move and will finally approach 0°. A visual comparison of this figure suggests that the radiance at $\tau = 50$ is almost identical to the asymptotic form. Figure 36(b) shows that in water where $\tau \leq 20$, there is a local polarization minimum at the nadir angle

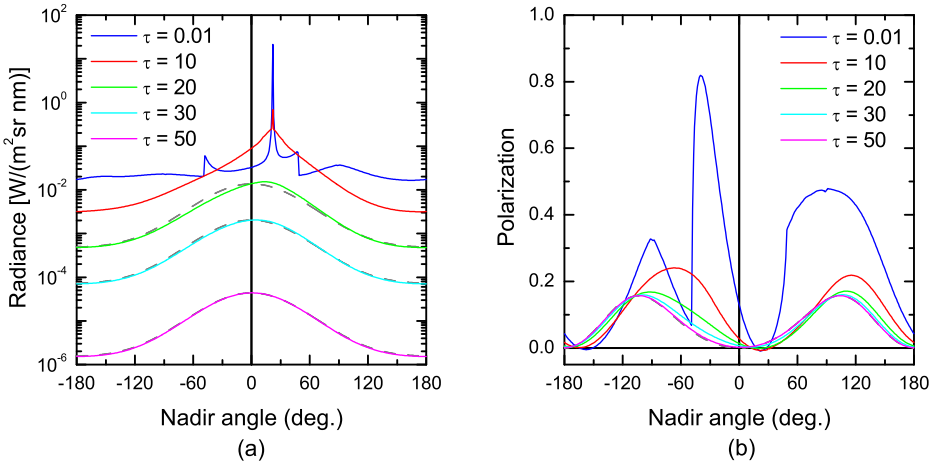

Fig. 36. Underwater radiance and degree of polarization patterns in the principal plane, computed from the MCA method at selected optical depths. The corresponding asymptotic radiance and polarization computed from the integral equation method are also shown in gray dashed curves for comparison. The Petzold phase function was used for the ocean, and a single scattering albedo $\omega_0 = 0.9$ was assumed.

$\theta_{\text{pol}} = 22°$, which will also move to 0°. At $\tau = 50$, the polarization pattern is very close to the asymptotic form. Since visual comparison could not provide us with a precise asymptotic depth, we use the nadir angles θ_{rad} and θ_{pol} as indicators for the asymptotic depths of the underwater radiance and polarization. When θ_{rad} and θ_{pol} become 0°, we say that we have reached the asymptotic regimes for the underwater radiance and polarization, respectively.

We then show the movement of θ_{rad} and θ_{pol} as a function of the optical depth τ in Fig. 37(a). Results for two cases, solar zenith angles $\theta_s = 30°$ and $\theta_s = 60°$, are shown here. What is more, since the light in the ocean attenuates exponentially as it propagates downward, it is possible that the radiance has become too small to

be detected before the light field becomes asymptotic, in which case the asymptotic regime will be out of the range of any practical experimental measurement. Therefore, it is also important to show θ_{rad} and θ_{pol} as function of the spectral downward plane irradiance, $E_d = \int_0^{2\pi} d\phi \int_0^{\pi/2} d\mu |\mu| p(\mu, \phi)$, as the detector moves downward, which is shown in Fig. 37(b).

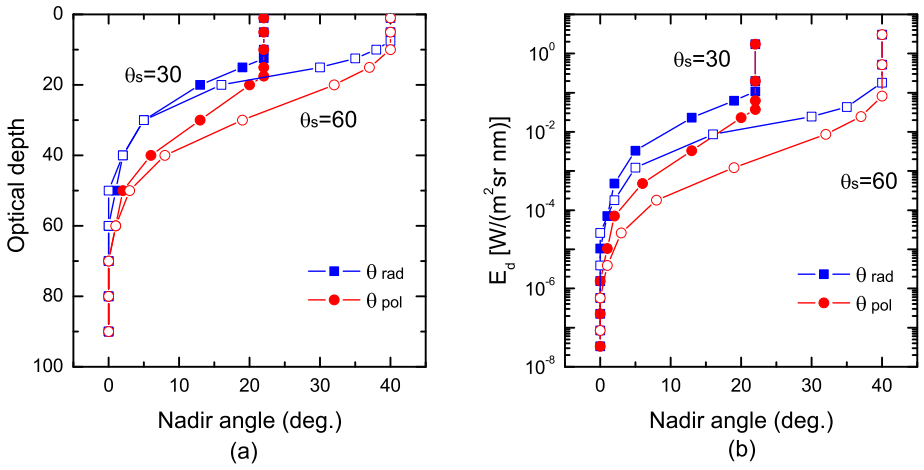

Fig. 37. Movement of θ_{rad} and θ_{pol} as the optical depth increases and the downward plane irradiance decreases. The Petzold phase function was used for the ocean, and a single scattering albedo $\omega_0 = 0.9$ was assumed. Two solar zenith angles $\theta_s = 30°$ (curves with solid symbols) and $\theta_s = 60°$ (curves with open symbols) are shown.

Figure 37(a) shows that when $\theta_s = 30°$, θ_{rad} starts to move at $\tau = 12.5$ and becomes 0° at $\tau = 60$, which will be defined to be the top of the asymptotic regime (TAR) for the radiance; and θ_{pol} starts to move at $\tau = 17.5°$ and becomes 0° at $\tau = 70$, the TAR for the polarization. When $\theta_s = 60°$, θ_{rad} and θ_{pol} start to move at $\tau = 7.5°$ and $\tau = 12.5°$, respectively, and become 0° at the same optical depths as before. It is interesting to note that, as the optical depth increases, the radiance

reaches its asymptotic form more quickly than does the polarization. Therefore, the TAR for the polarization is also the TAR for the polarized light fields. These results also verify that the TAR's are independent of the incident solar zenith angle.

In Fig. 37(b), it can be found that at the TAR for the polarized light field, the downward plane irradiance E_d is on the order of 10^{-6} W/(m^{2}nm) for a unit solar spectral irradiance. Remember that the solar spectral irradiance around 500 nm is roughly 2 W/(m^{2}nm), therefore the irradiance at the TAR in this case is sufficient to be detected.

2. Single Scattering Albedo Effects

The single scattering albedo in real oceanic waters varies a lot. To understand the effects of the single scattering albedo to the TARs, the same simulations were repeated, but for an ocean with a smaller single scattering albedo $\omega_0 = 0.5$. The results are shown in Fig. 38.

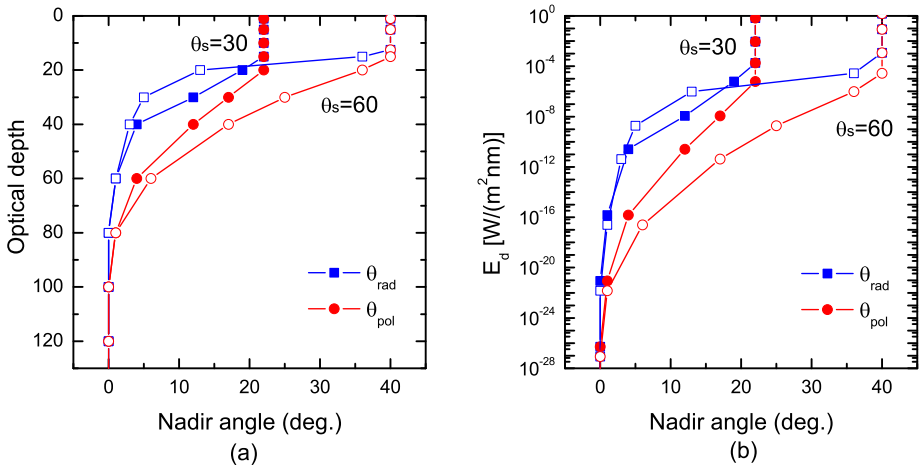

Fig. 38. Same as Fig. 37, but with a single scattering albedo of $\omega_0 = 0.5$ for the ocean.

As can be seen in Fig. 38, for a smaller single scattering albedo $\omega_0 = 0.5$ the TAR for the polarized light field is at optical depth $\tau = 100$, which is a little larger than before. However, at this depth we only have a downward plane irradiance of 10^{-27} W/(m^{2}nm), which is far too small to be detected. This is reasonable since for a smaller ω_0, the photons are more likely to be absorbed rather than being scattered by the scattering particles. Therefore, it needs more multiple scattering, i.e., larger optical depth, for the light fields to reach the asymptotic forms, and the radiance attenuates more quickly.

Shown in Fig. 39 are the optical depth of the TAR and the radiance maximum at the TAR for the underwater radiance and polarization for a homogeneous ocean with ω_0 varying between 0.5 and 0.9. This is the range in which ω_0 varies for wavelengths from 400 nm to 600 nm according to the Case 1 water model [77, 89]. The Petzold phase function was used in these simulations.

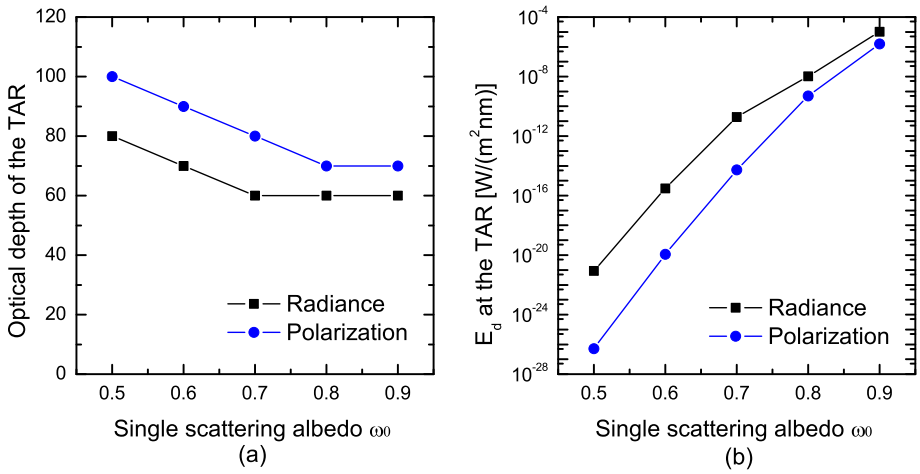

Fig. 39. (a) The optical depth of the TAR and (b) the spectral downward plane irradiance E_d at the TAR for the radiance and polarization, as ω_0 varies from 0.5 to 0.9. A unit solar spectral irradiance was assumed.

Figure 39(a) shows that, for a homogeneous water body with $\omega_0 \geq 0.8$, the TAR for the radiance is approximately at optical depth $\tau = 60$, and the TAR for the polarization is approximately at $\tau = 70$. One can also see from Fig. 39(b) that E_d at the TAR decreases exponentially as ω_0 decreases. When $\omega_0 \geq 0.8$, E_d at the TAR for the polarized light fields could be on the order of 10^{-9} W/(m^{2}nm), which is still sufficient to be detected. However, when $\omega_0 < 0.8$, there are far too few photons at this depth to give a meaningful measurement of irradiance.

3. Phase Function Effects

We next wanted to study how the asymmetry of the ocean phase function would affect the asymptotic light fields. Here we used the Fournier-Forand (F-F) phase function [90, 91], which is derived for an ensemble of hydrosol particles that have a hyperbolic (Junge-type) particle size distribution. The two-parameter analytic F-F phase function is determined by n, the refractive index of scattering particles relative to water and ν, a Junge parameter in the size distribution of hydrosol particles, as

$$p(\mu) = \frac{A(1+\mu^2)}{(1-\delta)^2\delta^w}\left\{[w(1-\delta)-1+\delta^w] + \frac{2}{1-\mu}\left[1-\delta^{w+1}-(1+w)(1-\delta)\right]\right\}, \tag{3.11}$$

where A is a normalization factor and

$$w = \frac{3-\nu}{2}, \quad \delta = \frac{2(1-\mu)}{3(n-1)^2}. \tag{3.12}$$

Mobley *et al.* have shown [92] that for an unknown water body, the F-F phase function can provide a satisfactory substitute for the particle phase function, given a

measured backscatter fraction

$$b_p = \frac{1}{2}\int_{-1}^{0} p(\mu)d\mu. \tag{3.13}$$

Since the backscatter fraction of the Petzold phase function is $b_p = 0.0183$, we simulated the ocean with two F-F phase functions: (i) the first was generated using $n = 1.09$ and $\nu = 3.8$, with $b_p = 0.02$ and $g = 0.92$, representing a Petzold-like water body; and (ii) the second was generated using $n = 1.14$ and $\nu = 4.6$, with $b_p = 0.2$ and $g = 0.53$, representing a water body with a much less anisotropic phase function. The single scattering albedo was still $\omega_0 = 0.9$. The nadir angles $\theta_{\rm rad}$ and $\theta_{\rm pol}$ as a function of the optical depth and the downward plane irradiance are presented in Fig. 40.

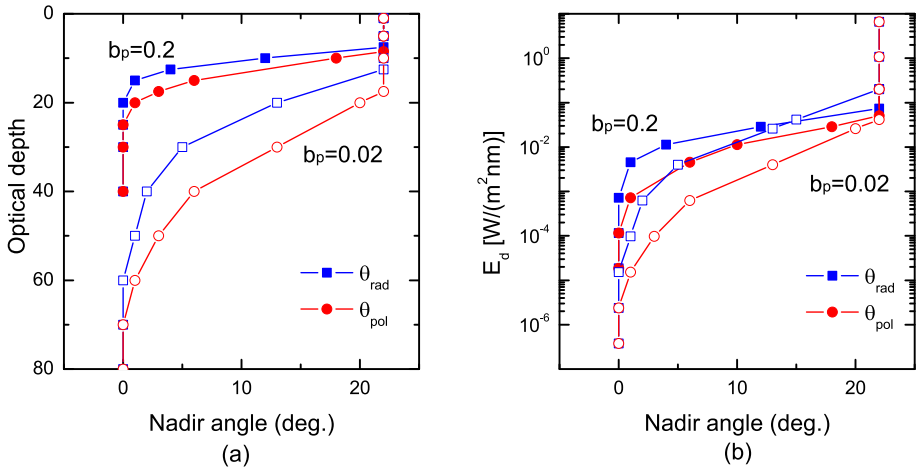

Fig. 40. Movement of $\theta_{\rm rad}$ and $\theta_{\rm pol}$ as (a) the optical depth increases and (b) the downward plane irradiance decreases, for F-F phase functions with (i) $b_p = 0.02$ (curves with open symbols) and (ii) $b_p = 0.2$ (curves with solid symbols).

Figure 40 shows that the results in case (i) are similar to those for the Petzold phase function. While in case (ii), the underwater light fields become asymptotic

much more quickly. The optical depth of the TAR in this case is less than half of that in case (i), and the downward plane irradiance at the TAR is two orders larger. These comparisons imply that if the ocean phase function were less anisotropic, the asymptotic regime will be reached at a smaller optical depth, and it is possible that the asymptotic regime could be reached experimentally for an ocean with a smaller ω_0.

4. More Realistic Water Model

Previously, we assumed a homogeneous water body with a constant single scattering albedo ω_0 and a constant attenuation coefficient K. In real oceanic waters, however, the absorption coefficient $a = a(\lambda, z)$ and the scattering coefficient $b = b(\lambda, z)$ both depend on the wavelength and the physical depth. For example, in phytoplankton-dominated Case 1 waters, the optical properties of the water are mainly described as a function of the wavelength and the chlorophyll concentration, which in turn is a function of the physical depth. Therefore, the asymptotic nature of the underwater light fields will vary accordingly. Firstly, the single scattering albedo $\omega_0 = b/(a+b)$ can be substantially different at different wavelengths. Secondly, the physical depth corresponding to an optical depth would vary with wavelength, since the extinction coefficient $K = a+b$ varies. Shown in Fig. 41 is a contour plot of the single scattering albedo ω_0 as a function of the wavelength and the physical depth according to the Case 1 water model, where the black lines are the contour lines for $\omega_0 = 0.75$ and $\omega_0 = 0.8$. Here, we used a chlorophyll profile that gives a good fit to the measured values of the fairly high chlorophyll concentration in coastal waters of the Celtic Sea [77, 93]. This chlorophyll concentration profile has a maximum of $\mathrm{Chl}(z) = 6.6\ \mathrm{mg/m^3}$ at $z = 17$ m, and becomes less than $0.5\ \mathrm{mg/m^3}$ when $z > 40$ m. In this case, when wavelength $\lambda < 570$ nm, ω_0 is greater than 0.8 for physical depth up to 40 m; at

physical depth greater than 40 m, ω_0 becomes essentially constant, but is still greater than 0.75 for wavelengths $\lambda < 500$ nm. Thus we can expect to reach the asymptotic regime within this waveband.

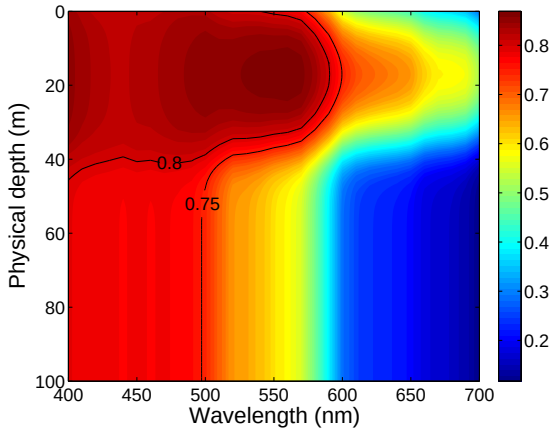

Fig. 41. Single scattering albedo ω_0 as a function of the wavelength and the physical depth.

In Fig. 42, we show the optical depth τ as a function of the wavelength and the physical depth. The two black curves are the contour lines for $\tau = 60$ and $\tau = 70$, which correspond to the TAR for the radiance and the TAR for the polarization, respectively, when $\omega_0 \geq 0.8$. For wavelengths $\lambda < 500$ nm, the TAR for the radiance varies from physical depth 130 m to 200 m, while the TAR for the polarization varies from 180 m to 260 m.

As a consequence of the varying single scattering albedo and optical depth, the downward radiance at the top of the asymptotic regime also varies with wavelength. Specifically, due to the small single scattering albedo at longer wavelengths, the elastically scattered light would be extremely dark in deep water, whereas the contribution due to Raman scattered photons plays an important role in the underwater light field. Berwald *et al.* [94] have studied the effect of Raman scattering on the diffuse attenuation coefficient k and the average cosine of irradiance in the ocean, assuming

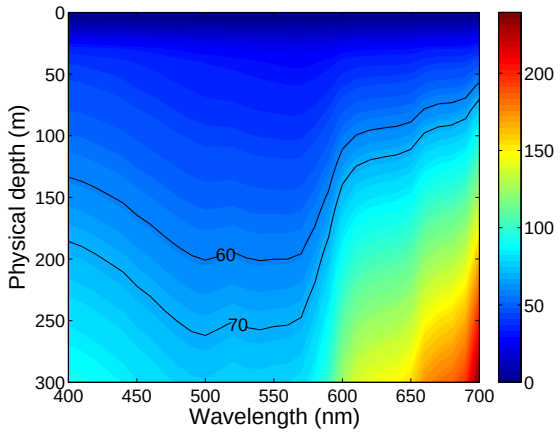

Fig. 42. The optical depth τ as a function of the wavelength and the physical depth.

a constant chlorophyll concentration. Here we want to show this effect for a water body with varying chlorophyll concentrations.

We simulated the underwater light field at physical depths down to 250 meters, with and without contributions from Raman scattering. Again, the solar zenith angle was $\theta_s = 30°$, the Case 1 water model was used, and the Petzold phase function was used as the hydrosol scattering phase function. A powerful code developed by Mobley and Sundman, the `HydroLight` [95], was used to do this simulation, since it has Raman scattering contributions conveniently built-in. Shown in Fig. 43 is the simulated downward irradiance E_d at various wavelengths and selected physical depths from above the ocean surface ($z = \epsilon$) down to the TAR. Here the solid lines are irradiance with Raman scattering, while the dashed lines are that without Raman scattering.

A combination of Fig. 42 and Fig. 43 reveals that, for 480 nm $\leq \lambda \leq$ 500 nm, the downward irradiance E_d at the TAR for the radiance ($z = 200$ m) is over 10^{-8} W/(m^{2}nm). For $\lambda = 400$ nm, E_d at the TAR for the radiance ($z = 130$ m) is about 10^{-7} W/(m^{2}nm). When λ decreases from 480 nm to 400 nm, the physical

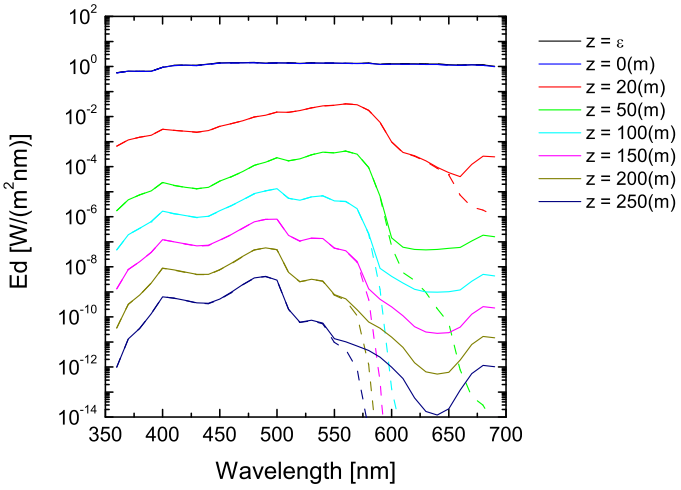

Fig. 43. The downward irradiance E_d at various physical depths, as a function of the wavelength. Solid lines are results with Raman scattering, while dashed lines are results without Raman scattering.

depth of the TAR for the radiance goes from 200 m to 130 m, and the downward irradiance is always above 10^{-8} W/(m^{2}nm). The downward irradiance at the TAR for the polarization is about one order of magnitude lower. What is more, Fig. 43 shows that at the TAR, the contribution from Raman scattering starts to show up in the underwater light field at $\lambda \geq 550$ nm, and becomes more and more important as the wavelength increases.

To show more details on the angular distribution of the radiance, we plot the underwater radiance patterns in the principal plane at various depths and selected wavelengths in Fig. 44.

It is clearly shown in these plots that at shorter wavelengths $\lambda \leq 510$ nm, Raman scattering has little effect on the underwater light field, and the light field down to the TAR is solely determined by the elastic scattering. At longer wavelengths $\lambda \geq 570$ nm, the contributions from Raman scattering significantly change the radiance patterns in

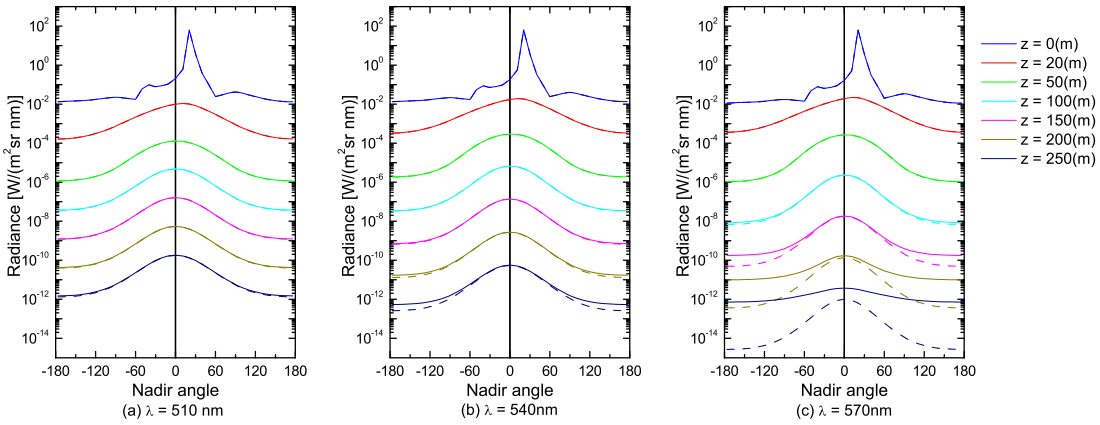

Fig. 44. Underwater radiance patterns at various depths and selected wavelengths, for a solar zenith angle of $\theta_s = 31°$. Dashed curves are results without contributions from Raman scattering, and solid curves are results with contributions from Raman scattering.

the deep ocean, such that the asymptotic characteristics of the elastic-scattered light field is destroyed. In the wavelength band 510 nm $< \lambda <$ 540 nm, Raman scattering does change the underwater light field appreciably, but the overall radiance pattern remains the same, and could still give us some information on the asymptotic nature of the elastic-scattered light.

In real oceanic waters, another factor affecting the underwater light field are surface waves, which can substantially change the light field in shallow water. However, it remains unknown whether effects of the surface wave shows up down in the asymptotic regime. To study this, we performed simulations involving roughed surface associated with various wind speeds following the wave-slope wind-speed law proposed by Cox and Munk [96]. The wavelength was $\lambda = 510$ nm. The resultant radiance at various physical depths associated with wind speeds $U = 0$, 5, and 10 (m/s) are shown in Fig. 45.

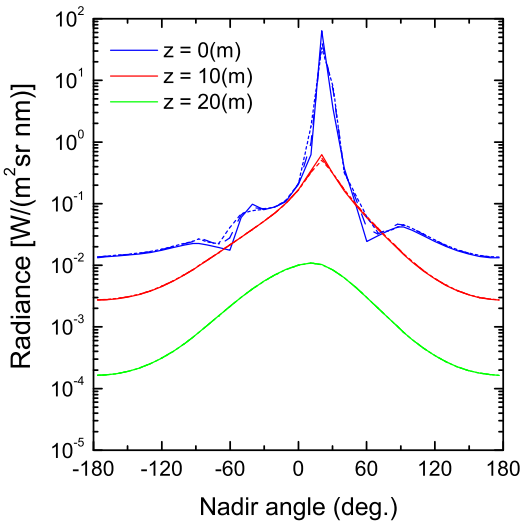

Fig. 45. Underwater radiance patterns at various depths associated with various wind speeds, for a solar zenith angle of $\theta_s = 31°$. Solid curves, dashed curves, and dotted curves correspond to wind speeds $U = 0$, 5, and 10 (m/s), respectively.

Figure 45 reveals that effects of surface waves only appear in shallow water. Just below the surface, the radiance patterns differ substantially as the wind speed varies. At depth $z = 10$ m, the radiance patterns show little difference. At depth $z = 20$ m, which is still far above the asymptotic depth, the radiance patterns are almost identical for all wind speeds. This assures us that surface wave effects will be of no consequence in the asymptotic regime.

CHAPTER IV

SUMMARY AND CONCLUSIONS

In this study we have applied generalized Discrete Dipole Approximation formalisms to simulations of inelastic scattering and studies of invisibility cloak. We have also investigated the asymptotic nature of the polarized light in deep oceans.

A. Application of the DDA Formalism to Inelastic Scattering

We have generalized the conventional DDA formalism for an incident plane wave field to the incident field induced by oscillating dipoles embedded in a host particle. Special attention has been paid to the coupling of the diverging local field of an oscillating dipole and the DDA dipoles in its immediate proximity. The local field correction has been considered. Two schemes of locating the source dipoles were compared, and the interstitial scheme, in which a source dipole is located at the center of a DDA cell, was found to be superior to the substitutional scheme. Comparisons between the DDA results and analytical results for a single embedded source dipole suggest that, for scattering particle with refractive index $m \leq 2$, DDA computations give accurate solutions to total radiated power as well as the angular dependence of the radiated power per solid angle, provided that $mkd < 0.5$. If $mkd > 0.5$, DDA computations could still give reasonable results for angular dependence of the radiated power per solid angle with relative errors within $\pm 30\%$ at most scattering angles and could predict the shape of the radiation patterns with reasonable accuracy.

We have also applied the generalized DDA formalism to computations of incoherent Raman scattering. With simple assumptions on how the source dipole are induced by the local exciting field, the DDA simulated inelastic-scattering patterns pertaining to spherical host particles agree with corresponding analytic results. We

also simulated the inelastic-scattering radiation from a spore-like particle represented by a layered prolate spheroid, with various distributions of the active molecules within the host particle. Our results suggest that the inelastic-scattering patterns provide useful information on the distribution of the active molecules.

B. Application of the DDA Formalism to Invisibility Cloak

We have generalized the conventional DDA formalism for dielectric particles to particles with both non-unit electric permittivity and non-unit magnetic permeability. Besides the electric part of the responses of the scattering particle to the incident electromagnetic field, we also included the magnetic part in the generalized formalism. We have used this formalism to simulate the scattering of a spherical invisibility cloak made from metamaterial with inhomogeneous and anisotropic electric permittivity and magnetic permeability, and the DDA simulations agree with theoretical predictions.

We have explored the possibility of invisibility cloaks for particles with irregular shapes. The electric permittivity and magnetic permeability tensors of invisibility cloaks for ellipsoids, rounded-cuboids, and rounded-cylinders have been derived using the coordinate transformation method. DDA computations have been performed for an object embedded within invisibility cloaks with these geometries. The simulated results have confirmed that particles with the designated permittivity and permeability tensors keep the electromagnetic fields in the external region unchanged as if neither the cloaked object or the cloak itself exists.

The DDA calculations, however, can not give an exact zero scattering, as the material specifications realized in the DDA formalism is a discretization of the continuously varying material properties required for an invisibility cloak. The simulated

scattering efficiencies of a cloaked object in various cases are three orders lower than that of it when uncloaked, which partially shows the cloaking effects.

C. The Nature of Polarized Light in Deep Oceans

We have studied the asymptotic nature of the polarized light in deep oceans using a fast multi-component approach. It has been found that the radiance of the light fields approaches its asymptotic form more quickly than the polarization does. Therefore, a vector radiative transfer solution is necessary for asymptotic light field studies.

Our simulations have also shown that the larger the single scattering albedo, and the less anisotropic the oceanic scattering phase function, the more quickly the asymptotic regime can be reached, and the larger irradiance there would be in the asymptotic regime. For a typical water body whose scattering property is characterized by the Petzold phase function, a single scattering albedo of $\omega_0 > 0.8$ is required in order that the asymptotic regime can be reached before there are too few photons to be detected.

We have also investigated the effects of wavelength, Raman scattering and surface waves for a scalar light field in a more realistic water body with high chlorophyll concentration described by the Case 1 water model. It turned out that for wavelengths $\lambda < 540$ nm, the contribution from Raman scattering can be reasonably neglected. What is more, surface waves do not affect the radiance pattern in the asymptotic regime.

REFERENCES

[1] H. C. van de Hulst, *Light scattering by small particles* (Dover, New York, 1981).

[2] C. F. Bohren and D. R. Huffman, *Absorption and scattering of light by small particles* (Wiley, New York, 1983).

[3] M. I. Mishchenko, L. D. Travis, and A. A. Lacis, *Scattering, absorption, and emission of light by small particles* (Cambridge U. Press, Cambridge, UK, 2002).

[4] G. G. Stokes, "On the composition and resolution of polarized light from different sources," Transactions of the Cambridge Philosophical Society **9,** 399 (1852).

[5] J. C. Maxwell, "A dynamical theory of the electromagnetic field," Royal Society Transactions **155,** 459-512 (1865).

[6] J. D. Jackson, *Classical Electrodynamics* (John Wiley & Sons, New York, 1975).

[7] K. S. Yee, "Numerical solution of initial boundary problems involving Maxwell's equations in istotropic media," IEEE Trans. Antennas Propag. **AP-14,** 302-307 (1966).

[8] A. Taflove and S. Hagness, *Computational electrodynamics: the finite-difference time-domain method* (Artech, Boston, 2000).

[9] E. M. Purcell and C. R. Pennypacker, "Scattering and absorption of light by nonspherical dielectric grains," Astrophys. J. **186,** 705-714 (1973).

[10] P. Waterman, "Matrix formulation of electromagnetic scattering," Proc. IEEE **53,** 805-812 (1965).

[11] M. I. Mishchenko, L. D. Travis, and D. W. Mackowski, "T-Matrix computations of light scattering by nonspherical particles: a review," J. Quant. Spectrosc. Radiat. Transfer **55,** 535-575 (1996).

[12] P. Yang, K. N. Liou, "Geometric-optics-integral-equation method for light scattering by nonspherical ice crystals," Appl. Opt. **35,** 6568-6584 (1996).

[13] S. Chandrasekhar, *Radiative transfer* (Dover, New York, 1960).

[14] M. I. Mishchenko, L. D. Travis, and A. A. Lacis, *Multiple scattering of light by particles: radiative transfer and coherent backscattering* (Cambridge U. Press, Cambridge, UK, 2006).

[15] S. Twomey, H. Jacobowitz, and H. B. Howell, "Matrix methods for multiple-scattering problems," J. Atmos. Sci. **23,** 101-108 (1966).

[16] S. Twomey, H. Jacobowitz, and H. B. Howell, "Light scattering by cloud layers," J. Atmos, Sci. **24,** 70-79 (1967).

[17] G. N. Plass, G. W. Kattawar, and F. E. Catchings, "Matrix operator theory of radiative transfer. 1: Rayleigh scattering," Appl. Opt. **12,** 314-329 (1973).

[18] G. N. Plass, G. W. Kattawar, and F. E. Catchings, "Matrix operator theory of radiative transfer. 1: Scattering from maritime haze," Appl. Opt. **12,** 1071-1084 (1973).

[19] K. Stamnes, S.-C. Tsay, W. Wiscombe, and K. Jayaweera, "Numerically stable algorithm for discrete-ordinate-method radiative transfer in multiple scattering and emitting layered media," Appl. Opt. **27,** 2502-2509 (1988).

[20] K. Stamnes, S.-C. Tsay, W. Wiscombe, and I. Laszlo, "DISORT, a general-purpose Fortran program for discrete-ordinate-method radiative transfer in

scattering and emitting layered media: documentation of methodology," ftp://climate1.gsfc.nasa.gov/wiscombe/Multiple_Scatt/DISORTReport1.1.pdf (2000).

[21] B. T. Draine, "The discrete-dipole approximation and its application to interstellar graphite grains," Astrophys. J. **333,** 848-872 (1988).

[22] B. T. Draine and P. J. Flatau, "Discrete-dipole approximation for scattering calculations," J. Opt. Soc. Am. A **11,** 1491-1499 (1994).

[23] B. T. Draine and P. J. Flatau, "User guide for the discrete dipole approximation code DDSCAT 6.1," http://xxx.arxiv.org/abs/astro-ph/0409262 (2004).

[24] M. A. Yurkin, V. P. Maltsev, and A. G. Hoekstra, "The discrete dipole approximation for simulation of light scattering by particles much larger than the wavelength," J. Quant. Spectrosc. Radiat. Transfer **106,** 546-557 (2007).

[25] A. Penttilä, E. Zubko, K. Lumme, K. Muinonen, M. A. Yurkin, B. Draine, J. Rahola, A. G. Hoekstra, and Y. Shkuratov, "Comparison between discrete dipole implementations and exact techniques," J. Quant. Spectrosc. Radiat. Transfer **106,** 417-436 (2007).

[26] M. A. Yurkin and A. G. Hoekstra, "The discrete dipole approximation: An overview and recent developments," J. Quant. Spectrosc. Radiat. Transfer **106,** 558-589 (2007).

[27] B. T. Draine and J. Goodman, "Beyond Clausius-Mossotti: wave propagation on a polarizable point lattice and the discrete dipole approximation," Astrophys. J. **405,** 685-697 (1993).

[28] J. J. Goodman and B. T. Draine, "Application of fast-Fourier-transform techniques to the discrete-dipole approximation," Opt. Letters **16,** 1198-1200 (1991).

[29] W.-H. Yang, G. C. Schatz, and R. P. van Duyne, "Discrete dipole approximation for calculating extinction and Raman intensities for small particles with arbitrary shapes," J. Chem. Phys. **103,** 869-875 (1995).

[30] G. Liu, "Aapproximation of single scattering properties of ice and snow particles for high microwave frequencies," J. Atmos. Sci. **61,** 2441-2456 (2004).

[31] T. Wriedt, J. Hellmers, E. Eremina, and R. Schuh, "Light scattering by single erythrocyte: comparison of different methods," J. Quant. Spectrosc. Radiat. Transfer **100,** 444-456 (2006).

[32] C. V. Raman and K. S, Krishnan, "A new type of secondary radiation," Nature **121,** 501-502 (1928)

[33] H. Chew, P. J. McNulty, and M. Kerker, "Model for Raman and fluorescent scattering by molecules embedded in small particles," Phys. Rev. A **13,** 396-404 (1976).

[34] H. Chew, "Transition rates of atoms near spherical surfaces," J. Chem. Phys. **87,** 1355-1360 (1987).

[35] H. Chew, D. D. Cooke, and M. Kerker, "Raman and fluorescent scattering by molucules embedded in dielectric cylinders," Appl. Opt. **19,** 44-52 (1980).

[36] D. S. Wang, M. Kerker, and H. Chew, "Raman and fluorescent scattering by molecules embedded in dielectric spheroids," Appl. Opt. **19,** 2315-2328 (1980).

[37] H. Chew, M. Sculley, M. Kerker, P. J. McNulty, and D. D. Cooke, "Raman and fluorescent scattering by molecules embedded in small particles: numerical results for incoherent optical processes," J. Opt. Soc. Am. **68,** 1676-1686 (1978).

[38] H. Chew, M. Sculley, M. Kerker, P. J. McNulty, and D. D. Cooke, "Raman and fluorescent scattering by molecules embedded in small particles: results for coherent optical processes," J. Opt. Soc. Am. **68,** 1686-1689 (1978).

[39] M. Kerker and S. D. Druger, "Raman and fluorescent scattering by molecules embedded in spheres with radii up to several multiples of the wavelength," Appl. Opt. **18,** 1172-1179 (1979).

[40] V. Griaznov, I. Veselovskii, A. Kolgotin, and D. N. Whiteman, "Angle- and size-dependent characteristics of incoherent Raman and fluorescent scattering by microspheres. 1. General expressions," Appl. Opt. **41,** 5773-5782 (2002).

[41] I. Veselovskii, V. Griaznov, A. Kolgotin, and D. N. Whiteman, "Angle- and size-dependent characteristics of incoherent Raman and fluorescent scattering by microspheres. 2. Numerical simulation," Appl. Opt. **41,** 5783-5791 (2002).

[42] J. Zhang and D. Alexander, "Hybrid inelastic scattering models for particle thermometry: unpolarized emissions," Appl. Opt. **31,** 7132-7139 (1992).

[43] J. Zhang and D. Alexander, "Hybrid inelastic scattering models for particle thermometry: polarized emissions," Appl. Opt. **31,** 7140-7146 (1992).

[44] N. Velesco and G. Schweiger, "Geometrical optics calculation of inelastic scattering on large particles," Appl. Opt. **38,** 1046-1052 (1999).

[45] T. Weigel, J. Schulte, and G. Schweiger, "Inelastic scattering on particles with inclusions," J. Opt. Soc. Am. A **22,** 1048-1052 (2005).

[46] T. Weigel, J. Schulte, and G. Schweiger, "Inelastic scattering by particles of arbitrary shape," J. Opt. Soc. Am. A **23,** 2797-2802 (2006).

[47] P. J. Wyatt, "Differential light scattering: a physical method of identifying living bacterial cells," Appl. Opt. **7,** 1879-1896 (1968).

[48] C. J. F. Böttcher, *Theory of electric polarization*, Vol 1, (Elsevier, Amsterdam, 1973).

[49] J. Gersten and A. Nitzan, "Radiative properties of solvated molecules in dielectric clusters and small particles," J. Chem. Phys. **95,** 686-699 (1991).

[50] J. J. Maki, M. S. Malcuit, J. E. Sipe, and R. W. Boyd, "Linear and nonlinear optical measurement of the Lorentz local field," Phys. Rev. Lett. **67,** 972-975 (1991).

[51] H. A. Lorentz, *The theory of electrons* (Dover, New York, 1952).

[52] G. L. J. A. Rikken and Y. A. R. R. Kessener, "Local field effects and electric and magnetic dipole transitions in dielectrics," Phys. Rev. Lett. **74,** 880 (1995).

[53] F. J. P. Schuurmans, D. T. N. de Lang, G. H. Wegdam, R. Sprik, and A Lagendijk, "Local-field effects on spontaneous emission in a dense supercritical gas," Phys. Rev. Lett. **80,** 5077 (1998).

[54] A. J. Ward and J. B. Pendry, "Refraction and geometry in Maxwell's equations," J. Mod. Opt. **43,** 773-793 (1996).

[55] J. B. Pendry, D. Schurig, and D. R. Smith, "Controlling electromagnetic fields," Science **312,** 1780 (2006).

[56] U. Leonhardt and T. G. Philbin, "General relativity in electrical engineering," New J. Phys. **8,** 247 (2006).

[57] D. Schurig, J. B. Pendry, and D. R. Smith, "Calculation of material properties and ray tracing in transformation media," Opt. Express **14,** 9794-9804 (2006).

[58] U. Leonhardt, "Optical conformal mapping," Science **312,** 1777-1780 (2006).

[59] U. Leonhardt, "Notes on conformal invisibility devices," New J. Phys. **8,** 118 (2006).

[60] D. Schurig, J. B. Pendry, and D. R. Smith, "Transformation-designed optical elements," Opt. Express **15,** 14772-14782 (2007).

[61] E. J. Post, *Formal structure of electromagnetics* (Wiley, New York, 1962).

[62] S. A. Cummer, B.-I. Popa, D. Schurig, D. R. Smith, and J. B. Pendry, "Full-wave simulations of electromagnetic cloaking structures," Phys. Rev. E **74,** 036621 (2006).

[63] D. Schurig, J. J. Mock, B. J. Justice, S. A. Cummer, J. B. Pendry, A. F. Starr, and D. R. Smith, "Metamaterial electromagnetic cloak at microwave frequencies," Science **314,** 977 (2006).

[64] H. Chen, B.-I. Wu, B. Zhang, and J. A. Kong, "Electromagnetic wave interaction with a metamaterial cloak," Phys. Rev. Lett. **99,** 063903 (2007).

[65] B. Zhang, H. Chen, B.-I. Wu, Y. Luo, L. Ran, and J. A. Kong, "Response of a cylindrical invisibility cloak to electromagnetic waves," Phys. Rev. B **76,** 121101 (2007).

[66] M. Rahm, D. Schurig, D. A. Roberts, S. A. Cummer, D. R. Smith, and J. B. Pendry, "Design of electromagnetic cloaks and concentrators using form-invariant coordinate transformations of Maxwell's equations," Photon. Nanostruct.: Fundam. Applic. **6,** 87-95 (2008).

[67] H. Ma, S. Qu, Z. Xu, J. Zhang, B, Chen, and J. Wang, "Material parameter equation for elliptical cylindrical cloaks," Phys. Rev. A **77,** 013825 (2008).

[68] D.-H. Kwon and D. H. Werner, "Two-dimensional eccentric elliptic electromagnetic cloaks," Appl. Phys. Lett. **92,** 013505 (2008).

[69] R. M. Walser, "Metamaterials: an introduction," in *Introduction to complex mediums for electromagnetics and optics*, W.S. Weiglhofer and A. Lakhtakia eds. (SPIE Press, Bellingham, WA, USA, 2003), pp. 295-316.

[70] W. Cai, U. K. Chettiar, A. V. Kildishev and V. M. Shalaev, "Optical cloaking with metamaterials," Nature Photonics **1,** 224-227 (2007).

[71] A. Lakhtakia, "General theory of the Purcell-Pennypacker scattering approach and its extension to bianisotropic scatterers," Astrophys. J. **394,** 494-499 (1992).

[72] I. D. Faux and M. J. Pratt, *Computational geometry for design and manufacture* (Wiley, Chichester, 1979).

[73] T. Wriedt, "Using the T-Matrix method for light scattering computations by non-axisymmetric particles: superellipsoids and realistically shapes particles," Part. Part. Syst. Charact. **19,** 256-268 (2002).

[74] H. H. Poole, "The angular distribution of submarine daylight in deep water," Sci. Proc. R. Dublin Soc. **24,** 29-42 (1945).

[75] R. W. Preisendorfer, "Theoretical proof of the existence of characteristic diffuse light in natural waters," J. Marine Res. **18,** 1-9 (1959).

[76] G. W. Kattawar and G. N. Plass, "Asymptotic radiance and polarization in optically thick media: ocean and clouds," Appl. Opt. **15,** 3166 (1976).

[77] C. D. Mobley, *Light and water - radiative transfer in natural waters* (Academic Press, San Diego, 1994).

[78] H. C. van de Hulst, "Radiative transfer in thick atmospheres with an arbitrary scattering function," Bull. Astron. Inst. Neth. **20,** 77-86 (1968).

[79] E. Anderson, Z. Bai, C. Bischof, S. Blackford, J. Demmel, J. Dongarra, J. Du Croz, A. Greenbaum, S. Hammarling, A. McKenney, and D. Sorensen, *LAPACK users' guide* (Society for Industrial and Applied Mathematics, 1999).

[80] L. I. Chaikovskaya, I. L. Katsev, A. S. Prikhach, and E. P. Zege, "Fast code to compute polarized radiation transfer in the atmosphere-ocean and atmosphere-Earth systems," *Geoscience and remote sensing symposium proceedings, 1999. IGARSS '99. 1999 IEEE International* **2,** 1398, (1999).

[81] E. P. Zege, A. P. Ivanov, and I. L. Katsev, *Image transfer through a scattering medium* (Springer-Verlag, Heidelberg, 1991).

[82] H. H. Tynes, G. W. Kattawar, E. P. Zege, I. L. Katsev, A. S. Prikhach, and L. I. Chaikovskaya, "Monte Carlo and multicomponent approximation methods for vector radiative transfer by use of effective Mueller matrix calculations," Appl. Opt. **40**, 400-412 (2001).

[83] T. J. Petzold, "Volume scattering functions for selected ocean waters," SIO Ref., 72, Scripps Institution of Oceanography, La Jolla, Calif., (1972).

[84] J. T. Adams, E. Aas, N. K. Hojerslev, and B. Lundgren, "Comparison of radiance and polarization values observed in the Mediterranean Sea and simulated in a Monte Carlo model," Appl. Opt. **41,** 2724-2733 (2002).

[85] A. Morel, B. Gentili, H. Claustre, M. Babin, A. Bricaud, J. Ras, and F. Tièche, "Optical properties of the 'clearest' natural waters," Limnol. Oceanogr. **52,** 217-229 (2007).

[86] J. E. Tyler and R. C. Smith, *Measurements of spectral irradiance underwater* (Gordon & Breach, New York, 1970).

[87] N. G. Jerlov, *Optical Oceanography* (Elsevier, Amsterdam, 1968).

[88] V. I. Man'kovskii, "Specific features of the vertical distribution of the beam attenuation coefficient in the short- and long-wave spectral bands in deep-water layers of the hydrogen-sulfide zone and n the bottom layer of the Black Sea," Phys. Oceanogr. **13,** 183-187 (2003).

[89] A. Morel and L. Prieur, "Analysis of variations in ocean color," Limnol. Oceanogr. **22,** 709-722 (1977).

[90] G. R. Fournier, and J. L. Forand, "Analytic phase function for ocean water," in *Ocean Optics XII*, J. S. Jaffe, ed., Proc. SPIE **2258,** 194 (1994).

[91] V. I. Haltrin, "An analytic Fournier-Forand scattering phase function as an alternative to the Henyey-Greenstein phase function in hydrologic optics," *Geoscience and Remote Sensing Symposium Proceedings, 1998. IGARSS '98. 1998 IEEE International*, **2,** 910, (1998).

[92] C. D. Mobley, L. K. Sundman, and E.Boss, "Phase function effects on oceanic light fields," Appl. Opt. **41,** 1035-1050 (2002).

[93] T. Platt, and S. Sathyendranath, "Oceanic primary production: estimation by remote sensing at local and regimeal scales," Science **241,** 1613-1619 (1998).

[94] J. Berwald, D. Stramski, C. D. Mobley, and D. A. Kiefer, "Effect of Raman scattering on the average cosine and diffuse attenuation coefficient of irradiance in the ocean," Limnol. Oceanogr. **43,** 564-576 (1998).

[95] C. D. Mobley, and L. K. Sundman, *HydroLight 4.1 users' guide* (2000).

[96] C. Cox and W. Munk, "The measurement of the roughness of the sea surface from photographs of the sun's glitter," J. Opt. Soc. Am. **44,** 838-850 (1954).

VITA

Yu You, the son of Shigen You and Xulun Tan, was born in Xiangtan, Hunan, China. He graduated from the First Middle School of Xiangtan in 1998. He then attended the University of Science and Technology of China in Hefei, Anhui, China, for five years, and graduated with a Bachelor of Science in Physics in July, 2003. In the fall of 2003, he began his Ph.D. work in physics at Texas A&M University, and finished in August, 2008. He can be reached by e-mail at youyu123@hotmail.com, or by contacting Dr. George W. Kattawar at Texas A&M University.

The typist for this thesis was the author.